Improvement of ductility and crystallization properties of poly (lactic acid) (PLA)

Verbesserung der Duktilität und der Kristallisationseigenschaften von Polymilchsäure (PLA)

Vom Fachbereich Chemie
der Technischen Universität Darmstadt

zur Erlangung des Grades
Doctor rerum naturalium
(Dr.rer.nat.)

Dissertation
von
M. Sc. Maria Gokhale-Stec

Erstgutachter:	Prof. Dr. M. Rehahn
Zweitgutachter:	Prof. Dr. R. Pfaendner

Darmstadt 2021

Tag der Einreichung: 13. April 2021

Tag der mündlichen Prüfung: 31. Mai 2021

Gokhale-Stec, Maria: Improvement of ductility and crystallization properties of poly (lactic acid) (PLA)
Darmstadt, Technische Universität Darmstadt
Jahr der Veröffentlichung auf TUprints: 2021
URN: urn:nbn:de:tuda-tuprints-190921
Tag der mündlichen Prüfung: 31.05.2021

Acknowledgements

I express my deep gratitude to many people who are associated with this thesis and supported me over the last few years. First, I would like to sincerely thank Prof. Dr. Matthias Rehahn for providing me opportunity to pursue research at Technical University of Darmstadt and Fraunhofer LBF. I express my special acknowledgment to Prof. Dr. Rudolf Pfaendner for offering me a position in his research team and fabricating an international research program in collaboration with University of Queensland and Commonwealth Scientific and Industrial Research Organisation (CSIRO), Australia. I thank him for his guidance, motivation and giving a willing ear to discuss new ideas and challenges.

I am grateful to Dr. Ian Dagley from Cooperative Research Centre for Polymers (CRC-P) for inviting me to work in Australia and granting a solid financial aid to support my research. I am grateful to Prof. Peter Halley and Dr. Bronwyn Laycock from University of Queensland and Dr. Graeme Moad from CSIRO for giving me a very warm welcome to their research teams. I thank them for their guidance and providing me access to their lab facilities. I deeply appreciate friendly support from Dr. Michael Murphy and Dr. Emilie Gauthier for introducing me to the blown film extrusion equipment.

I would like to thank Dr. Frank Malz for his assistance in NMR measurements, and Helena Mertyn for GPC measurements. I thank Anina Leipold, Christoph Schultheis, Julien Fage, Dr. Bettina Weber and Dr. Christian Battenberg for their helpful discussions and suggestions. I truly thank all other colleagues at LBF for making my Ph.D. years so much enjoyable!

I owe special thanks to Ashwini Gokhale for reading manuscript of this thesis, discussing the corrections and making meaningful suggestions.

My parents and my brother have been instrumental in my life – I wouldn’t have made this far without their love and support. I would like to thank them with all heart!

Finally, my deepest gratitude goes to my beloved husband Dr. Rhishikesh Gokhale. His immense patience, encouragement and trust gives me strength to take on new challenges, and I couldn’t have accomplished this without him. I am truly blessed by being part of his life!

TABLE OF CONTENTS

List of abbreviations

Bis-MPA	2,2-bis-methylolpropionic acid
BTA	Butyl stannoic acid
°C	Degree Celsius
Ca	Capillary number
Ca_{cr}	Critical capillary number
$CDCl_3$	Deuterated chloroform
D	Droplet radius
DMSO-d_6	Deuterated dimethyl sulfoxide
DSC	Differential scanning calorimetry
E-BA-GMA	Ethylene-Butyl Acrylate-Glycidyl Methacrylate
EBS	Ethylene bis-stearamide
E-GMA	Ethylene-Glycidyl Methacrylate
FDA	Food and drug aministration
G	Gramm
$\dot{\gamma}$	Shear rate
ΔG_{cryst}	Heat of crystallization
ΔG_m	Gibbs free energy of mixing
GPC	Gel permeation chromatography
GRAS	Generally recognized as safe
ΔG_{surf}	Surface energy
H	Hour
HBP	Hyperbranched Polymer
ΔH_{cm}	Crystallization enthalpy
HDPE	High-density polyethylene
ΔH_m	Enthalpy of Mixing
IR	Infrared spectroscopy
J	Joule
Kg	Kilogram
LA	Lactic Acid
LDPE	Low-density polyethylene
LLDPE	Linear low-density polyethylene
MAH	Maleic anhydride
Min	Minute
M_n	Number average molecular weight
MPa	Megapascal
mPE	Metallocene polyethylene
M_w	Weight average molecular weight
NA	Nucleating agent
NMR	Nuclear magnetic resonance
OA	Orotic acid
P	Viscosity ratio
PA 6	Polyamide 6
PA 6.6	Polyamide 6.6

PC	Polycarbonate
PDI	Polydispersity index
PE	Polyethylene
PEG	Poly(ethylene glycol)
PE-g-MA	Polyethylene-graft-maleic anhydride
PET	Polyethylene terephthalate
Phr	Parts per hundred
PI	Phthalimide
PLA	Polylactic Acid
PP	Polypropylene
PP50	Ethoxylated pentaerythritol
PS	Polystyrene
PVC	Polyvinyl chloride
r_{crit}	Critical embryo size
ROP	Ring opening polymerization
Rpm	Rotation per minute
S	Second
SA	Stearic acid
SEM	Scanning electron microscopy
ΔSm	Entropy of mixing
T	Temperature
$t_{1/2}$	Crystallization half-time
TAI	Trichloracetylisocyanate
T_{cc}	Cold crystallization temperature
T_{cm}	Crystallization temperature
T_g	Glass transition temperature
TGA	Thermogravimetric analysis
T_m	Melting Temperature
TMC	Tetramethylenedicarboxylic dibenzoylhydrazide
TN	Terephthaloyl-bis-N, N’-naphthalimidester
Wt	Weight
X_c	Percentage crystallinity
X_t	Relative crystallinity
Δ	Interfacial tension
η_m	Matrix viscosity
η_d	Dispersed Phase Viscosity

1. Introduction

1.1. Global Plastic Production

Gradual replacement of most traditional materials like glass, wood, ceramics, metal, leather and paper with synthetic polymers is a way to overcome challenges connected with climate change, energy demand, urbanization, fast-growing population and food security. Owning to their versatility, easy processing and fascinating properties, polymers are the material of choice in applications such as packaging (~40 % of plastic production), the building and construction sector (~20 % of plastic production), automotive industries (~10 % of plastic production), and agriculture [1]. The increase in the global demand for plastic is driven by the need to develop efficient and innovative solutions for existing problems that are a result of our modern lifestyle. According to the report *Plastics Product Manufacturing Global Market 2017* published by The Business Research Company, the total global production of plastic increased from 1.7 million tons in 1950 to 335 million tons in 2016, and it was worth 1.06 trillion US Dollars in 2016 [2]. As stated in the same report, the global market for plastic products will be worth 1.175 trillion US Dollars by 2020 [2]. However, the strong growing global demand for plastic materials, and the current levels of their usage and disposal entails consequences that must be addressed.

Fossil feedstocks, being a constantly diminishing energy resource, is the main raw material source to produce plastic. Over 99 % of plastics are produced from non-renewable resources such as natural gas, oil or coal [3,4]. About 6 % of global oil supply is used to produce plastic, which is equivalent to the oil consumption of the global aviation sector [5]. If the global plastic demand continues as expected, the production of new plastics will reach 20 % of total oil consumption by 2050 [5]. As the global trend goes towards a future free of fossil fuel, the dependence on fossil fuel as the only raw material source for plastic production, is not enough. Therefore, there is a need to find alternatives through exploring the role of renewable resources in plastic production.

It is estimated that 8300 million metric tons of plastics have been produced to date, out of which 60 % (4900 million metric tons) were discarded and are accumulating in landfills or in the natural environment [6]. This amount of plastic is a great concern to the environment because most varieties of plastic are inherently bio-resistant. Standard plastics like polyolefins, PVC, PET and PS represent approximately 75 % of the global plastics production, whereas polyethylene and polypropylene, with their major application as single-use packaging, constitute over 50 % by weight of all plastic produced in 2016 [4]. Out of all plastics used in the packaging sector, 40 % is landfilled and 32 % is either dumped illegally or not collected [5].

Every year, between 4.8 and 12.7 million tons of plastic is dumped into our oceans [7]. This amount of waste has a hazardous impact on marine environment and if no action is taken, there might be more plastic than fish, by weight, by 2050 [5]. Plastic particles eaten by fish, turtles and birds are causing their premature death. In addition, micro plastic is transferred up the food chain and gets accumulated inside the human body upon consumption and can leach toxins. Based on studies using laboratory animals as model organisms, cardiovascular diseases, type 2 diabetes, reproductive abnormalities, obesity and cancer can be directly linked with accumulation of plastics and chemicals used in the manufacture of plastics [8].

Due to the constantly growing plastic demand and the associated concern of raw material source for plastic production and disposal, the options of detaching plastic from fossil feedstock and producing plastics with a different end-of-life option are becoming increasingly desirable. The concerns associated with conventional plastic materials have driven the increase in focus towards developing sustainable polymers - where fossil raw materials are replaced with renewable feedstock and the disposal can be of biodegradable or compostable nature [9].

1.2. Polylactic Acid (PLA)

1.2.1. Feedstock and manufacturing of PLA

Polylactic acid is a compostable aliphatic polyester, produced from renewable material sources. The commercial production of lactic acid (LA), a basic building unit for PLA, involves microbial fermentation of sugar from renewable resources like potato, tapioca, wheat, barley, corn, sugar cane, etc. [10]. Feedstock for lactic acid production is versatile, since any carbohydrate source containing pentoses or hexoses can be used as a substrate [11]. The monomer for PLA production exists in two enantiomeric forms and depending on microorganisms used in the fermentation process, either optically pure lactic acid (L-isomer or D-isomer) or racemic mixture of both can be produced [10]. PLA is generally recognized as safe (GRAS) by the United State Food and Drug Administration (FDA) and is safe for food packaging application [12,13].

The most common synthetic route to produce high molecular weight PLA involves ring-opening polymerization (ROP) through lactide intermediate. The synthetic route involves three main steps, as presented schematically in Figure 1.

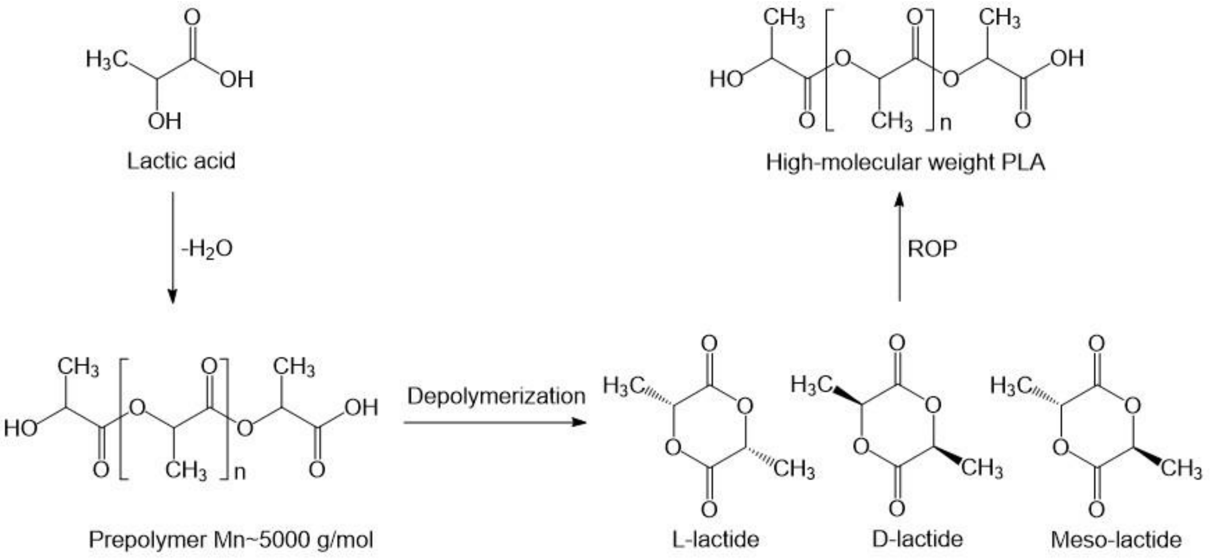

Figure 1: Schematic representation of PLA synthesis.

The controlled depolymerization step can yield three stereoforms of lactide: L-lactide, D-lactide, and meso lactide. Therefore, PLA produced from this process can be derived from different amounts of L and D-lactide[10,14]. A broad number of catalyst systems have been developed to provide stereo-controlled ROP of lactide, including metal-based, organic, enzymatic or anionic [15]. The most preferred and studied are tin compounds, especially tin octoate, due to their solubility in molten lactide, high catalytic activity and low rate of racemization of the polymer [16]. Currently NatureWorks, one of the biggest PLA producers, manufactures 150 thousand tons PLA per year using corn feedstock [17]. The land used to produce 150 thousand tons Ingeo™ PLA makes only 0.00046 % of available agricultural area, meaning that the impact on land use is very small [17]. Contrary to petroleum-based products, the price of PLA-based products depends on the cost of sugar, and is therefore unlikely to face fluctuations[18]. When compared with standard hydrocarbon-based polymers (e.g. PA 6.6, PA 6, PC, PS, PET, PE, PP, PVC), the PLA manufacturing process (from the cradle to the polymer factory exit gate) contributes strongly to its sustainable character because it is characterized by very low emission of carbon dioxide and distinctly lower water use [17]. In addition, PLA offers several end-of-life options, because it is recyclable or biodegradable under industrial composting [14]. PLA recycling includes chemical and mechanical recycling. Mechanical recycling involves reprocessing of PLA waste, whereas chemical recycling involves hydrolyzing PLA to LA at an elevated temperature. Recycling could be an optimum disposal route for uncontaminated packaging (e.g. water bottles), while compositing is preferable for food-contaminated plastics. During industrial composting, PLA is hydrolyzed at about 60°C to reduce molecular weight and degradation occurs by the action of microorganisms present in the soil, resulting in carbon dioxide and water. The compost medium has high moisture content, high temperature, and diverse microbial population, and therefore, compost degradation of PLA is faster than PLA biodegradation in the soil [19]. Nevertheless, in several studies, changes in PLA performance were observed after the soil burial test [19]. Calmon et al. buried PLA samples in four different areas of France for two years. After this period of time PLA was still present [20]. However, signs of physical degradation were seen after measuring the weight loss. Weng et al. studied degradation of PLA film under real soil conditions, buried in the west of Beijing, China [21]. Significant degradation of PLA was observed after four months of open soil burial trial leaving behind a small amount of residue [21]. Thus, temperature and geographical location might have a substantial impact on PLA degradation and further research is required to gain deeper insights into PLA degradation as a function of these variables.

1.2.2. PLA Properties

The control over L- to D-isomer ratio in the final polymer as well as molecular weight has a major influence on PLA properties [11,22]. The isomer content correlates directly with PLA crystallinity. The optical pure material produced from either L-lactide or D-lactide has an ordered structure, and therefore, a high crystallinity level (~ 45 %, when full annealed) and melting temperature (~ 190 °C) [23]. As the optical purity decreases, due to the L- and D-unit distribution, the PLA becomes stereo-irregular, and consequently, its crystallization ability decreases [23,24]. For the production of commercial PLA resin, mainly L-isomer with a small amount of D-isomer is used [25]. As the minor co-monomer amount exceeds 10 %, the final polymer is amorphous [26]. PLA crystallinity and crystallization rate are both important factors affecting its general properties, and therefore, in defining the PLA application. The crystalline fraction is more rigid than the amorphous, and therefore, an increase in PLA crystallinity is responsible for its high tensile strength and modulus [22,27,28]. Amorphous PLA has a lower glass transition temperature (T_g) than a crystalline sample. At a temperature above T_g, the chain mobility of the amorphous fraction increases, and therefore, heat deflection temperature and Vicat Penetration are influenced by the degree of crystallinity in PLA [22]. Moreover, crystallinity degree is an important factor, which determines PLA barrier properties to a great extent, and is especially crucial for packaging applications. Good permeability performance against transfer of gases and water vapor is required in the food packaging sector. The rate of water vapor transfer and oxygen and methane permeability can be reduced by increasing film crystallinity [29–31]. However, PLA crystallization is a very slow process. PLA remains amorphous under high supercooling conditions such as injection molding, [32]. Further, sample annealing at an elevated temperature might be associated with material degradation due to prolonged thermal treatment [33]. Due to low heat deflection temperature (~60 °C) PLA cannot be used for microwaveable containers, single-use cups for hot drinks, or electrical and automotive parts where resistance to heat is required [34–36]. Therefore, many commercial applications of PLA are limited to non-heat applications [14]. In addition, a slow crystallization rate results in longer molding cycles due to difficulties in ejecting the part. Moreover, low barrier properties limit the usage of PLA bottles to non-carbonated beverages. Incorporation of a nucleating agent is a good strategy to increase crystallinity and improve crystallization rate. Consequently, the issue of pure thermal stability and barrier properties can be overcome and the cycle time during injection molding of PLA goods can be reduced. Another main shortcoming of PLA is brittleness. PLA fails by crazing with the elongation at break less than 10 % [37]. Its poor ability to absorb impact energy without breaking or to absorb energy while stretching restrict PLA usage in the packaging, films or textile fiber areas [38,39]. Thus, polymer needs to be modified in order to be used in applications that need plastic deformation at higher stress level [37]. Compared to the conventional polyolefins PE and PP that are typically used in packaging applications, the higher price of PLA further limits its widespread application [18,40]. The high cost is not due to the polymerization process itself, but is due to the process of obtaining the monomer (lactic acid and lactide) for the polymerization process [41]. Moreover, the supply chain is also a concern, because NatureWorks has been the main industrial-scale producer of PLA [42,43]. Therefore, in order for PLA based materials to be a good alternative to conventional plastics, effort must be made to improve the mechanical and thermal properties as well as to decrease the final product price.

1.3. Tailoring the mechanical properties of PLA

1.3.1. Polymer blends theory

The blending of two or more polymers is the most effective and inexpensive way to overcome shortcomings of single polymers. This is achieved by tailoring their combinations to produce new materials with better overall properties [44]. Whereas the development and commercialization of new polymers is costly and time consuming, the blending process is cheaper and more efficient in order to develop a new material with desired properties [45]. Based on the miscibility of components, there are three categories of polymer blends: miscible, partially miscible, and immiscible [46]. Blend miscibility depends on the value of *Gibbs energy of mixing* (ΔG_m), which is given by:

$$\Delta G_m = \Delta H_m - T\Delta S_m \qquad (1)$$

The enthalpy of mixing ΔH_m expresses heat that is either consumed ($\Delta H_m > 0$, endothermic process) or generated ($\Delta H_m < 0$) exothermic process) during mixing [47]. Entropy of mixing ΔS_m determines the number of possible mixed configurations [48]. For long-chain macromolecules, ΔS_m is very low and can be negligible. Therefore, ΔG_m is determined by ΔH_m [48]. Two polymers are miscible if the value of energy of mixing is negative, and this condition requires exothermic heat of mixing [49,50]. To promote exothermic mixing condition and thus blend miscibility, strong specific interactions, such as strong covalent and ionic bonding or weaker hydrogen bonding or dipole-dipole, ion-dipole, donor-acceptor interactions need to occur between the blend components [49]. Miscible blends form a single phase, which is homogeneous down to the molecular level and is characterized by a single glass transition temperature. The overall blend performance can be predicted based on the composition-weighted average of the properties of the individual blend components [50]. However, very few polymer pairs fulfil the miscibility criteria. In case of most of the polymer pairs, only very weak van der Waals interactions appear, and thus their blends are immiscible [47]. A heterogeneous, immiscible polymer blend exhibits phase separation on a macroscopic scale. Due to this, the physical properties are poor in comparison with individual blend components and depend greatly on the blend morphology. Large interfacial tension between the polymer phases is caused by the lack of favorable interaction and results into phase separation. Therefore, control over morphology in multiphase polymer blends, developed during the melt mixing process, enables tailoring of the final material properties. Morphology itself is defined by the shape, size, and spatial distribution of blend phases [51]. Based on the composition, concentration of ingredients, material parameters and processing conditions, there can be two categories of morphology for heterogeneous systems: dispersed or co-continuous.

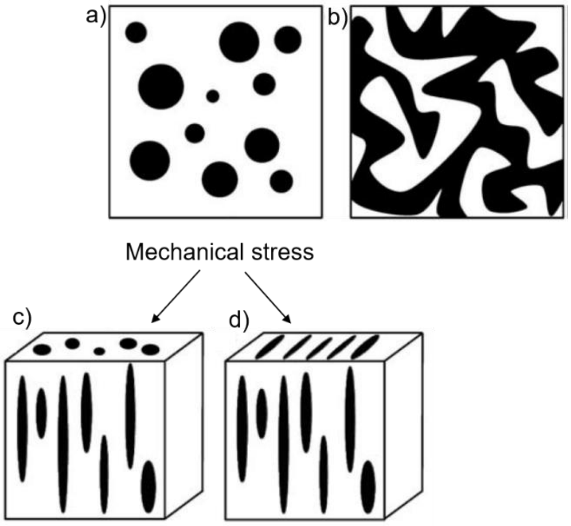

Figure 2: Schematic representation of a) dispersed blend morphology, b) co-continuous blend morphology, c) and d) deformed particles of dispersed phase. Scheme adopted from reference [47].

Dispersed morphology is characterized with particles surrounded by a matrix, whereas in case of co-continuous morphology both phases are fully continuous. The dispersed particles often take an energetically-favorable spherical shape. However, as a consequence of shear stress and/or elongation flow field, anisotropic deformed particles such as ellipsoids, fibrils, or platelets can also be observed in polymer blends [47].

Several steps are involved in morphology development during melt mixing of immiscible polymer blends as a matter of action of heat and shear forces inside an extruder barrel. The initial step involves softening and melting of blend components in the form of pellets, flakes, or powder. If the minor component softens first, then it develops the matrix phase, which is rearranged into dispersed phase after the major component melts. This process is called phase inversion and its progress is influenced by the viscosity ratio of components. The latter, consequently affects the blend morphology. Phase inversion does not occur if the major component softens before the minor component. During melt-mixing, the final shape and size of the phase domains depends upon the deformation process, such as droplet stretching into threads or sheets, followed by breakup into smaller droplets, and competitive process of droplet coalescence into larger ones [47,51].

The deformation of dispersed liquid droplets in a liquid matrix under a flow is governed by two dimensionless parameters, the capillary number Ca, and the viscosity ratio p of the components. Ca is defined as the ratio of the deforming hydrodynamic stress to the restoring interfacial stress.

$$Ca = \frac{\eta_m \dot{\gamma} d}{\sigma} \tag{2}$$

$$p = \frac{\eta_d}{\eta_m} \tag{3}$$

where η_m and η_d stand for viscosity of the matrix and dispersed phase, respectively, $\dot{\gamma}$ is the shear rate, d is droplet radius of the dispersed phase, and σ is the interfacial tension between the phases. Droplet breakup occurs if a certain value of Ca, defined as critical capillary number Ca_{CR} exceeds for a given viscosity ratio. This means, the hydrodynamic stress that tends to deform the droplet is sufficiently high. First, the drop becomes unstable and eventually breaks into smaller drops. This results in a fine distribution of the droplets in the matrix. At the value of Ca below Ca_{CR}, drops are deformed in the flow in a steady shape and droplet break-up does not occur. Figure 3 schematically shows the conditions for various stages of droplet deformation and breakup as a function of p.

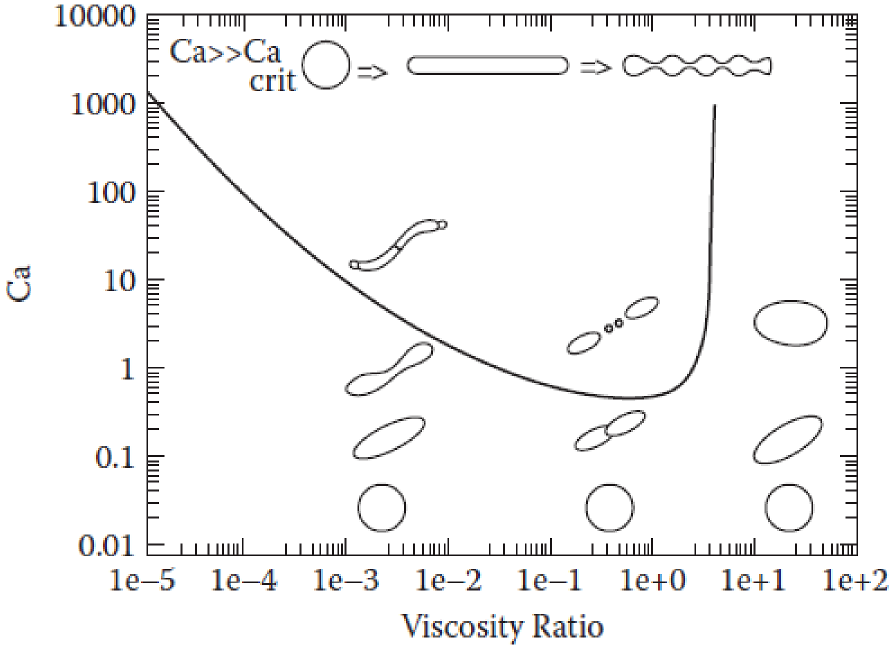

Figure 3: Schematic representation of the capillary number *Ca* vs. viscosity ratio in shear flow. Above the critical capillary number Ca_{CR} (represented as a solid line) droplet breaking by fracture occurs. Scheme adopted from reference [52].

On the one hand, the development of the dispersed phase can be altered while blend processing, by changing the temperature, the rotational speed of extruder screws, or the mixing time. The processing parameters control the viscosity ratio of the blend components to a great extent. Nevertheless, the thermal stability of the processed polymer needs to be considered, because polymers decompose above a certain temperature and very high shear forces contribute to chain scission. On the other hand, interfacial tension is a parameter that cannot be adjusted while blend processing. Large interfacial tension causes phase separation, which results in large particle size and prevents the deformation of the dispersed phase during mixing [49]. Adding compatibilizers lowers the interfacial tension, thereby making the deformation and break-up of droplets easier. Therefore, as an effect of compatibilizer addition, *Ca* increases without the need for drastic changes in the processing parameters.

During polymer mixing in the flow field, the process of droplet coalescence competes with the process of droplet deformation and breakup. Coalescence is as a natural tendency of multiphase polymer systems to minimize the interfacial area and thereby minimizing the free enthalpy [53].

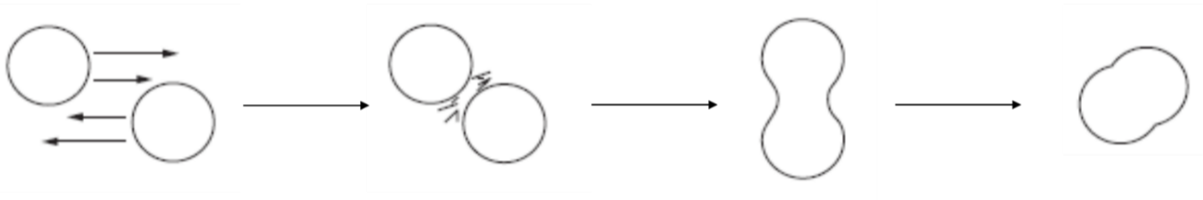

Figure 4: Schematic representation of coalescence in polymer blends. Scheme adopted from reference [54].

An increase in the concentration of the dispersed phase increases the probability of droplet collision. As two drops approach each other by a shear field, the matrix film filling the gap between them thins and is squeezed out. The coalescing droplets merge as soon as a critical distance between them is exceeded and as a result a bigger drop is formed. Therefore, coalescence counteracts the development of fine dispersed blend morphology. A compatibilizer added to the system of a binary polymer blend and located at the interface between two phases prevents the drops from reaching the critical distance, and thus inhibits coalescence.

1.3.2. Compatibilization

Interfacial modification of immiscible blends contributes to fine dispersion of the minor phase by stabilizing phase morphology against coalescence and reduction of interfacial tension between two phases [55,56]. Compatibilizers improve the interfacial adhesion between the two phases, which leads to better stress transfer from one phase to another, and thereby preventing interfacial failure [57]. By using compatibilizers, the mechanical properties sensitive to stress transfer - in particular the impact strength, maximum strain at break, and the yield strength - are enhanced [55]. Compatibilization can be performed either in a non-reactive or reactive process.

Non-reactive, additive compatibilizers are premade block (linear or star-shaped, di-block or multi-block) or graft copolymers and are constituted of at least two different segments (Figure 5). Each of the segments is miscible with particular blend components, although do not need to be identical with the corresponding blend component. Compatibilization efficiency depends on the number and the length of blocks, the ratio of blend components, and the processing conditions [47]. The drawback of non-reactive compatibilizers relates to the tendency of micelles formation [58]. A short blending time and a high viscosity in polymer melt systems restrict the diffusion of the compatibilizer to the interface [56,58,59].

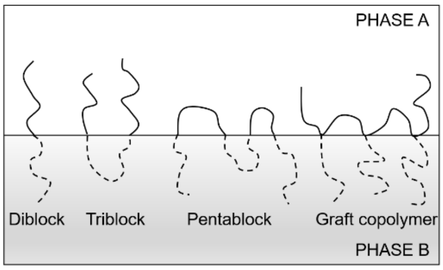

Figure 5: Schematic representation of an ideal localization of block (di-block and multi-blocks) copolymers and graft copolymers at the interface between two immiscible polymers. Scheme adopted from reference [60].

Reactive compatibilization, unlike a non-reactive one, is based on the formation of the block or graft copolymer compatibilizers directly at the phase interface, through covalent or ionic bonds, in situ during the blending process. Depending on the type of immiscible polymer pairs selected for the melt mixing, there are three scenarios of how the compatibilization process occurs [59].

- Reactive polymer pair - both polymers contain functional groups that are mutually reactive. The reaction between the two blend components results into the formation of a copolymer compatibilizer.
- One blend component is a reactive polymer with functional groups, whereas the second one is chemically inert with respect to the first. Two compatibilization strategies can be applied for this system. One method is based on modifying a non-reactive polymer with functional groups being able to react with the reactive polymer. The other method is the introduction of a reactive compatibilizer precursor. The latter, can be a functionalized polymer, possessing a backbone miscible with one of the blend components and reactive groups suitable to form covalent or ionic bonds with functional groups of the other blend component.
- Non-reactive polymer pair - where both polymers are chemically inert. Reactive compatibilization can also be achieved through functionalization of both polymers with groups, which are mutually reactive or through incorporation of two additional reactive polymers. Each of the reactive polymers has a backbone miscible with one of the nonreactive blend components, and upon their reaction effective compatibilization can be accomplished.

Based on structural considerations, PLA is an aliphatic polyester. Therefore, compatibilization of PLA- based blends can be achieved upon utilization of PLA terminal carboxyl and hydroxyl groups. The common compatibilizer precursors used to react in situ during melt mixing in the blend system with the polyester host (where one of the components is polyester) are those with functional groups such as glycidyl methacrylate (GMA), maleic anhydride (MAH), oxazoline, isocyanate, hydroxyl or carboxyl [61–65]. Reactions between PLA terminal groups and functional groups of reactive precursor are summarized in Figure 6.

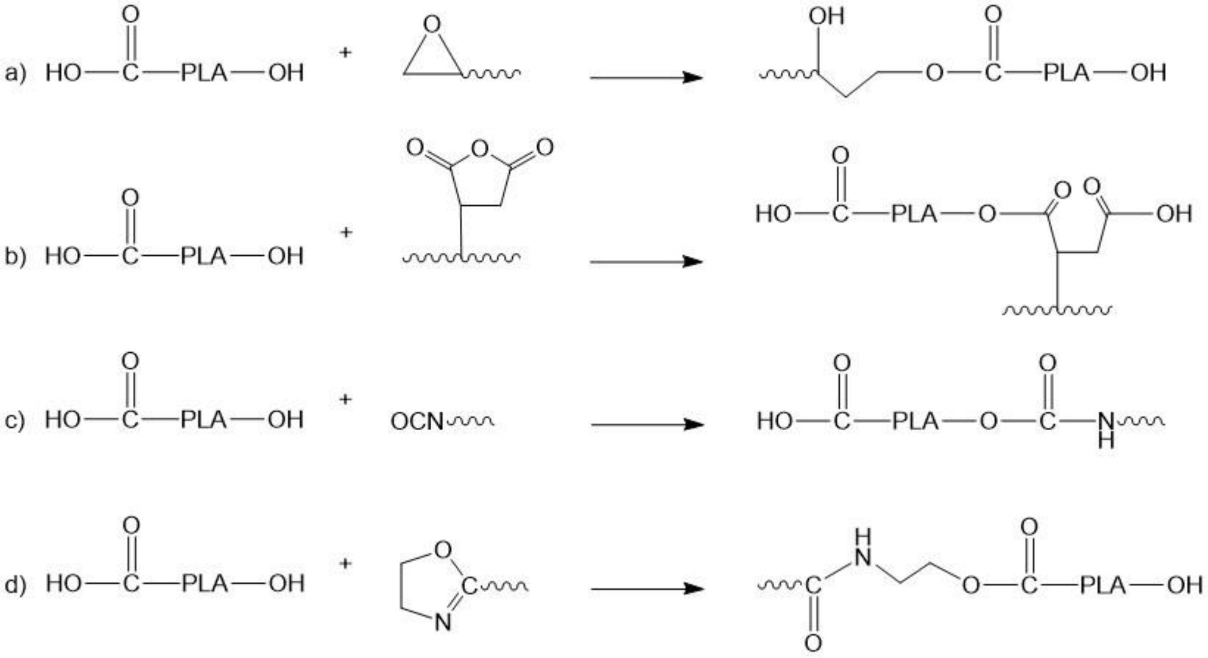

Figure 6: Schematic representation of reactions between PLA terminal groups and a) glycidyl methacrylate, b) maleic anhydride, c) isocyanate, d) oxazoline functional groups. Scheme adopted from reference [60].

Among the above mentioned precursors, the one with GMA group (that contains epoxy moiety) is an attractive choice for reactive extrusion with polyester, due to its reactivity with both polyester carboxyl and hydroxyl end groups [61,63]. In addition, the coupling between carboxyl and epoxy terminal chains is faster than corresponding reactions with oxazoline terminal chains [66]. Moreover, the reaction of the MAH unit with polyester hydroxyl end group is reversible at high mixing temperature and is unfavorable for efficient compatibilization [63,67,68]. The possibility of forming compatibilizers directly during melt blending makes reactive extrusion an efficient and cost-effective way over non-reactive compatibilization [59]. In addition, the viscosity of the reactive precursor is lower in comparison with that of the non-reactive compatibilizers. Thus, the transport to the interface, where the actual compatibilizer is formed and located, is faster [47]. Reactive compatibilization is an efficient process, provided that the compatibilizer precursor is capable of reacting and forming compatibilizers within a relatively short processing time during melt blending, which is in the range of a few minutes. Therefore, the performance of reactive extrusion depends strongly on the concentration and the accessibility of functional groups. A sufficient amount of reactive functional groups enhances the chance of copolymer formation during melt blending. In addition, fast diffusion of the precursor to the phase interface is advantageous in terms of successful compatibilization [50]. Most of the reactive compatibilization strategies are based on linear precursors with terminal or pendent functional groups. An alternative to this is using a polymer with hyperbranched architecture. As a result of the three-dimensional, packed structure and lack of entanglements, the viscosity of hyperbranched polymers in solution and molten state is much lower than that of linear polymers of the same molar mass [69–72]. Moreover, large numbers of functional groups positioned at the structure peripheries are easy to access increasing reactivity and, therefore, grafting efficiency at the interface. Faster diffusivity to the interface, ascribed to low viscosity, together with higher reactivity of multifunctional hyperbranched polymer contribute to stronger compatibilization efficiency in comparison with a functional linear polymer [73–75]. High regular dendritic polymers with monodispersed structures are prepared step by step via convergent and divergent approaches. Unlike the regular dendritic polymers, hyperbranched polymers are polydisperse products, formed in one-step or a pseudo-one step procedure, and this makes the synthesis attractive from an industrial point of view [76,77].

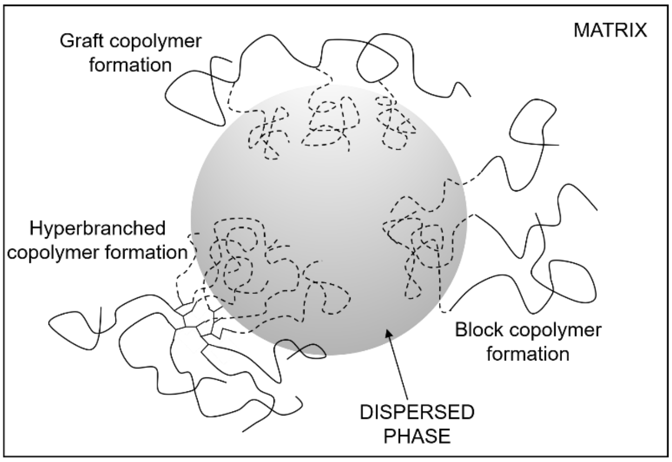

Figure 7: Schematic illustration of grafted, hyperbranched and block copolymers formed at the interface between matrix and dispersed phase.

1.3.3. Polyethylene (PE) as a blend component for PLA

PLA /Polyethylene (PE) mix is a classic example of polymer blends, where the unique properties of both PLA and PE phases add value to the final product and also compensate each other for their individual shortcomings. The origin of PLA from natural resources and its biodegradable nature are the key advantage of PLA, and hence makes it the preferred choice in the development of environmentally-friendly goods. However, PLA has low impact resistance and high brittleness, and therefore has some deficits in commercial applications [11]. PE, by contrast, is one of the most well-known commodity polymers and is utilized heavily in packaging and greenhouse coverings due to its excellent mechanical properties and low cost [78]. One of the main shortcomings of PE is that it degrades very slowly under environmental conditions, even after being exposed to oxygen and ultra violet light [79–84]. Blending of PLA with PE can improve the toughness of PLA and lowers the cost of the final product. In addition, the manufacturing of goods containing biodegradable and non-biodegradable polymers reduces the total amount of polymer waste, which cannot degrade in nature.

Considering the differences in solubility parameters between PLA and PE, they are expected to be immiscible (21.3 $(J/cm^{-3})^{1/2}$ for PLA and 17.1 $(J/cm^{-3})^{1/2}$ for PE) [85–87]. This was confirmed by Hamad et al., who showed in his study that non-Newtonian index of PLA and low density polyethylene (LDPE) blends are less than those of homopolymers [88,89]. Nevertheless, rheological results of his study reveal that high viscosity of PLA/LDPE at a low shear rate can provide integrity to the extrudate during extrusion, whereas low viscosity of the blend at a high shear rate can lead to high injection speed and less time of the injection cycle, which make these blends interesting materials from the processing point of view. Further, Djellali et al. demonstrated immiscibility between PLA and LDPE on the basis of rheological properties, viscoelastic behavior and thermal analysis [90]. In this study it was shown that rheological properties of PLA/LDPE blends differ from the properties predicted by the additivity law. This might be considered as an indication of immiscible blend components in the melt. Moreover, based on thermal analysis of PLA/LDPE blends, no significant shift of glass temperature was observed, which additionally indicates that this blend system is immiscible.

Although it is established that PLA and PE are immiscible in the melt, there is evidence in the literature that physical melt blending of these two materials results in a blend with potentially attractive properties. The change in properties of PLA/PE blends after physical melt blending of PE in PLA was studied by Balakrishnan et al. who investigated the effect of loading linear low density polyethylene (LLDPE) in a PLA matrix on the morphology, mechanical and thermal properties of the resulting PLA/LLDPE blends[91]. The main outcome of this study was that the melt blending of LLDPE in PLA improved the impact strength of PLA with an associated sacrifice of stiffness and strength [91]. In another approach, Jiang attempted to optimize the morphology of PLA/LLDPE blends by controlling the melt processing (mixing type) through a combination of different screw elements in a single screw extruder. He showed that a co-continuous morphology appears in PLA/LLDPE blends when produced using high shear/chaotic mixing, which is characterized by stretching and folding the materials during flow [92].

Besides adjusting a processing method, properties of PLA/PE blends can be improved by adding a suitable compatibilizer. Several attempts have been made to increase the compatibility of PLA/PE blends to enhance the interfacial adhesion and reduce interfacial tension between the PLA and PE phases. Anderson and coworkers reported that when amorphous PLA was melt mixed with LLDPE (weight ratio 80/20) the addition of PLA-PE block copolymer, consisting of semi crystalline PLA, was required in order to improve the impact resistance of this formulation (34 J/m for the binary blend versus 460 J/m for the compatibilized blend) [87]. However, when semi crystalline PLA was used as a matrix, the toughening effect was observed even in the absence of compatibilizer (350 J/m for PLA/LLDPE blend versus 20 J/m for PLA) [87]. In another study, Anderson and co-workers reported the properties of PLA/PE blends where three different polyethylene types were used. It was observed that the impact properties of the final blend depended strongly on the properties of the dispersed phase, (the PE phase). Moreover, the influence of different PLA-PE block copolymers with varying crystallizing ability at the PLA/PE interfacial adhesion was reported [93]. For PE with the lowest stiffness (LLDPE containing 13.2 mol % octene), the greatest improvement in the impact properties was achieved by using a block copolymer with the strongest interfacial adhesion. Whereas, for PE with intermediate stiffness (LLDPE containing 4.8 mol % octene), the greatest improvement in toughening properties was achieved when a block copolymer with an intermediate degree of adhesion was used. When PE with the highest modulus (HDPE) was used as the dispersed phase, the addition of block copolymer that gave the weakest interfacial adhesion led to the largest improvement in the impact properties.

Some authors studied the addition of compatibilizers with reactive groups to improve blend compatibility and properties of the resulting PLA/PE blends. A copolymer of ethylene and glycidyl methacrylate (E-GMA) and terpolymers of ethylene-methyl acrylate-glycidyl methacrylate (E-MA-GMA), ethylene-butyl acrylate-glycidyl methacrylate (E-BA-GMA) and ethylene–glycidyl methacrylate–vinyl acetate (E-GMA–VA) have been reported by researchers to improve the compatibility between PLA and PE [94–99]. Kim et al. found that the addition of the E-GMA copolymer to the PLA/LDPE blend resulted in improved strain at break from 6.6 % for the binary blend to 77.9 % for the ternary blend. Moreover, it was shown that increasing the weight percentage of GMA units in the copolymer from 8 wt % to 25 wt % enhanced the compatibility of E-GMA towards PLA but decreased the compatibility of E-GMA towards LDPE [100]. Other reactive blends based on PLA, PE, and PE grafted with maleic anhydride (PE-g-MA) have also been reported in the literature. Abdolrasouli et al. studied the effect of maleic anhydride grafted PE (PE-g-MA) on the phase morphology and melt viscoelastic properties of PLA/PE/organoclay blend nanocomposites. It was reported that organoclay hinders the coalescence of PE droplets. By contrast, the introduction of the compatibilizer into the blend results in intercalated structures and a finer morphology in the blend nanocomposite [101]. In the examples presented above, compatibilization of immiscible PLA/PE blends using a suitable compatibilizer was used as a technique to form fine phase morphology and improve interfacial interaction between PLA and PE. An incompatible PLA/PE blend with poor properties could be transformed into compatible PLA/PE blend with good properties due to a reduction in the size of the dispersed phase.

1.4. Tailoring thermal properties of PLA

1.4.1. Polymer Crystallization Theory

The tendency of polymer molecules to crystallize depends on the chemical composition and on the extent of the secondary bond forces among the polymer chains [102]. Crystallinity in macromolecules is impaired by factors affecting structural regularity - such as the presence of branches, and large side groups or copolymers. Crystallization might be enhanced when polar groups (for example, amide, carboxyl, hydroxyl, nitrile) are present along the polymer chain [102]. Crystallization requires stable nuclei and can be initiated upon cooling from the melt, annealing, or mechanical stretching. The crystallization process of polymeric materials consists of nucleation and subsequent growth of polymer crystals [103]. There are two types of nucleation processes - homogeneous and heterogeneous.

In homogeneous nucleation, the formation of nuclei in the melt is due to thermal fluctuations at the local order level [104]. In the primary nucleation step, thermally activated random motion triggers spontaneous aggregation of aligned polymer segments to form unstable crystalline embryos [105]. The formation of the interface between crystal and melt requires energy in the form of surface energy (ΔG_{surf}) [105]. At the same time, the energy in form of heat of crystallization is released (ΔG_{cryst}) since the ordered state has a lower energy than the disordered state [106]. The result of the competing effect between ΔG_{surf} and ΔG_{cryst} for the nucleation process is illustrated schematically as a function of crystal size (Figure 8) [103,105].

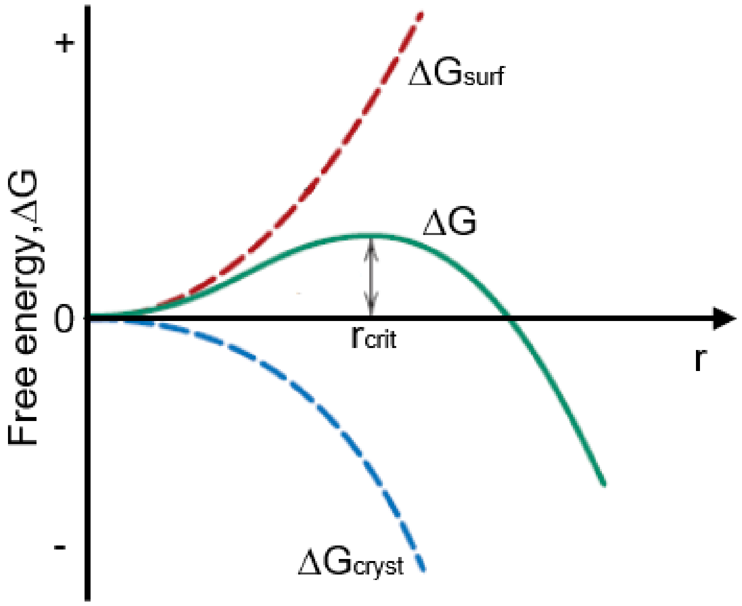

Figure 8: Schematic representation of the change of *Gibbs free energy* with the radius of nucleus during nucleation process. Scheme adopted from reference [107].

For a small embryo, the surface to volume ratio and surface energy of the embryo is high, which increases free energy [105]. As segments are incorporated into the embryo, the surface to volume ratio decreases and surface energy of the embryo is accompanied by increase of crystallization energy. At the critical minimum embryo size (r_{crit}), ΔG starts to decrease. Further aggregation of segments transforms the embryo into a stable nuclei, which might induce the spontaneous growth of crystals [103]. Thus, polymer crystallization takes place if the energy barrier is overcome.

Heterogeneous nucleation occurs much more often than homogeneous nucleation and takes place through the accumulation of polymer segments into insoluble particles in the polymer melt [103]. Heterogeneous nuclei can be dust particles, contaminations, or catalyst residues present in bulk polymer. Likewise, residual nuclei, which are present after incomplete melting of polymer, can cause self-nucleation on subsequent cooling. The surface energy in heterogeneous nucleation is lower, and therefore, the free energy needed to form a stable nucleus is reduced [108].

The acceleration of polymer crystallization by adding nucleating agents is a special case of heterogeneous nucleation whereby the nucleation density can be increased [109]. Hence, the spherulite size can be reduced and the nucleation process can be induced at higher temperatures. The crystallization temperature is a measure of the nucleating agent efficiency. The higher the crystallization temperature, the better is the efficiency of the nucleating agent.

1.4.2. Crystallization of PLA

PLA is a semi-crystalline polymer, where the crystallization is strongly influenced by copolymer ratio of L- and D stereoisomers [110]. As described in section 1.2.1 , the synthesis of a high molecular PLA is based on the lactide polymerization of three different stereoisomeric forms of lactide. L-lactide and D-lactide are made from either two L-lactates or D-lactates respectively, whereas meso-lactide (or LD-lactide) is a combination of L- and D-lactate. Depending on the production method, the amount of isomers in the final product differs [111]. Due to stereoregularity, PLA formed from either L- or D-isomer is highly crystalline with melting temperature between 170 and 180 °C [110,112,113]. It was shown that copolymerization of L-lactide with meso-lactide reduces the melting point and the glass transition temperature of PLA and inhibits PLA crystallization [110,112]. The PLA melting peak decreases by approximately 5 °C with every 1 % D-unit content, and PLA crystallization is two times slower with 3 % meso-lactide [26,112]. In addition, the PLA ability to crystallize is suppressed if the amount of meso-lactide exceed 15 % [110]. Moreover, the 50/50 L- and D-isomer mixture leads to irregular, amorphous material [110]. Therefore, PLA crystallization, melting point, glass transition temperature, and hence the resistance to elevated temperature during material utilization can be controlled by isomeric composition of PLA. Commercial and research focus is comprised mostly on PLA synthesized from L-rich mixture, because most of the lactic acid in nature is L-type [11]. However, the production of PLA with high stereochemical purity requires purification prior to polymerization, in order to separate meso-Lactide and D-lactide from the monomer mixture. Most of the commercial PLA grades contain a minimum of 1-2 % of D units due to purification issues, and thus, the PLA chain order is disturbed as the amount of D-form rises [26]. Another factor affecting PLA crystallinity is the sample molecular weight [114]. Due to restrictions in chain mobility, the spherulite growth rate of PLA decreases with increased molecular weight. Drastic changes can be observed only in low molecular weight samples (below 100 kg/mol) [114]. For PLA with molecular weight higher than 100 kg/mol, the impact of molecular weight on the spherulite growth rate is nearly constant and can be negligible [26,115]. Meaning that for commercial PLA grades with molecular weight of 100 kg/mol or higher, the difference in molecular weight plays a small effect on the crystallization rate. Similar conclusions can be drawn from the dependency of melting point on molecular weight. As PLA molecular weight exceeds 50 kg/mol, molecular weight does not affect melting temperature [116].

Fast cooling rates and short cycle time applied during industrial processing hinder the crystallization of PLA as a stand-alone material, and hence prevent PLA to be used for making durable parts that need to withstand higher temperatures. Therefore, increasing PLA crystallization rate would facilitate the reduction of cycle time and required energy in the injection molding process and thereby improve product performance [117].

1.4.3. Nucleating agents for PLA

Various inorganic, organic, and macromolecular nucleating agents have been found to enhance the crystallization of PLA. Talc is a classic example of inorganic nucleating agent for PLA, and is reported to have the best nucleation efficiency among the inorganic class of nucleators [118]. In the presence of 1 % talc, the crystallization half-time ($t_{1/2}$) at 100 °C is reduced to 90 s, which is approximately 27-fold faster than that for pure PLA [119]. Under non-isothermal experimental conditions, at a cooling rate of 10 °C/min, a high crystallization enthalpy (ΔH_{cm}) of around 40 J/g was measured at crystallization temperature (T_{cm}) of 104 °C. However, at a cooling rate of 20 °C/min, ΔH_{cm} was reduced almost by half and T_{cm} dropped to 94 °C. First, upon addition of 10 % talc, ΔH_{cm} of nearly 40 J/g was achieved at a cooling rate of 20 °C/min, although with T_{cm} below 100 °C [119]. Decreasing the cooling rate in the non-isothermal experiment to 1 °C/min triggered the crystallization of PLA with 3 % talc loading at 123 °C [120]. The ability of talc to enhance PLA crystallization could have been improved in combination with plasticizers. Combination of 1 % talc and 10 % of poly(ethylene glycol) (PEG) enabled to achieve ΔH_{cm} of approximately 36 J/g at a cooling rate as high as 80 °C/min. At the same cooling rate, PLA with 1 % talc and without PEG reaches ΔH_{cm} of only 6 J/g [119]. The chain movement from amorphous phase into crystal surface is enhanced due to plasticizer incorporation, and hence the crystallization process is improved.

The use of organic materials in comparison to inorganic ones might allow better dispersion and miscibility in the polymer matrix, and hence result in better performance [121]. Numerous studies focused on PLA performance nucleated with N,N’,N”-tricyclohexyl-1,3,5-benzenetricarboxylamide (TMC-328) are reported in the literature [31,34,122–124]. In PLA-melt, TMC-328 can be dissolved and self-assemble through intermolecular hydrogen bonding of the amides upon cooling into fine fibrils capable of nucleating PLA [124]. TMC-328 effectively promotes the nucleation of PLA, reducing $t_{1/2}$ at 120 °C from 61 min for pure PLA, to 2.87 min at the loading of 0.25 %, and 1.39 min at the loading of 1 % [123]. Enhanced crystallinity degree improved heat resistance of TMC-328 nucleated PLA by 2 fold as well as improved PLA oxygen barrier, which is nearly 3 orders of magnitude lower than that of the amorphous PLA [31,34]. Strong nucleation effect on PLA was noted with N,N’-ethylene bis(12-hydroxystearamide) (EBH) and N,N’-ethylene bis(stearamide) (EBS)[27,117,125,126]. With 2 % EBS loading, $t_{1/2}$ at 115 °C reduces by 21 fold, from 38.2 min for pure PLA with ~1.4 % D content to 1.8 min, whereas 1 % EBH loading reduces $t_{1/2}$ of PLA with 1.5-2 % of D isomer at 115 °C by 6.7 fold, from 18.8 min to 2.8 min [27,117]. However, a direct comparison of these two low-molecular weight aliphatic amides in the same PLA type reveals that EBH shows stronger nucleation ability than EBS, since $t_{1/2}$ for PLA doped with EBH is two times shorter than for PLA/EBS [126].

Oxalamide compounds are another class of nucleators for PLA [127,128]. It was proposed that oxalamide self-assembles into fibrillar structures via intermolecular hydrogen bonding upon cooling from the melt and prior to the solidification of PLA chains [128]. Subsequently, the fibrillar superstructures accelerate the crystallization of PLA. This behavior is similar to that described for amide compound [124]. The most effective oxalamide compound, N_1,N_1'-(ethane-1,2-diyl)bis(N_2-phenyloxalamide) (Oxa), at a loading of 0.75 % reduces $t_{1/2}$ of PLA with 2 % of D isomer at 135 °C from 40 min to 3 min, whereas under similar conditions, 0.75 % talc decreases $t_{1/2}$ to 21 min [127].

Organic compounds having hydrazide groups were identified as a strong nucleating agent for PLA [129–134]. In PLA with 1.6 % D isomer, 1 % loading of decamethylene dicarboxylic dibenzoylhydrazide enables to achieve T_{cm} and ΔH_{cm} of 131 °C and 46 J/ at a cooling rate of 20 °C/min. Under the same conditions, 1 % of Talc or EBD showed lower T_{cm} (102 and 110 °C, respectively) and ΔH_{cm} (26 and 35 J/g, respectively) [129]. Under non-isothermal experimental conditions, at a cooling rate of 2 °C/min, T_{cm} of PLA with 1.2-1.6 % D isomer shifts from 103 °C to 132 °C for PLA nucleated with 0.2 % tetramethylenedicarboxylic dibenzoylhydrazide (TMC-306) [130]. In addition, the results of isothermal experiment show that the introduction of 0.5 % TMC-306 into PLA gives rise to a reduction of $t_{1/2}$ from 146.9 min to 8.8 min at 145 °C, whereas at 130 °C crystallization of the nucleated PLA can be completed within 1 min [130]. Likewise, self-organization of the hydrazide compound into fibrils in PLA melt induces growth of PLA lamellae and favors PLA crystallization [130]. Similarly, phthalimide shows a positive effect on enhancing PLA crystallinity [135,136]. Upon cooling at 5 °C/min, the starting temperature of melt crystallization was increased from 112 °C for pure PLA with 2 % D isomer to 122 °C at the loading of 0.1 % phthalimide [135].

An interesting approach to improve crystallinity of PLA is by addition of orotic acid (OA), which is a bio-based chemical [137,138]. At the cooling rate of 10 °C/min, crystallization exotherm was hardly observed for neat PLA, whereas as little as 0.3 % OA promoted T_{cm} at 124 °C with ΔH_{cm} of 34 J/g. It is believed that the high efficiency of orotic acid to act as a nucleating agent for PLA is due to the good match between b-spacing of PLA and a-spacing of OA crystals [137].

The direct comparison of some of the above-mentioned nucleating agents, namely talc, TMC-306, Oxa, and OA, was performed in the same PLA matrix and under the same experimental conditions [118]. It was demonstrated that upon 0.5 % loading, the nucleation effect of the investigated nucleating agents for PLA is reduced in the order of OXA ≈ TMC–306 > TALC > OA [118].

The figure below summarizes the representatives of the most commonly reported classes of organic nucleating agents for PLA.

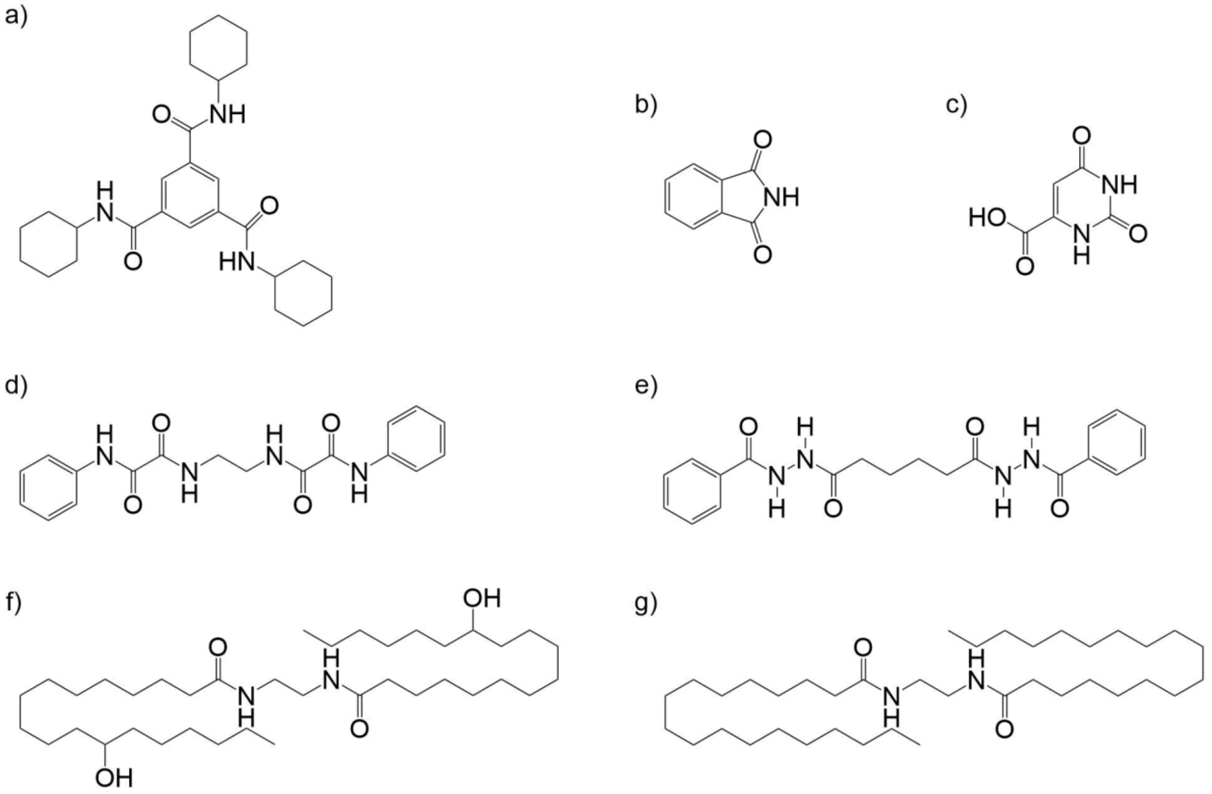

Figure 9: The chemical structure of a) multiamide compound (TMC-328), b) phthalimide, c) orotic acid, d) oxalamide compound (Oxa), e) hydrazide compound (TMC-306), aliphatic amide f) EBH, g) EBS.

2. Goal and strategy

PLA is a compostable polymer derived from renewable resources and has key advantages such as high melting temperature and high strength. On the downside, other characteristics of PLA - brittleness structure, low impact resistance, low heat distortion temperature, and low crystallization rate - limit its utility in several industrial applications. The properties of PLA are primarily linked to its L- to D- isomer ratio and its molecular weight. The properties of PLA are manipulated by the appropriate choice of additives and processing techniques.

The goals of the present thesis can be listed as follows:

1. Improving of the tensile properties of PLA without altering its degradation behavior.
2. Establishing a synthetic route to functionalize a hyperbranched polymer with a potential utility to compatibilize PLA/PE blends.
3. Improving the crystallization properties of PLA.

The first part of this chapter presents two distinct strategies based on the concept of polymer blending that specifically aim to improve the elongation at break of PLA. A synthetic route to functionalize a hyperbranched polymer is discussed that might lead to a new class of compatibilizers. The second part of this chapter introduces a custom-made nucleating agent to improve the crystallization rate of PLA. In addition, the nucleation efficiency of this custom-made nucleating agent is compared with that of commercially available nucleating agents.

2.1. PLA/PE binary blends

The strategy of blending PLA with different PE types to improve the mechanical properties of PLA has been widely reported [88–92]. The state-of-the-art work includes investigations of the change in the mechanical and thermal properties of PLA as a function of PLA/PE composition and in-process conditions [91,92,139–143]. In the present work, this PLA/PE blending strategy is deployed to examine the change in elongation at break of PLA as a function of varying PE types - HDPE, LDPE, LLDPE, and mPE. The focus is to gain a deeper understanding of the impact of the PE type on the morphology of PLA/PE blends.

A novel approach is introduced, which uses a calendar roller system at the die exit of an extruder to induce a uniaxial stretching effect in the PLA/PE blends. The speed of the calendar roller can be controlled, thus enabling control over the morphology of the dispersed phase. As far as is known, this is the first time that such a study is conducted. The morphology of PLA/PE blends is investigated via SEM and supported with first heating DSC scans.

2.2. Functionalization of hyperbranched polymers

Hyperbranched polymers with terminal functional end groups are attractive precursors for new polymeric materials. A large number of reactive sites per macromolecule provides feasibility to tailor the properties of the hyperbranched polymer to a desired application [76]. Within the scope of this research, a commercial hyperbranched polyester polyol (Boltorn™ HB20) is modified with a variable amount of stearic acid (SA) and PLA, and the resulting macromolecule is subjected to a detailed characterization. A method to quantify the degree of functionalization of PLA and SA onto Boltorn™ HB20 is introduced, and forms a very important part of this research. The chemical structure of Boltorn™ HB20 is shown in Figure 10.

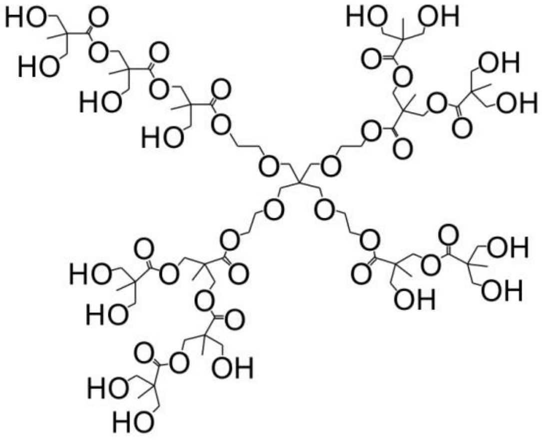

Figure 10: Chemical structure of Boltorn™ HB20.

The first step of derivatization involves partial modification of hyperbranched polyester hydroxyl end groups with stearic acid via a condensation reaction. In the second step, the remaining hydroxyl groups are modified with PLA during the extrusion process. The hypothesis is that the hyperbranched polymer functionalized with PLA and SA might enable in-situ compatibilization of the PLA/PE blends. The PLA part and the SA part of the modified hyperbranched polymer might facilitate good mixing of PLA and hydrophobic interactions with PE in the PLA/PE blend, respectively [144,145]. Thus, the hyperbranched compatibilizer can create a link between the two phases, potentially resulting in a better stress transfer, subsequently contributing to an improvement in the tensile properties of the PLA/PE blend.

The researches have demonstrated lactide polymerization in bulk using hyperbranched polyol as an initiator or via direct modification of the hyperbranched polyol with PLA in a discontinuous melting process [72,146,147]. The attempt to modify hyperbranched polymer with PLA in the presence of polyanhydride (PA) via reactive extrusion has also been explored [148]. Bhardwaj et al. reported in-situ crosslinking of hyperbranched polymer Boltorn™ H2004, which has six primary hydroxyl groups, with polyanhydride (PA) in a PLA melt. The results of his study indicated physical entanglement of the PLA chains in the network of Boltorn™ H2004 and PLA. However, Bhardwaj et.al could not confirm the reaction between PLA and Boltorn™ H2004 [148]. In the present thesis, the reaction between SA functionalized Boltorn™ HB20 and PLA is accelerated by the use of a suitable catalyst and carried out in an extrusion process. Boltorn™ HB20 and the subsequent functionalization with SA and PLA is intensively analyzed via ^{1}H-NMR spectroscopy.

2.3. PLA/PE ternary blends compatibilized with E-GMA

The researchers have reported that the addition of E-GMA to PLA/PE binary blends contributes to an improved compatibility between PLA and PE, and consequently, results in an improvement in the mechanical and thermal properties of PLA [95,97,99,100]. In the present thesis, the PLA/PE/E-GMA blending approach is used to investigate the changes in elongation at break of PLA as a function of changing PE type- LDPE, HDPE, LLDPE and mPE. The impact of the PE type and the amount of E-GMA in the blend composition on the morphology of the final blend is monitored in detail. The morphology of PLA/PE blends is investigated via SEM and supported with DSC.

PLA/mPE/ E-GMA ternary blends and PLA/mPE binary blends are subjected to a degradation study under natural weathering conditions. The impact of E-GMA and mPE on the degradation properties of PLA is investigated. TGA and IR spectroscopy as well as GPC analysis are used to track the changes in thermal properties and chemical nature of the blends, respectively, after exposure to hot and humid weather conditions in Eastern Australia.

2.4. Terephthaloyl-bis-N, N'-naphthalimidester – a novel nucleating agent for PLA

The mode of action of common nucleating agents used for PLA is based on self-assembly of the molecules into fibrillar structures via intermolecular hydrogen bonding [31,121,130,134]. In a self-assembly process, molecules or parts of molecules aggregate and get spontaneously organized into high ordered structures [149]. Non-covalent interactions are essential in the formation of structural assemblies [150,151]. Besides hydrogen bonding, $\pi \cdots \pi$ stacking interactions have been found to drive the molecular self-assembly process in benzoyl-terminated hyperbranched polymers (HBP) [149]. Jang et al. investigated the effect of terminal groups of HBP on the crystallization behaviour of poly(ethylene terephthalate) (PET) in PET/HBP blends, and found that HBP with phenyl-terminated groups function as the nucleating agent [152,153]. Cyclic aromatic imides and their derivatives are a potential class of molecules to guide the self-assemblies [154]. Aromatic imides are dipolar due to the presence of a relatively electron-rich aromatic unit connected to an electron-deficient imide ring, and this allows them to arrange in different ways in the crystal lattices. Terephthaloyl-bis-N,N'-naphthalimidester (TN) is a 1,8-naphthalimide derivate that was first developed as a flame retardant [155].

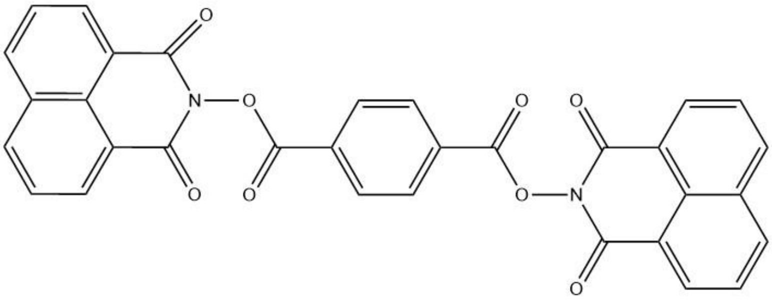

Figure 11: Chemical structure of Terephthaloyl-bis-N, N'-naphthalimidester (TN).

The motivation behind exploring TN as a nucleating agent for PLA lies in the molecular structure of TN. Different types of stacking interactions might appear from the positions and arrangement of the dipoles in the following order of stability : π-deficient···π-deficient > π-deficient···π-rich > π-rich···π-rich [156]. Figure 11 outlines the different stacking arrangements in 1,8-naphthalimide derivatives.

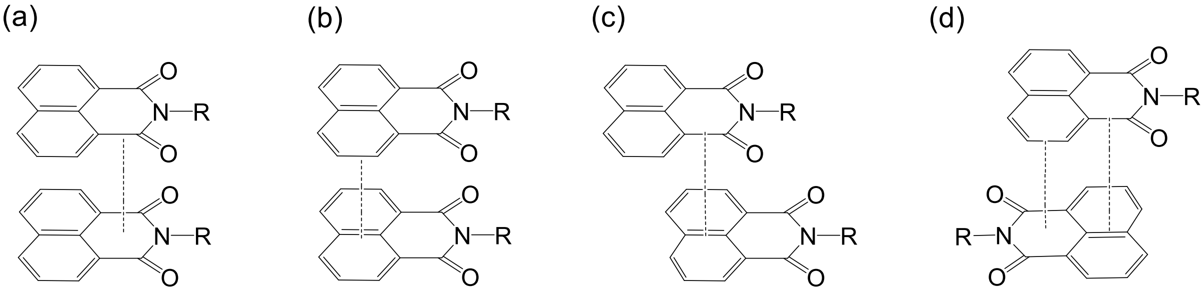

Figure 12: Stacking arrangements in 1,8-naphthalimide derivatives: (a) π-deficient···π-deficient, (b) π-rich···π-rich and π-deficient···π-rich stacking interactions, (c) head to head and (d) head to tail arrangements [154].

The hypothesis is that the naphthalimide planar groups might lead to self-assembly of TN molecules into parallel chains through π··· π stacking interactions. The parallel chains oriented to each other in a columnar arrangement, as superstructures, might accelerate the crystallization of PLA. The nucleating ability of TN under non-isothermal crystallization conditions is investigated in PLA, PLA/mPE binary and PLA/mPE/E-GMA ternary blends. In addition, the nucleating ability of TN under isothermal and non-isothermal crystallization conditions is compared against different commercially-available nucleating agents.

3. Polymer blending to achieve an improvement in the mechanical properties of PLA

The present chapter apprises an approach to improve mechanical properties of poly lactic acid (PLA), where PLA is blended with a suitable choice of dispersed phase, such as polyethylene (PE). The chapter is divided into two parts. The first part manifests the mechanical properties and morphology of the binary blends produced via an extruder that is equipped with a slit die and conveyor belt at the die exit. In the second part, the conveyor belt is interchanged with a calendar roller at the die exit. The impact of the calendar roller system on the mechanical properties and morphology of the resulting blends is investigated.

3.1. Tensile testing and morphology investigation of PLA/PE binary blends

PLA/PE binary blends were produced in a twin-screw extruder Process 11, operating in co-rotating mode and equipped with slit die and conveyor belt at the die exit. The extruded material was drawn continuously at a draw ratio of 2. The PLA used in the current research contains 96 mol % L-lactide and 4 mol % D-lactide. The dispersed phase in the blend composition was varied with the following PE types: HDPE, LDPE, LLDPE, and mPE. The physical properties of PLA and different PE types that were used in the composition of binary blends are listed in Table 1. The molecular weight and polydispersity of the polymers were measured with gel permeation chromatography (GPC). The degree of branching was obtained by using nuclear magnetic resonance spectroscopy (^{13}C-NMR), and the melting temperature was obtained by using differential scanning calorimetry (DSC). The density of the polymers was taken from the product data sheets provided by the supplier.

Table 1: Physical properties of PLA and different PE types used in the current research.

	Material				
Material Property	HDPE	LDPE	LLDPE	mPE	PLA
Mn (g/mol)	3.20×10^4	4.95×10^4	4.85×10^4	5.7×10^4	1.45×10^5
Mw (g/mol)	14.1×10^4	18.5×10^4	12.5×10^4	9.4×10^4	2.67×10^5
PDI	4.40	3.73	2.58	1.65	1.83
Branching degree (per 1000 carbon)	0	7 butylene, 4 amylene, 3 hexene or longer range chains	13 ethylene	10 butylene	-
ρ (g/cm³)	0.961	0.923	0.918	0.918	1.240
T_m (°C)	135	111	122	118	149

The blends were extruded at a constant PLA/PE weight ratio of 80:20 / wt% : wt%. Pure PLA and pure PE types were extruded as reference. The elasticity modulus and the elongation at break of the resulting blends were characterized in a tensile testing machine. The sample specimens for tensile testing (25 mm / 4 mm / 0.3-0.45 mm; length / width / thickness) were punched directly out of the extruded film. The elasticity modulus and elongation at break of PLA, different PE types and PLA/PE blends is shown in Table 2.

Based on the tensile test data summarized in Table 2, PE is a very flexible material with an elongation at break above 1000 % for HDPE, LLDPE and mPE and low elasticity modulus. HDPE has the highest modulus amongst the four PE types. PLA, on its own, is a very brittle material with poor elongation at break and a high elasticity modulus. Addition of PE to PLA results in a drop in elasticity modulus of PLA/PE blends, which could be due to the plasticizing effect that PE induces in the blend system. PLA/PE blends based on HDPE and LDPE exhibit minimal to no improvement in mechanical properties compared to that of pure PLA, which could be related to a brittle fracture behavior. On the contrary, addition of LLDPE and mPE to PLA shows significant improvement in the elongation at break compared to pure PLA and PLA/PE blends based on other PE types. Compared to 9 % elongation at break for pure PLA, 20 % LLDPE in PLA/LLDPE blend or 20 % mPE in PLA/mPE blend substantially improve elongation at break to 355 % and 364 %, respectively.

Table 2: Elasticity modulus and elongation at break of PLA, HDPE, LDPE, LLDPE, mPE and PLA/PE blends. The dispersed phase in the blend composition consists of either HDPE, LDPE, LLDPE or mPE.

Sample	Composition (wt% / wt%)	Elasticity Modulus (MPa)	Elongation at break (%)
PLA	100	1810 ± 188	8.6 ± 1.9
HDPE	100	641 ± 133	1073 ± 276
LDPE	100	142 ± 18	610 ±78.7
LLDPE	100	139 ± 9	1408 ±118
mPE	100	143 ± 16	1392 ± 83
PLA/HDPE	80/20	1590 ± 95	11 ± 8
PLA/LDPE	80/20	1330 ± 29	5 ± 0.8
PLA/LLDPE	80/20	1400 ± 69	355 ± 34
PLA/mPE	80/20	1390 ± 78	364 ± 30

Scanning electron microscopy (SEM) was used to conduct morphological analysis of PLA/PE blends on the cryofractured surface of extruded films. The fractures were prepared perpendicular to the machine direction. Figure 13 shows the distinct morphology of the different PLA/PE blends. PLA/HDPE and PLA/LDPE blends reveal large globules of PE dispersed in the PLA matrix as shown in Figure 13a and 13b, respectively. The presence of large globules in the PLA matrix could indicate poor interfacial adhesion between blend components [91,139,141]. PLA/LLPDE (Figure 13c) and PLA/mPE (Figure 13d) blends show noticeably different blend morphologies, where PE is present in the form of elongated microfibrils. A very low elongation at break of PLA/HDPE and PLA/LDPE could be associated with weakly-adhered HDPE and LDPE in the PLA matrix, seen as large globules in SEM images. On the other hand, elongated microfibrils of LLDPE and mPE interpenetrating into the PLA matrix well explains a drastic increase in elongation at break of the resulting blends.

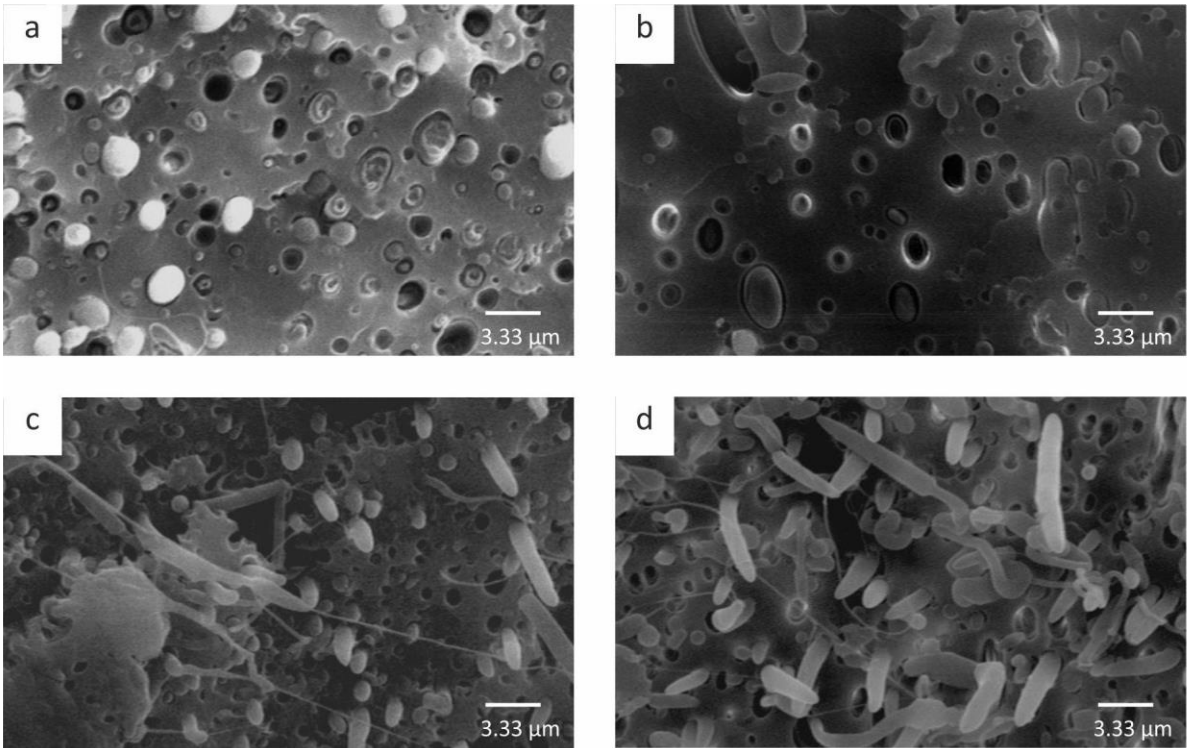

Figure 13: SEM morphologies of cryogenically-fractured surfaces of 80:20 /wt%: wt% blends of (a) PLA/HDPE, (b) PLA/LDPE, (c) PLA/LLDPE and (d) PLA/mPE.

As the PLA/mPE blend exhibited substantially high elongation at break as compared to pure PLA, it was of interest to determine the minimum loading in PLA that guarantees a high elongation at break, without compromising much on the elasticity modulus of PLA. Here, another reason for choosing mPE over LLDPE was found because PLA/mPE has a larger number of fibrillar structures as compared to those in the PLA/LLDPE blend. Four blends of PLA/mPE were prepared with different amounts of mPEs ranging from 20 wt-% to 5 wt-%. The composition and tensile test results of the different PLA/mPE blends are shown in Table 3.

Table 3: Composition, elasticity modulus and elongation at break of different PLA/mPE blends.

Sample	Composition (wt% / wt%)	Elasticity Modulus (MPa)	Elongation at break (%)
PLA	100	1810 ± 188	8.6 ± 1.9
PLA/mPE	80/20	1390 ± 78	364 ± 30
PLA/mPE	85/15	1540 ± 40	191 ± 98
PLA/mPE	90/10	1670 ± 92	112 ± 107
PLA/mPE	95/5	1840 ± 29	69 ± 45

The elasticity modulus of PLA/mPE blends is lower than elasticity modulus of pure PLA and it decreases as the amount of mPE loading increases. The elongation at break of the PLA/mPE blend is the highest for the blend comprising of 20 % mPE and the lowest for the blend comprising of 5 % mPE. The elongation at break increases gradually with the increasing amount of mPE in the blend composition. Even a 5 % mPE loading in PLA has significantly higher elongation at break as compared to that of pure PLA, PLA/HDPE and PLA/LDPE blends as summarized in Table 2. However, considering the standard deviation in elongation at break, minimum 20 % mPE loading in the PLA matrix is required in order to obtain a distinctly higher elongation at break as compared to pure PLA.

Following the analysis of mechanical properties, the morphology of PLA/mPE blends listed in Table 3 was studied. Figure 14 shows the cryogenically-fractured surface of PLA/mPE blends comprising different amounts of mPE loading in the PLA matrix.

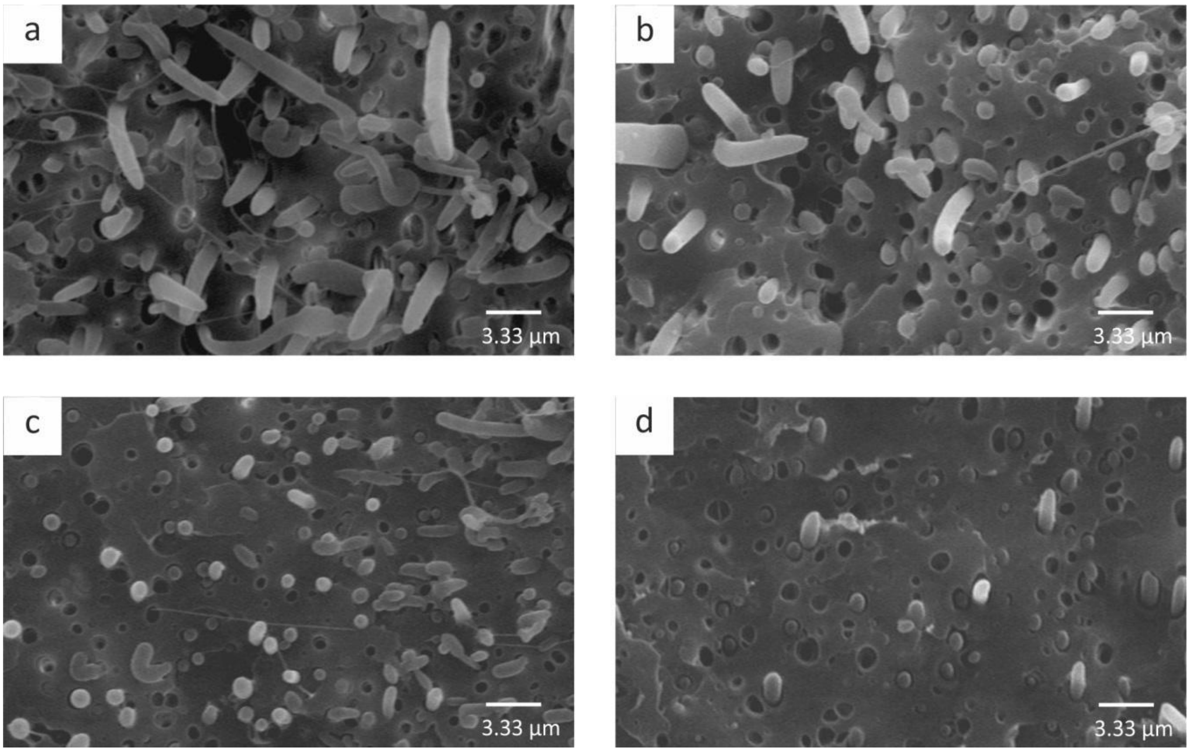

Figure 14: SEM morphologies of the cryogenically-fractured surface of (a) 80/20, (b) 85/15, (c) 90/10 and (d) 95/5 wt%/ wt% of PLA/mPE binary blends.

As shown in Figure 14, PLA/mPE blends with 20 % (Figure 14a) and 15 % (Figure 14b) mPE amount are rich in long microfibrils, which might contribute to a satisfactory transfer of stress in the system and result in high elongation at break. PLA/mPE blends with lower mPE amount, such as 10 % (Figure 14c) and 5 % (Figure 14d) are dominated by globular structures and few microfibrils, which could explain the drop in elongation at break due to a weak stress transfer in the blend system. This is notably seen in the case of PLA/mPE blend with 5 % mPE loading.

3.2. Effect of drawing method on the morphology of PLA/PE binary blends

In the previous section, a significant difference was reported in the tensile properties of PLA/HDPE and PLA/mPE blend and the difference could be correlated to the morphological features of individual blends. In an effort to study the impact of the drawing method on morphological features, and thereby on mechanical properties of PLA/HDPE and PLA/mPE blends, the conveyor belt at the die exit was interchanged with a calendar roller system, that has a better precission. The calendar roller system is equipped with three calendar rollers that generate an elongation flow field on the extruded material.

Each of the two blends was extruded under three different conditions. In one case, the extruded material was directly cooled in a water bath. In the other two cases, the extruded material was drawn continuously at a draw ratio of 4.5 and 9.0. Figure 15 shows SEM micrographs of the cryogenically-fractured surface of PLA/HDPE and PLA/mPE binary blends. The SEM micrographs of the cryogenically-fractured surface of PLA/HDPE blends and PLA/mPE blends, cooled in a water bath post extrusion are shown in Figure 15a and Figure 15b, respectively. Figure 15a' and Figure 15b' are SEM micrographs of PLA/HDPE blends and PLA/mPE blends drawn at a ratio of 4.5 post extrusion, whereas Figure 15a" and Figure 15b" are SEM micrographs of PLA/HDPE and PLA/mPE blends at a ratio of 9 post extrusion.

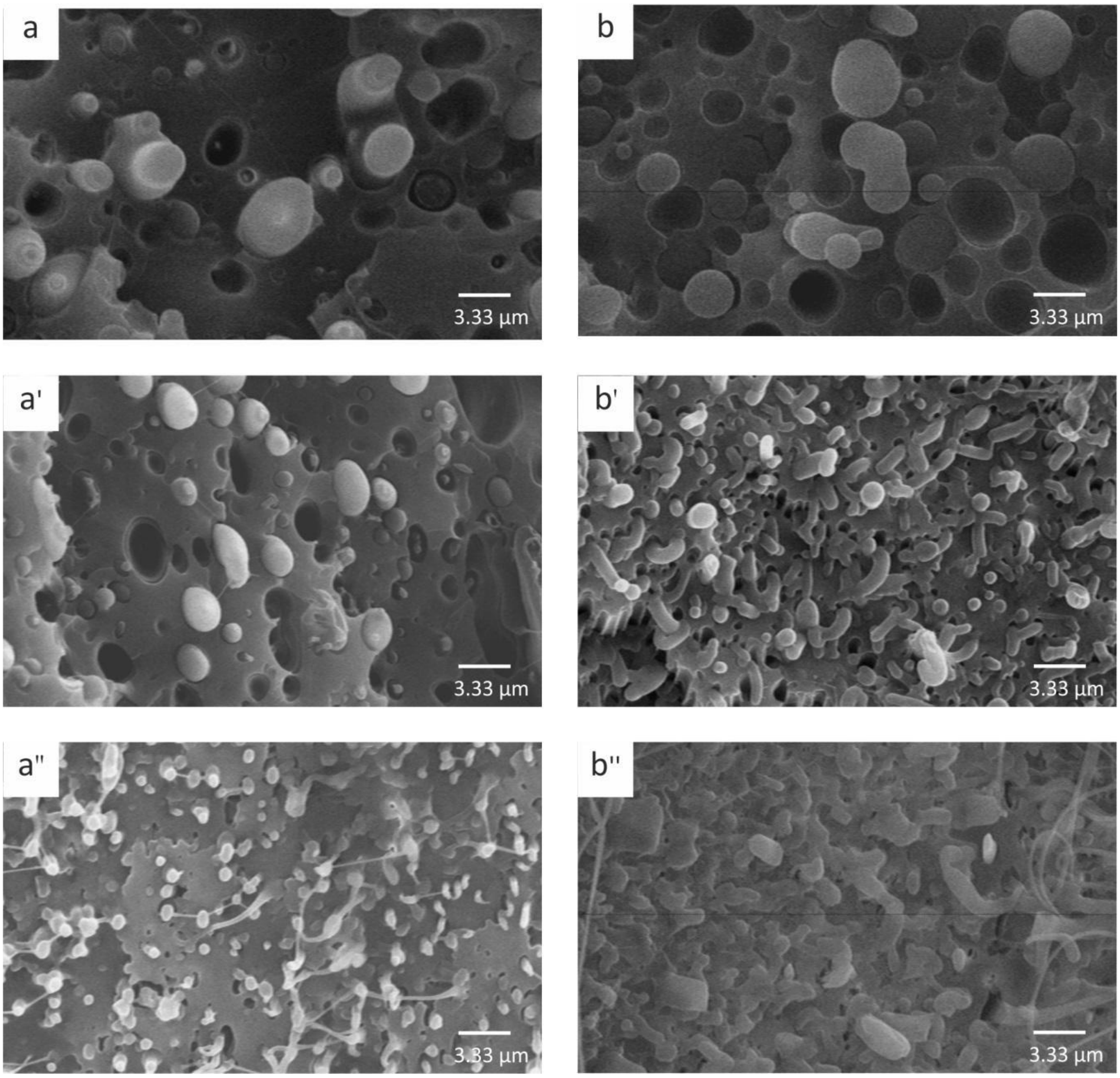

Figure 15: SEM micrographs of the cryogenically-fractured surface of binary blends (a) PLA/HDPE an (b) PLA/mPE cooled in a water bath post extrusion; (a') PLA/HDPE and (b') PLA/mPE drawn at a draw ratio of 4.5 post extrusion;(a'') PLA/HDPE and (b'')PLA/mPE drawn at a draw ratio of 9 post extrusion.

The PLA/HDPE (Figure 15a) and PLA/mPE (Figure 15b) blends, which were cooled directly in a water bath post extrusion, show spherical morphology, large PE domains that are dispersed in PLA matrix, and a diameter of approximately 3 μm. The smooth and distinct particle interface, irrespective of the choice of dispersed phase, indicates poor interfacial adhesion.

As soon as the calendar rollers are introduced at the die exit, the blend morphology is tailored and the calendar rollers continuously draw the extruded material into films. The morphology of the PLA/HDPE (Figure 15a') drawn through the calendar rollers at a ratio of 4.5 is still marked by spherical domains of dispersed PE phase. The lack of adhesion between PLA and PE is evidenced by several PE particles being pulled out of the PLA matrix. The size of HDPE droplets is reduced to approximately 1.5 µm due to the extensional strain. As the dispersed phase is changed from HDPE to mPE, a noticeably different type of morphology is observed at the draw ratio of 4.5 (Figure 15b') as compared to that of the non-stretched binary blend. Droplet deformation into elongated particles and their coalescence into the network is assumed as soon as uniaxial stretching is introduced. The morphology of the PLA/mPE blend indicates finer dispersion with fewer cavities on the cryofracture surface, in contrast to the SEM images of the PLA/HDPE blend. The average diameter of the fibrils is 0.75 μm.

As the draw ratio is increased from 4.5 to 9, the PLA/mPE morphology (Figure 15b") remains intact with less cavities being observed on the cryofractured surface. The PLA/HDPE blend undergoes more intensive stretching deformation, which results in a stepwise breakdown into smaller droplets. Subsequently, a larger number of smaller droplets are observed (figure 15a") in combination with droplets bridged through thin fibrillar structures. It appears that at a critical stretching deformation, the bridge holding the droplets breaks, resulting into separate droplets. The morphology development in the PLA/mPE and PLA/HDPE blends upon the post-extrusion is a result of two different mechanisms. While mPE particles can arrange themselves in the direction of uniaxial stretching and merge to form long elongated particles, HDPE droplets separate into smaller droplets. A scheme for the morphology development in the PLA/HDPE and PLA/mPE blends is proposed in Figure 16. A further rheological investigation is required in order to explain this phenomenon, which was not in the scope of this work.

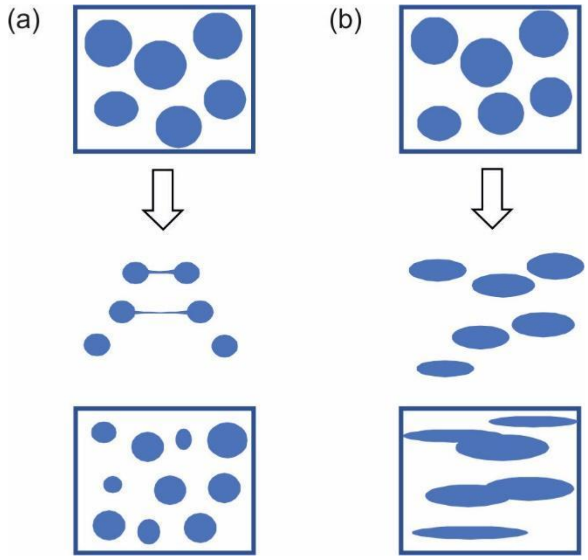

Figure 16: Schematic of morphology development for a) PLA/HDPE and b) PLA/mPE blend during post-extrusion drawing.

The first heating DSC scans of the PLA/HDPE and PLA/mPE blends were obtained to support the findings from the morphological studies. The first heating DSC was chosen as the appropriate method because the thermograms of the first heating DSC scan are defined by the processing-related heat history. Figure 17 shows DSC thermograms of the PLA/mPE (curve a, b and c) and PLA/HDPE blends (curve d, e and f) recorded at heating rate of 10 °C/min. All the thermograms are very similar and reflect the glass transition (T_g) of PLA and the melting temperature (T_{mI}) of PE that overlaps with the cold crystallisation peak (T_{cc}) of PLA and a subsequent melting peak of PLA (T_{mII}). The overlap of the T_{cc} with the melting peak of PLA indicates that the exact determination of T_{cc} and crystallinity is not possible.

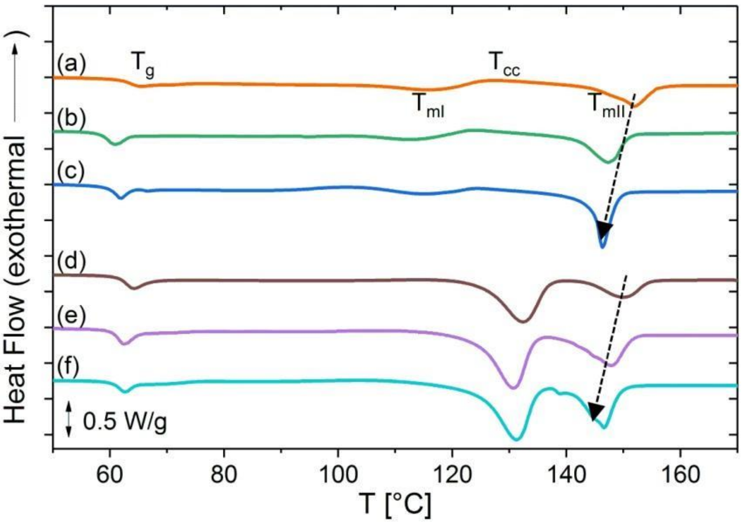

Figure 17: DSC heating curves of 80/20 PLA/mPE drawn at a draw ratio (a) 0, (b) 4.5, (c) 9 and 80/20 PLA/HDPE blends drawn at a draw ratio (d) 0, (e) 4.5, (f) 9 m/min, recorded at a rate of 10 °C/min.

Table 4: Thermal parameters obtained from DSC heating scan of PLA/mPE and PLA/HDPE blends prepared at different draw ratios.

Sample	Draw ratio	T_g [°C]	T_{mI} [°C]	T_{mII} [°C]
PLA/mPE	-	64	115	152
	4.5	61	113	147
	9	59	114	146
PLA/HDPE	-	62	132	150
	4.5	61	130	148
	9	60	131	147

As shown in Table 4, T_{mII} of the PLA phase in the non-drawn PLA/mPE blend is 152 °C and it decreases to 147 °C as the extrudate is fed to the calendar roller operating at a draw ratio of 4.5. This 5 °C drop in T_{mII} with implementation of the calendar roller system could be attributed to the plasticizing effect of mPE due to better distribution of mPE in the PLA matrix. This drop is seen in Figure 15b' and is in contrast to Figure 15b, which shows the non-drawn PLA/mPE blend. As the draw ratio is increased from 4.5 to 9, the melting peak of the PLA phase in the PLA/mPE blend becomes narrower and a minor drop in melt temperature by 1 °C is observed. In addition, T_g of PLA in the PLA/mPE blend decreases with an increase in the calendar roller speed, and this is a clear indication of reduced rigidity of the mPE blend.

In case of the PLA/HDPE blend, the drop in T_{mII} of PLA in the PLA/HDPE blend is not as strong as in the case of the PLA/mPE blend. T_{mII} of the non-drawn PLA/HDPE blend is 150 °C and it decreases to 148 °C, which is only a 2 °C difference, as the extrudate is fed to the calendar roller operating at a draw ratio of 4.5. A further increase in draw ratio to 9 results in a reduction in T_{mII} by 1 °C. This minimal drop in T_{mII} could be attributed to weakly-adhered HDPE dispersed phase in PLA matrix, and is seen as globular particles in Figure 15a' and Figure 15a". In addition, T_g of PLA in PLA/HDPE blend does not exhibit a significant decrease with an increase in the calendar roller speed, and indicates rigidity of the HDPE blend.

3.3. Summary on polymer blending towards improvement in the mechanical properties of PLA

In this chapter, it was demonstrated that the tensile properties of the PLA/PE binary blends, which were produced using an extruder equipped with slit die and conveyor belt at the die exit, strongly depend upon the nature of the dispersed PE phase. The elongation at break of pure PLA was significantly enhanced by dispersing LLDPE or mPE in the PLA matrix without much compromise on the elasticity modulus of PLA. The most significant improvement was obtained with as less as 20 % mPE in the blend composition, yielding a 42-fold increase in elongation at break over neat PLA. The difference in elongation at break of various PLA/PE blends was explained through SEM morphological studies. The exceptionally high elongation at break of PLA/mPE and PLA/LLDPE is related to the microfibrils of mPE and LLDPE having interpenetrated into the PLA matrix, thereby holding the system together. On the contrary, the low elongation at break of PLA/HDPE and PLA/LDPE could be related to the globules of HDPE and LDPE being weakly adhered to the PLA matrix. The morphology of PLA/PE binary blends was tailored by introducing a calendar roller system at the die exit and by adjusting the speed of the calendar rollers. DSC experiments on the PLA/mPE and PLA/HDPE binary blends confirmed that increasing calendar roller speed has a plasticizing effect on mPE, which eventually improved the tensile properties of PLA/PE binary blends.

4. Hyperbranched polyester polyol modified with stearic acid and polylactic acid as a potential compatibilizer for PLA/PE bends

4.1. General remarks

The present chapter reports development of hetero-armed hyperbranched polymers that could be potentially used as an in-situ compatibilizer for PLA/PE blends. The hyperbranched polymer used in the current research is a hyperbranched polyester polyol that is functionalized with stearic acid (SA) and PLA in a two-step process. The chapter is split into two subparts. The first part describes the chemical structure of the hyperbranched polymer prior to the modification of the hyperbranched polymer with SA and PLA. A model study to determine the efficiency of –OH group conversion of the hyperbranched polymer is introduced. This step is crucial to monitor the chemical changes occurring in hyperbranched polymers following the subsequent chemical modifications. The second part of this chapter describes the synthesis and characterization of SA and PLA functionalized hyperbranched polymers. The model study is applied to determine the extent of SA and PLA functionalization onto hyperbranched polymer.

4.2. Determination of degree of functionalization of hyperbranched polyester polyol

Boltorn™ HB20 (H0) - a commercially available hyperbranched polyester polyol - is selected as a scaffold, which is later functionalized with trichloracetylisocyanate (TAI). H0 functionalized with TAI serves two purposes: a) it acts as a model system to evaluate the efficiency of –OH group functionalization and b) it is used to explain H0 modification with SA and PLA.

4.2.1. Characterization of the hyperbranched polyester

This section discusses the synthesis of H0, and potential side reactions that could occur during the synthesis. H0 is a hydroxyl-functional aliphatic polyester having a theoretical core/monomer ratio of 1/12, an average of 16 -OH groups per macromolecule, and belongs to the second generation of hyperbranched polyesters [157]. It is synthesized from a tetra functional B_4 core molecule, ethoxylated pentaerythritol (PP50), tri-functional AB_2 type monomer, and 2,2-bis-methylolpropionic acid (bis-MPA), as the repeating unit. Figure 18 depicts a typical chemical structure of H0.

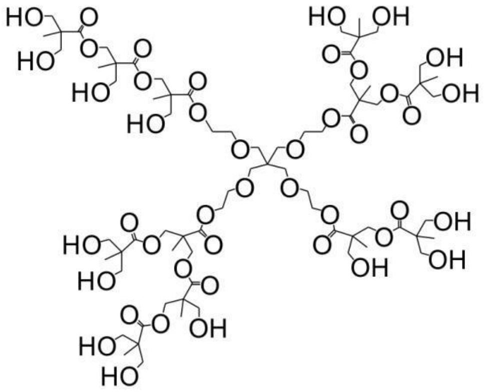

Figure 18: Chemical structure of Boltorn™ HB20 (H0).

One of the main side reactions during synthesis of hyperbranched polyesters based on bis-MPA, is self-condensation of monomers (Figure 19) [157]. This side reaction leads to the formation of hyperbranched structures having low molar mass and without a core molecule [158]. The branches have one unreacted carboxyl group in either focal linear or focal dendritic units [157,158].

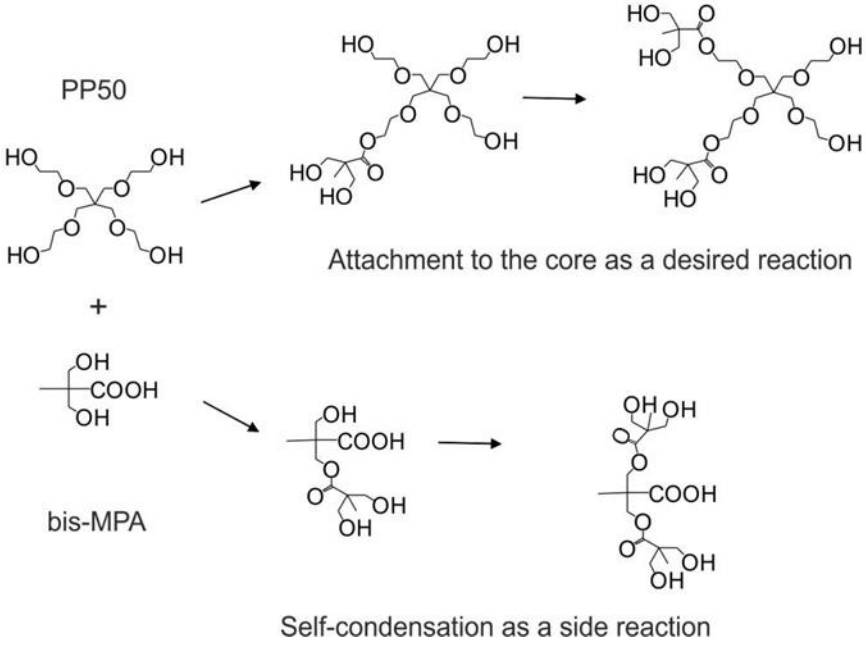

Figure 19: Schematic representation of possible pathways of hyperbranched polyester growth and self-condensation as a side reaction [158].

Moreover, the presence of cyclic species has been reported in poly (bis-MPA) with and without the core unit [157–161]. The cyclization reactions occur due to intramolecular esterification, intramolecular etherification and intramolecular hydroxyl-ester interchange [158]. Additional side products can be formed by intermolecular reactions [158]. Figure 20 is an example schematic of possible side reactions in poly (bis-MPA) with and without a core unit.

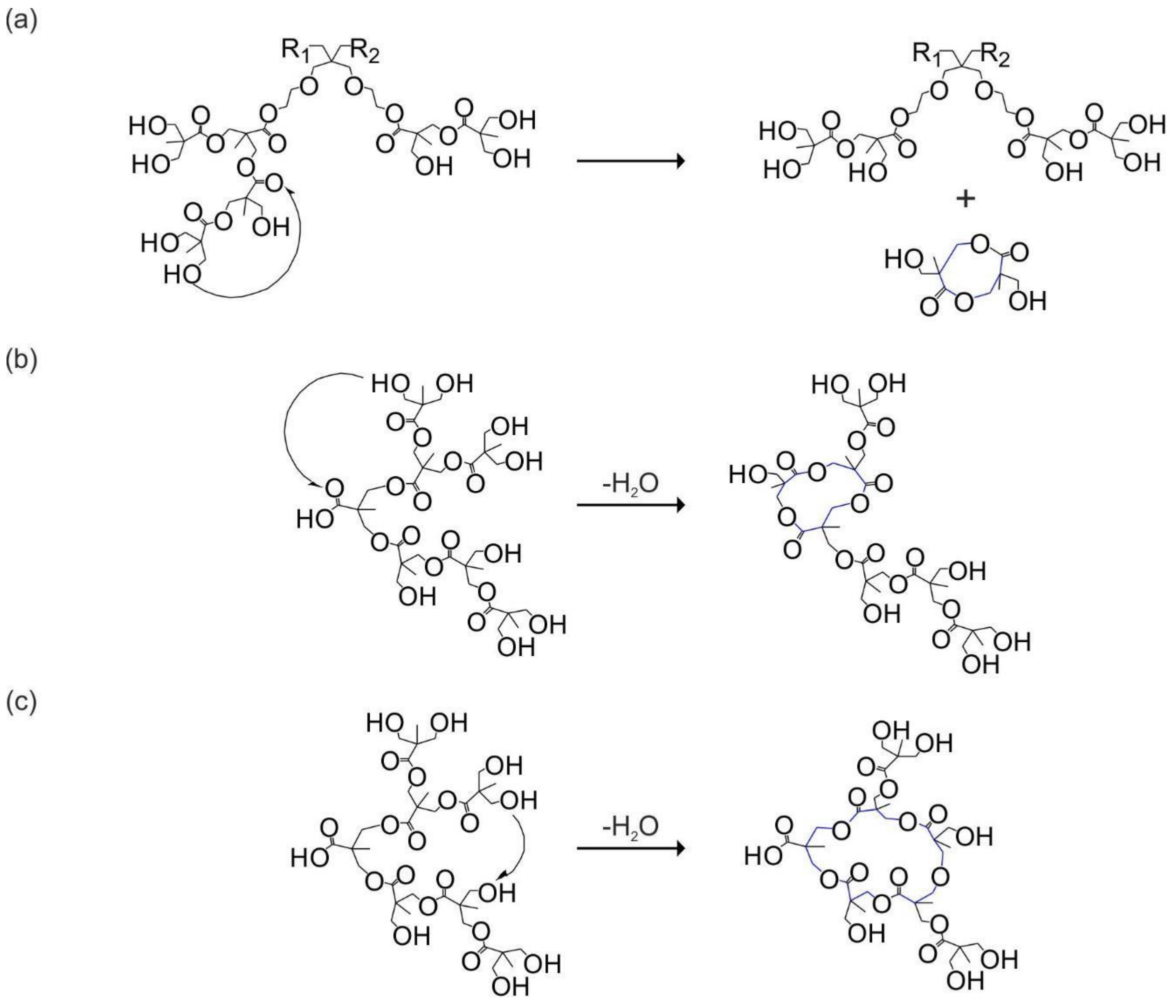

Figure 20: Schematic representation of possible side reactions in poly (bis-MPA) with core unit: (a) intramolecular hydroxyl-ester interchange between groups of the same branch and without core unit: (b) intramolecular esterification, (c) intramolecular etherification [158,159].

The hyperbranched structures without a core unit as well as cyclic structures have been reported in different generations of Boltorn™ polyesters, including H0 that is used in the present study [157,161]. Co-existing hyperbranched structures with a core unit and cyclic structures indicate a polydispersed hyperbranched polyester with respect to its structure and molar mass [157,159].

4.2.2. TAI model to determine the degree of H0 functionalization

Before H0 was functionalized with TAI, it was of interest to characterize pristine H0 via ^{1}H-NMR, although different generation of commercial hyperbranched polyesters from Perstorp have been characterized in recent publications [157,161–165].

A detailed characterization of H0 would support to distinguish ^{1}H-NMR signals of neat H0 from H0 functionalized with TAI, SA and PLA in the following sections. For ^{1}H-NMR characterization, H0 was dissolved in DMSO-d_6. Figure 21 shows ^{1}H-NMR spectrum of H0 along with the proton assignment.

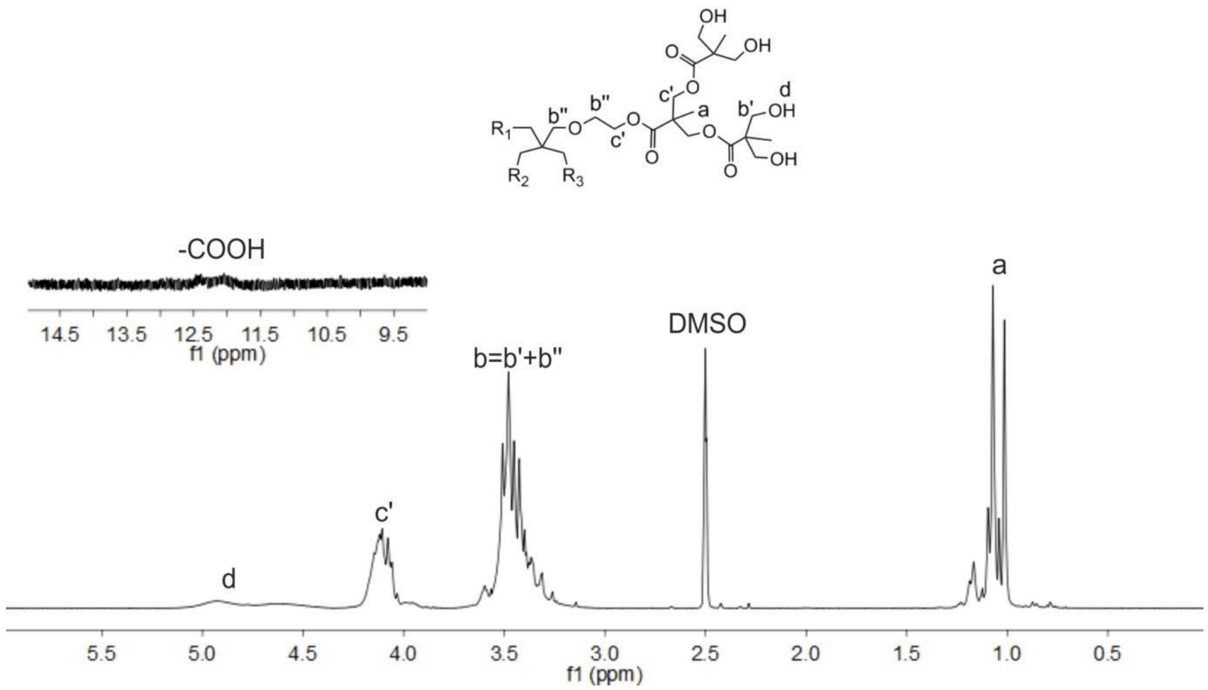

Figure 21: ^{1}H-NMR spectrum of Boltorn™ H0 in DMSO-d_6 along with a magnified signal in low magnetic field.

The resonance *a* at 1-1.25 ppm corresponds to methyl groups (-CH_3) of dendritic, terminal and linear units, whereas signal *b* at 3.2-3.7 ppm originates from the methylene groups linked to hydroxyl groups (-CH_2-OH) (signal *b'*) and methylene ether groups (-CH_2-O-) (signal *b''*). The origin of ether protons might be not only from the core, but also formed in side reactions during H0 manufacturing, as presented in Figure 20 [158–161]. Signal *c'* at 3.8-4.25 ppm corresponds to methylene ester groups(-CH_2-OCO-). The broad signals at *d* (4.61 and 4.91 ppm) correspond to –OH groups in terminal and linear repeat units, respectively. The broad signal in ^{1}H-NMR spectrum at 12 ppm could be related to the presence of unreacted carboxyl groups in H0, which might confirm the appearance of the side products due to self-condensation of bis-MPA [146,157,166]. In Figure 21, the integral of signal *a* is normalized to 1H. Table 5 summarizes the integral intensity of different peaks obtained in Figure 21 and the expected integral intensity of those peaks in case of an ideal structure of H0.

Table 5: Summary of the signals from Figure 21 with integral intensity and expected relative intensity for an ideal structure. The reference signal is represented by *.

Peak	Integral intensity	Expected integral intensity for an ideal structure
a*	1	1
b (b '+ b")	1.60	1.33
c'	0.59	0.67
D	0.19	0.44

As shown in Table 5, there is a deviation between expected and actual signal intensities of H0, which could be due to the presence of impurities in H0 used in the present work. In addition, the residual moisture as well as labile protons (-OH groups), which are not fully separated from the signal *c'* ($-CH_2-OCO-$), are a challenge in assigning an exact signal intensity. The functionalization of H0 with TAI involves rapid reaction between TAI and the hydroxyl end groups of polyester, thus yielding an urethane derivative as shown in Figure 22. Due to the reaction, the signals corresponding to –OH groups disappear from the ^{1}H-NMR spectrum [167]. In addition, excess of TAI reacts with moisture yielding trichloracetamide and generates a signal at ~ 6 ppm, which therefore do not interfere in the region of the interest. Because TAI is an aprotic agent, excess TAI does not show any additional signal in spectrum [168].

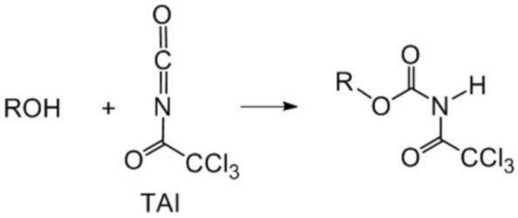

Figure 22: Schematic reaction of hydroxyl (-OH) groups with (TAI) [167].

The reaction between H0 and TAI occurs easily. Therefore, the in-situ derivatization of hydroxyl end groups of the polymer is performed in an NMR tube and is completed within 10 minutes [168]. Figure 23 shows the ^{1}H-NMR spectrum of H0 after derivatization with TAI.

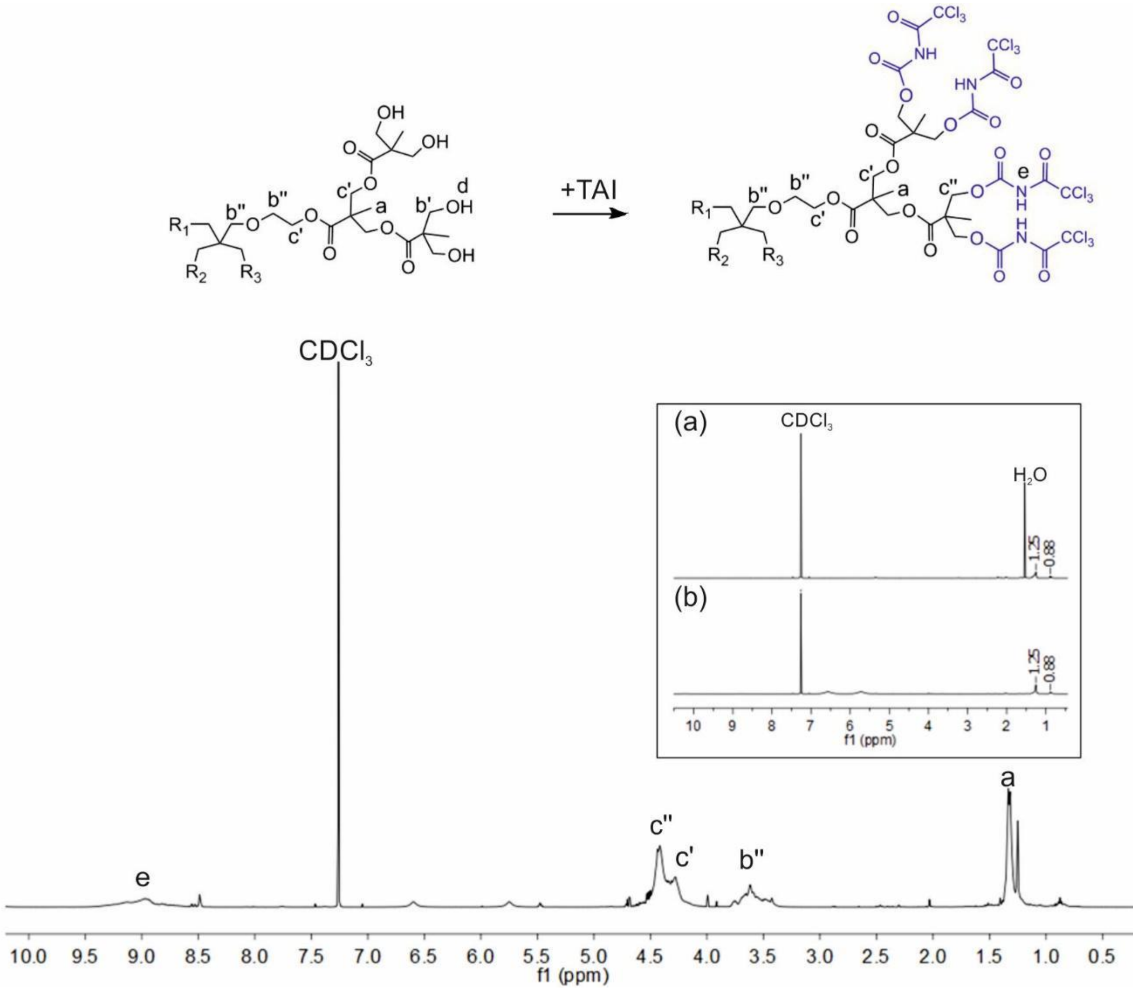

Figure 23: ^{1}H-NMR spectrum of TAI derivatized H0 in $CDCl_3$. ^{1}H-NMR spectrum of a) $CDCl_3$ and b) $CDCl_3$ after addition of TAI is captured in the frame.

After reaction with TAI, signal *b'* corresponding to the methylene α to the hydroxyl groups ($-CH_2-OH$) disappears. Instead, a new signal *c''*, which overlaps with the signal *c'* of the methylene α to ester groups, arises at 4.4 ppm. The signal *c''* corresponds to the protons adjacent to TAI-terminated functional end groups in H0. The chemical shift of *c''* is in agreement with the chemical shift of α-hydrogens of TAI-derivatized model compounds with hydroxyl end groups, as reported in the literature [168]. Signal *b'* disappears from ^{1}H-NMR spectrum due to the total termination of hydroxyl groups upon completion of the reaction, and signal *b''* corresponding to the ether protons remains unaltered [169]. Moreover, derivatization of hydroxyl end groups with TAI yield a broad signal *e* at 8.5 -9.5 ppm, which is attributed to the imidic hydrogen of the derivatized end groups. Two singlets at 5.7 and 6.6 ppm are due to trichloracetamide. For clarity, portions of the ^{1}H-NMR spectra of H0 and TAI-terminated H0 are presented with magnified signals in the low magnetic field, as shown in Figure 24. Due to traces of impurities in the deuterated NMR solvent ($CDCl_3$) at 1.25 ppm and 0.88 ppm, the intensity of signal *a* at the resonance 1.2-1.4 is not included in the further discussion.

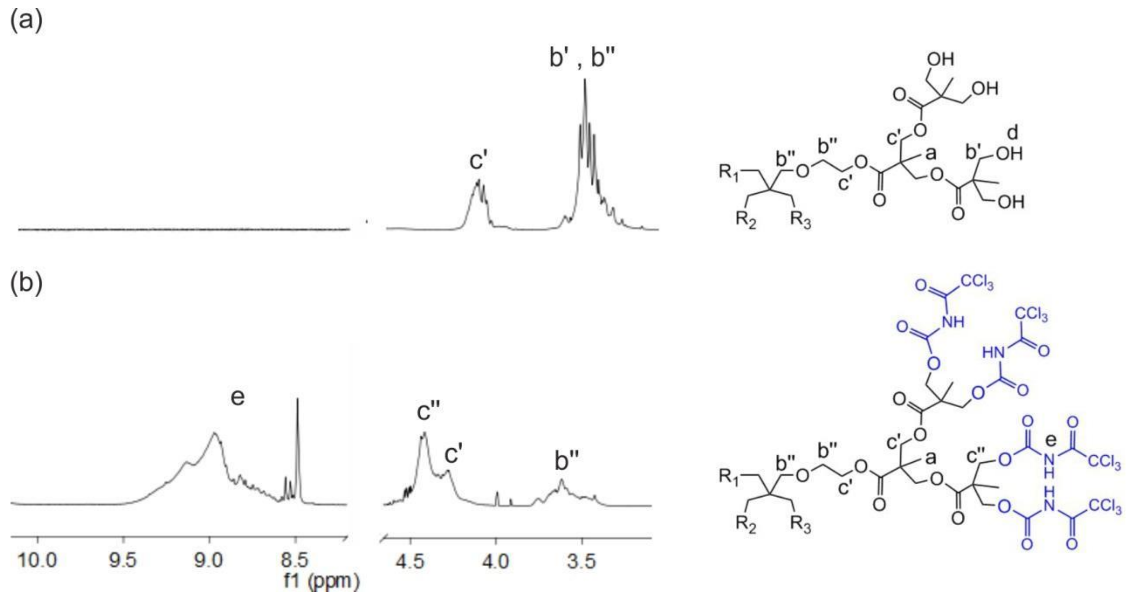

Figure 24: Portion of ^{1}H-NMR spectrum: (a) H0 in DMSO-d_6 and (b) TAI-terminated H0 (H0-TAI) in $CDCl_3$ with magnified signals in the low magnetic field.

Due to the termination of –OH groups, methylene protons of hydroxyl group of H0 (b') are transformed to methylene protons of TAI-terminated functional end groups (c''), and this is given in equation 4. Equation 5 presents the relation between intensity of signal e and b'.

$$I_{b'} = I_{c''} \tag{4}$$

$$I_e = I_{b'}/2 \tag{5}$$

Table 6 summarizes the intensity of signals from Figure 23 and the expected relative intensity for an ideal H0 structure functionalized with TAI. The sum of integral signals b'', c' and c'' were normalized to 1H. Table 6 shows the deviation between the integral intensities of experimental H0 and ideal H0, which are derivatized with TAI. The deviation might be due to the polydisperse nature of H0 in context of its chemical structure. Nevertheless, based on the signal e for the imidic hydrogen of derivatized end groups, a maximum conversion of -OH groups in pristine H0 can be established.

Table 6: Summary of the integral intensity of signals from Figure 23 and the expected relative intensity for an ideal structure terminated with TAI. * represents a reference signal.

Peak	Integral intensity	Expected integral intensity for an ideal structure
(b”)*	0.26	0.22
(c ’+ c”)*	0.74	0,78
e	0.22	0.22

Knowing the signal intensity of *e* (see Table 6), the integral intensity of *b'* can be calculated using equation 5 as

$$I_{b'} = 0.44 \text{ H} \tag{6}$$

The integral sum of (*c'* and *c"*) and *b"* of TAI-terminated H0 is 1 H. Thus, the integral intensity of *c'* can be obtained using equation 7, and the integral intensity of *b* can be obtained using equation 9.

$$I_{c'} = (I_{c'} + I_{c''}) - I_{b'} \tag{7}$$

$$I_{c'} = 0.3 \text{ H} \tag{8}$$

$$I_{b} = I_{b'} + I_{b''} = 0{,}7 \text{ H} \tag{9}$$

4.3. Synthesis and Characterization of H0 modified with stearic acid

The first step of H0 derivatization involves synthesis of stearic acid-grafted H0 (H0-SA) through a condensation reaction of H0 hydroxyl groups and SA carboxyl groups. SA was added to H0 in molar ratios of H0:SA 1:8 (H08) and 1:12 (H12). It is likely that due to the under-stoichiometric condition of SA carboxyl to H0 hydroxyl groups, not all hydroxyl groups react, leaving behind un-reacted hydroxyl groups. Thus, the second step of PLA derivatization could lead to the modification of the unreacted hydroxyl groups (see section 4.5).

Following the H0-SA modification reaction, TGA on H08 and H12 (see Figure 25) was performed in order to verify the absence of residual SA. The thermal stability of SA and H0 was also evaluated at a heating rate of 10 °C/min as a reference. The neat SA starts to decompose at 160 °C, whereas H08 and H12 do not show any trace of weight loss up to 320 °C. Thus, a successful substitution of SA to H0 can be concluded because no trace of residual SA is seen. Table 7 summarizes the temperatures obtained for mass losses at 5 mass % (T_5) and 50 mass % (T_{50}). Modification of –OH groups in H0 with SA significantly increases the thermal stability of H08 and H12.

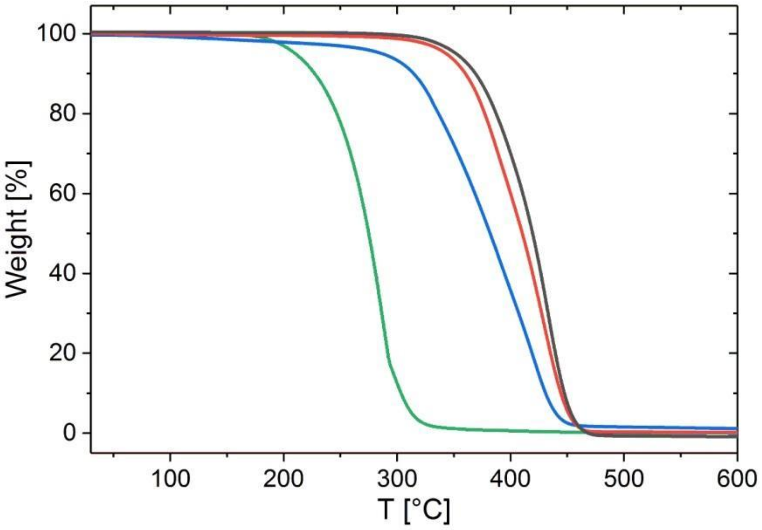

Figure 25: Thermogravimetric analysis of H12 (black), H08 (red), pristine H0 (blue) and SA (green).

Table 7: Degradation temperatures of SA, H0, H08 and H12 determined at a heating rate of 10 °C/min.

Sample	T_5 [°C]	T_{50} [°C]
SA	208	275
H0	290	382
H08	342	410
H12	350	420

The chemical structure of H08 and H12 was characterized via ^{1}H-NMR. For ^{1}H-NMR characterization, H08 and H12 was dissolved in $CDCl_3$. Figure 26 shows the ^{1}H-NMR spectrum of H08 along with the proton assignment, and Table 8 summarizes the corresponding integrals of signal intensities.

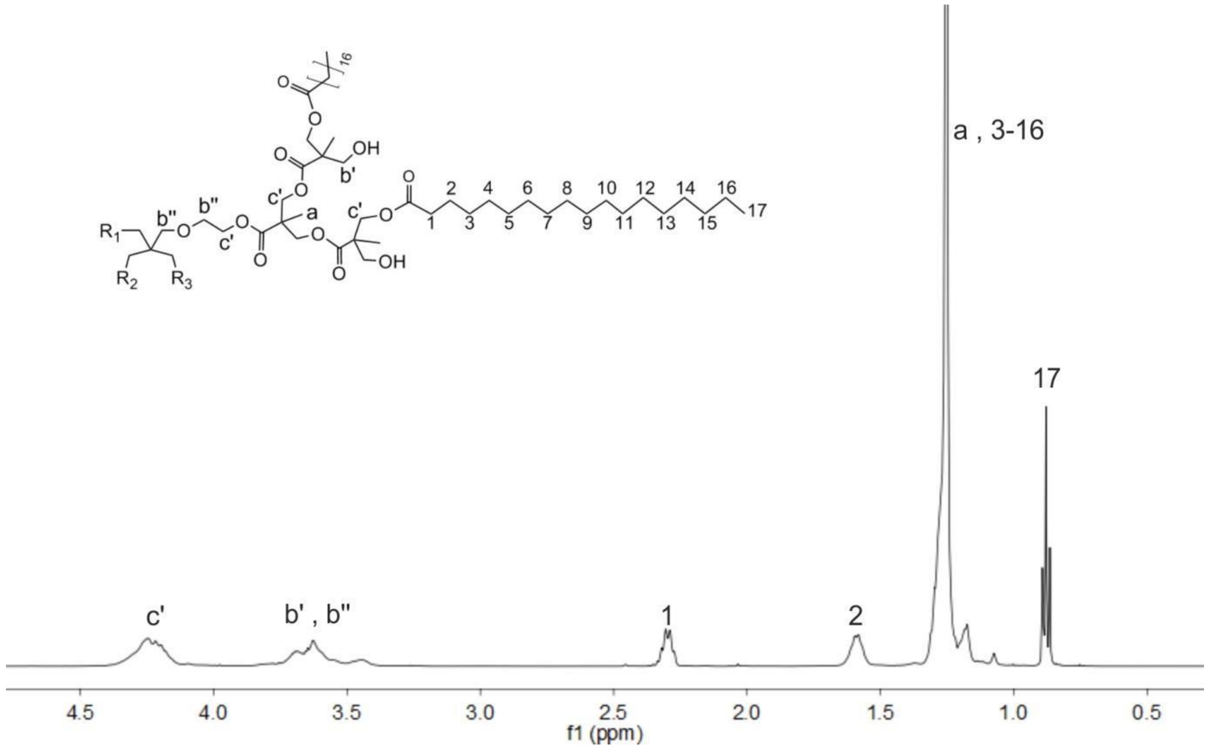

Figure 26: ^{1}H-NMR spectrum of H08 in $CDCl_3$.

Table 8: Summary of the integral intensity of signals from ^{1}H-NMR spectrum of H08 from Figure 26 and H12 (appendix). * represents reference signal.

Peak	Integral intensity for H08	Integral intensity for H12
*b (b' + b")	0.49	0.36
*c'	0.51	0.64
1	0.21	0.34
2	0.21	0.34

As discussed previously in section 4.2.2, the proton signals in the range 3.3 ppm - 4.2 ppm correspond to methylene protons of H0, whereas signals in the range 1 ppm - 1.4 ppm correspond to methyl protons of H0. H0 esterification with SA results in additional peaks of SA protons (labelled 3-16 in Figure 26) that overlap with methyl protons of H0. Furthermore, additional peaks at 2.28 ppm, 1.58 ppm and 0.88 ppm correspond to the remaining methylene and methyl protons of SA (labelled 1, 2 and 17 in Figure 26).

With reference to equations 8 and 9, the integral sum of *b* (*b'* and *b"*) and *c'* of an unmodified H0 is 1, where the integral sum of *b* is 0.7 and that of *c'* is 0.3. As shown in Figure 26, after the esterification of H0, methylene protons linked to hydroxyl group of H0 (*b'*) are transformed to methylene protons linked to ester groups of esterified H0. Thus, H0 esterification results in a decrease in the integral intensity of *b'* and a subsequent increase in the integral intensity of *c'*, whereas the integral sum of *b'*, *b"* and *c'* of esterified H0 and non-esterified H0 remains the same, i.e. 1 (reference signals, * in Table 8). For example, in case of H08 esterification, as presented in Table 8, the integral intensity of *b* reduced from 0.7 to 0.49 ($\Delta = 0.21$), whereas the integral intensity of *c'* increased from 0.3 to 0.51 ($\Delta = 0.21$). Thus, the amount of protons that shift from *b'* to *c'* corresponds to the intensity of signal 1 (methylene α to carboxyl group of SA), confirming an ideal case of H0 esterification without any side reactions. Similar observations were recorded in case of H12 esterification, as shown in Table 8. The ^{1}H-NMR spectrum of H12 is attached in the appendix section.

Based on the information from ^{1}H -NMR, the degree of stearyl chains substitution onto H0 (%DS) was calculated. The degree of stearyl chain substitution onto H0 reflects the ratio of –OH groups converted to ester groups and –OH groups initially present in pristine H0. Thus, % DS can be expressed as a peak integral ratio of methylene ester groups of SA (I_1) to the signal intensity of methylene α to the end hydroxyl groups in bulk H0 (equation 6). The latter was determined after the reaction of H0 with excess TAI (section 4.2.2).

$$\% \text{ DS} = I_1/0.44*100 \tag{10}$$

Based on equation 10, the calculated value of stearyl chain substitution onto H0 is 48 % for H08 and 77 % for H12. Thus, the expected theoretical amount of unreacted hydroxyl groups should be 52 % and 23 % for H08 and H12, respectively. The amount of unreacted hydroxyl groups after partial esterification with SA can be estimated using the TAI derivatization model, as discussed previously in section 4.2.2. The TAI substitution rate varies depending on the amount of free hydroxyl groups in modified H0, which is depicted schematically in Figure 27.

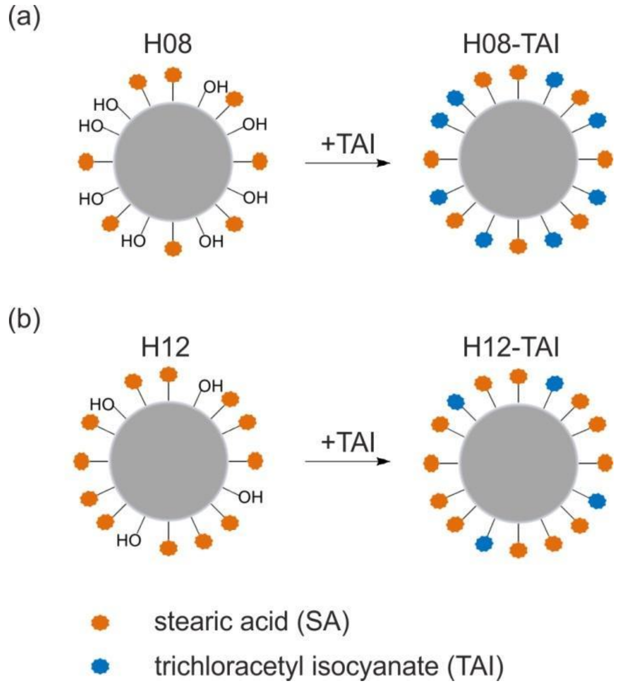

Figure 27: Schematic illustration of termination hydroxyl groups in (a) H08 and (b) H12 with TAI.

The intensity of the signals that appear after termination of hydroxyl groups with TAI change depending upon the extent of TAI substitution. Figure 28 shows an enlarged section of ^{1}H-NMR spectrum of neat and TAI-derivatized H08 and H12, supported by a schematic representation and signals attributed to the end groups. The peak designation and chemical shift are in agreement to the peaks presented in Figure 23 for TAI-derivatized H0. It can be observed that depending on the amount of free hydroxyl groups which varies between H08 and H12, the ratio of signal intensity *c”* to *c’* differs. As signal *e* is attributed to the imidic hydrogen of the derivatized end groups, the amount of unreacted hydroxyl end groups in H08 and H12 (%b’) can be calculated from its integral using equation 11.

$$\%b' = \frac{I_e}{0.44/2} * 100 \qquad (11)$$

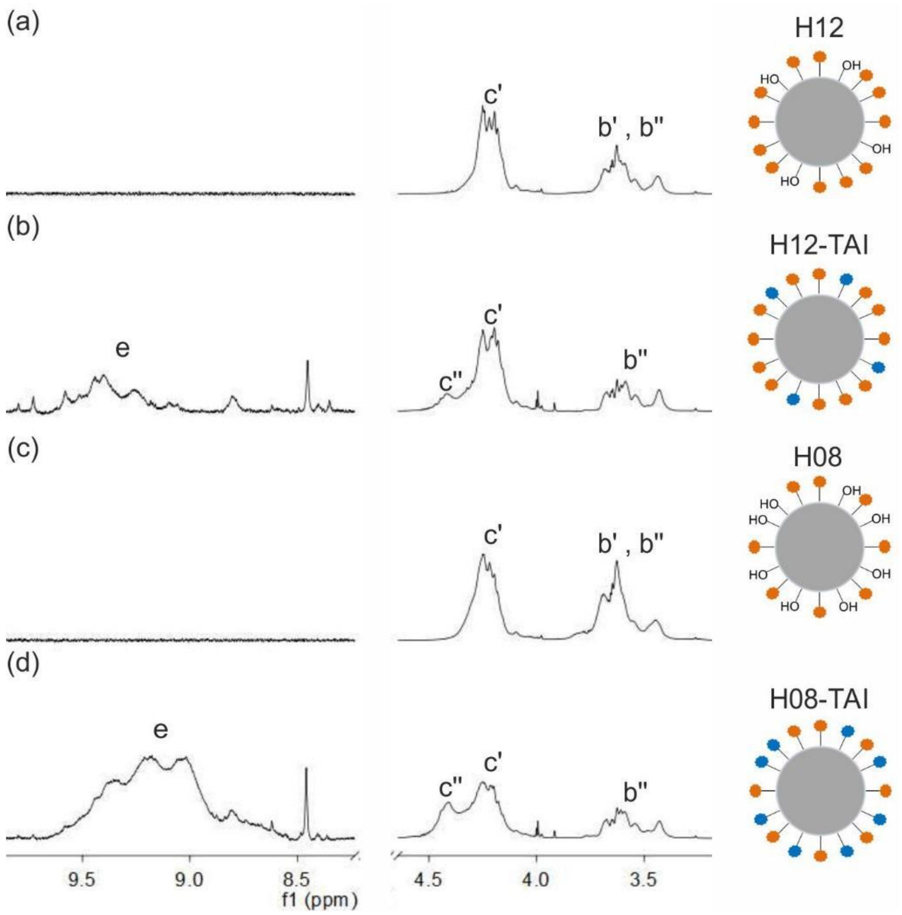

Figure 28: ^{1}H-NMR section of (a) H12, (b) TAI-derivatized H12, (c) H08 and (d) TAI-derivatized H08 showing signals attributed to the end groups, with magnified signal in the low magnetic field.

Table 9: Summary of the integral intensity of signals from the section of ^{1}H-NMR spectrum of TAI-derivatized H08 and TAI-derivatized H12 from Figure 28. * represents reference signal.

Peak	Integral intensity for H08	Integral intensity for H12
*b”	0.26	0.26
* c’ + c”	0.74	0.74
e	0.11	0.05

From equation 11, H08 and H12 have 50 % and 23 % of unreacted hydroxyl groups, respectively, which is in close agreement to the theoretical count of unreacted hydroxyl groups following the esterification with SA. This confirms that TAI derivatization is an effective method to establish the amount of hydroxyl end groups in hyperbranched polyester.

4.4. Synthesis of H0 Modified PLA

This section presents an approach to perform a reaction between H0 hydroxyl groups and PLA carboxyl groups in a continuous extrusion process using a small amount of Lewis acid catalyst, such as butyl stannoic acid (BuSnO(OH); BTA). An Organotin (IV) catalyst was selected due to its ability to boost the esterification at elevated temperatures [170,171]. PLA and H0 were blended at a molar ratio 5:1 and 1:1 in the presence of 0.2 phr BTA. The composition was calculated based on the molecular weight of PLA as determined by GPC (M_n= 1.31 * 10^5 g/mol) and the theoretical molecular weight of H0 (M_{theor}= 1748 g/mol). In addition, a sample of PLA was melt blended with H0 without BTA as a reference. The experiments were performed in a JSW TEX 30 twin-screw extruder operating in co-rotating mode (refer to the experimental section for further details). The residence time for a screw speed of 300 rpm and a throughput of 5 kg/h at 180 °C was 10 minutes. Table 10 summarizes the blend compositions with the respective codes, and Figure 29 illustrates the reaction between H0 and PLA in PLA matrix during the melt mixing.

Table 10: Composition of the extruded blends.

Code	PLA:H0 [molar ratio]	BTA [phr]
PLA	-	-
PLA/H0-5-1	5:1	-
PLA/H0/BTA-1-1	1:1	0.2
		2
PLA/H0/BTA-5-1	5:1	0.2

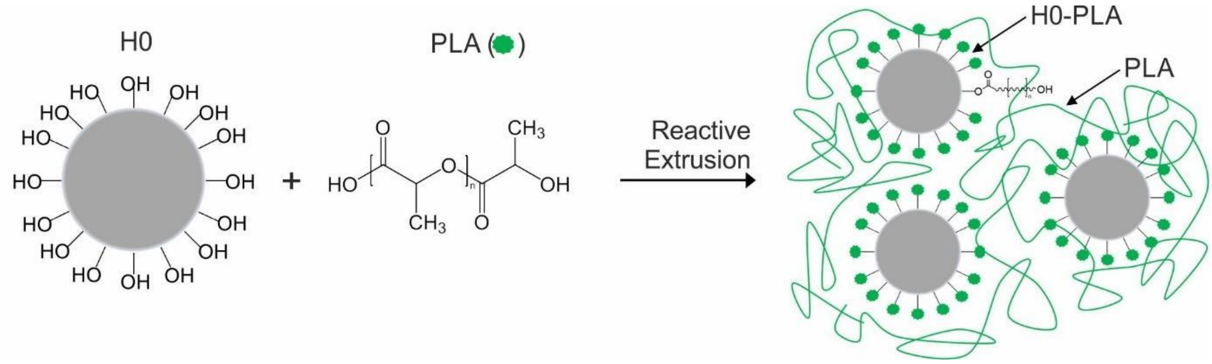

Figure 29: Schematic illustration of the reaction between H0 and PLA in PLA melt during reactive extrusion.

The reaction products of PLA and H0 during melt mixing were characterized using ^{1}H-NMR spectroscopy. For ^{1}H-NMR characterization, samples were prepared by dissolving the extruded material in $CDCl_3$. Figure 30 shows the ^{1}H-NMR spectrum of extruded PLA neat (Figure 30b), PLA/H0-5-1 (Figure 30c), PLA/H0/BTA-1-1 (Figure 30d) and PLA/H0/BTA-5-1 (Figure 30e). Figure 30a shows the spectrum of $CDCl_3$ so as to distinguish the solvent peak from the extruded material. The ^{1}H-NMR spectra of extruded materials have two characteristic signals at 1.5-1.6 ppm (*i*) and 5.13-5.20 ppm (*h*) corresponding to methyl and methine protons of the repeat units in PLA, respectively. The resonance signals at 1 ppm (*f*) correspond to the methyl group and those at 4.35 ppm (*g*) correspond to methine linked to the end hydroxyl groups. These signals have been previously reported in other studies [146,172]. In the enlarged section of the spectrum of PLA/H0-5-1, PLA/H0/BTA-1-1 and PLA/H0/BTA- 5-1 between 3.5 ppm and 4.5 ppm, new peaks can be seen, which are not present in neat PLA. As reported in sections 4.2.2 and 4.3, the position of these two peaks is in agreement with the chemical shift of methylene units in H0 (labeled b', b" and c'). The signal at ~4.28 ppm is overlapped by the signal for methine α to the end hydroxyl groups in PLA (g).

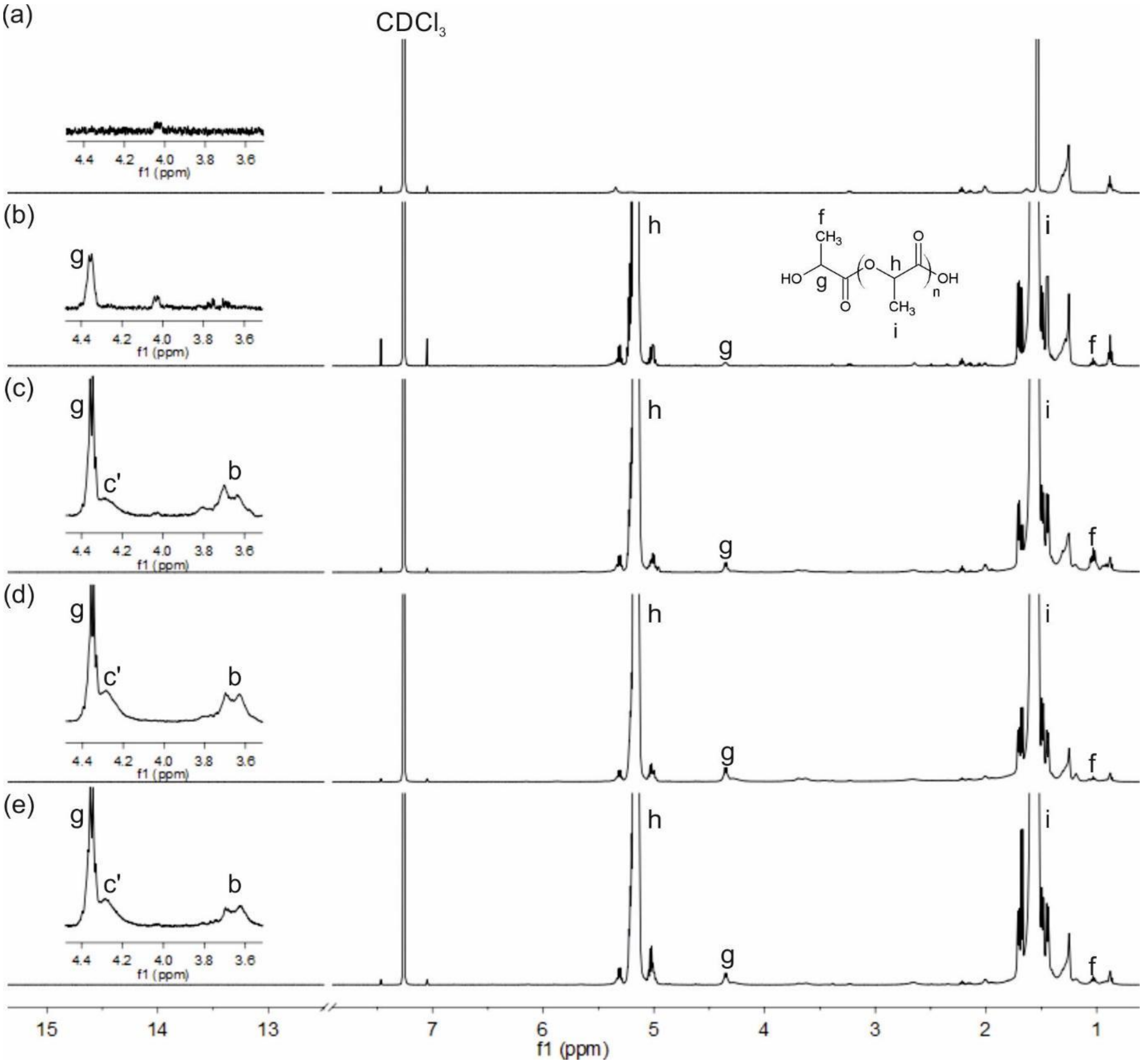

Figure 30: ^{1}H-NMR spectrum and assignment of peaks of (a) CDCl$_3$ NMR solvent (b) neat PLA (c) PLA/H0-5-1 (d) PLA/H0/BTA-1-1 and (e) PLA/H0/BTA-5-1 in CDCl$_3$.

To quantify PLA substitution on H0, the amount of unreacted hydroxyl groups by using a TAI derivatization model was determined. As discussed previously in sections 4.2.2 and 4.3, a TAI reaction with unoccupied –OH groups in H0 results in a peak labeled *c"* at 4.4 ppm, which corresponds to protons adjacent to TAI-terminated functional end groups in H0. Figure 31a is a schematic illustration of a partially successful reaction between PLA and H0, and Figure 31b is a schematic illustration of an unsuccessful reaction between PLA and H0. The green circles represent PLA-substituted H0, whereas the blue circles represent TAI-substituted H0. As shown in Figure 31a, the rate of TAI substitution onto H0 is low in case of partially successful PLA-H0 reaction due to limited availability of free –OH groups of H0. The consequence of the failed reaction between PLA and H0 is an increased rate of TAI substitution (Figure 31b).

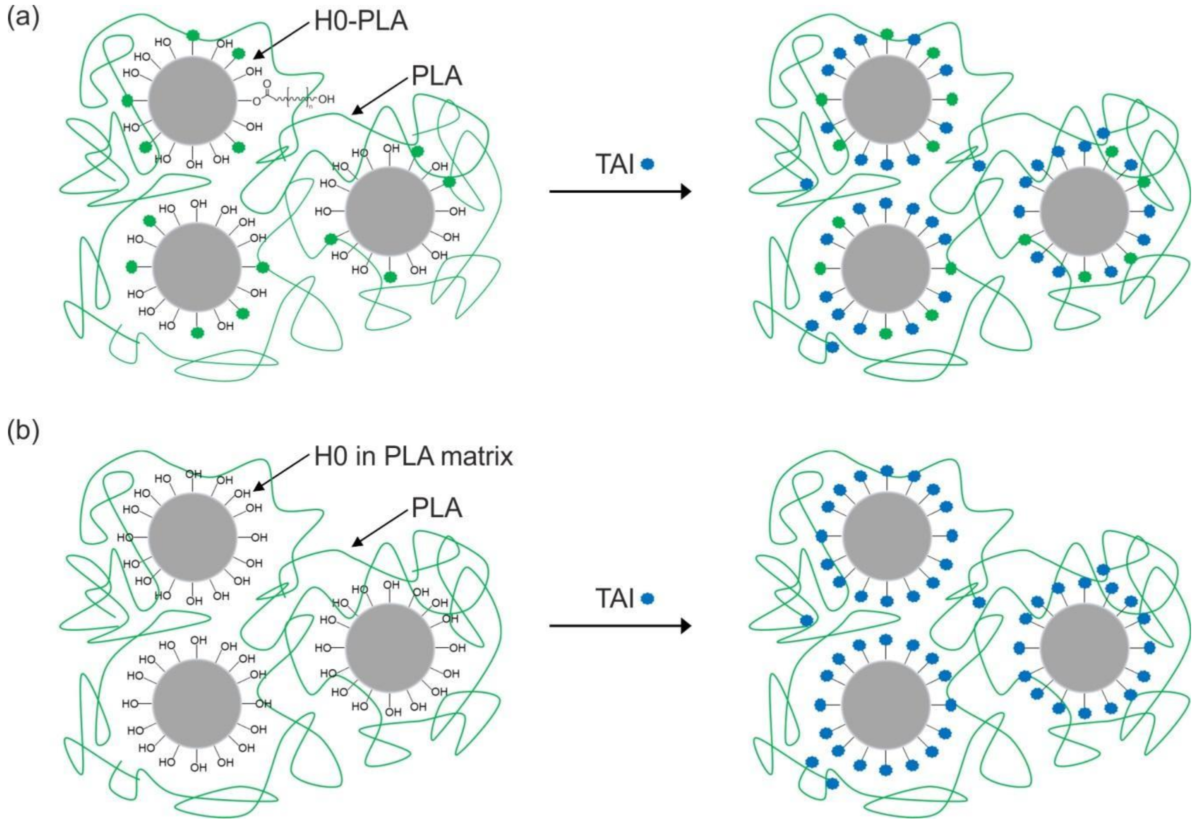

Figure 31: Schematic illustration of TAI derivatization in (a) partially successful reaction of H0-PLA and (b) unsuccessful reaction between H0 and PLA. The green circles represent PLA-substituted H0 and the blue circles represent TAI-substituted H0.

Figure 32 shows an enlarged section of ^{1}H-NMR spectrum of PLA (Figure 32a), PLA/H0-5-1 (Figure 32b), PLA/H0/BTA-1-1 (Figure 32c) and PLA/H0/BTA-5-1 (Figure 32d), and their respective TAI derivatives (Figure 32a'-d'). The peak (*g*) corresponding to a methine group linked to the end hydroxyl group of PLA (Figure 32a) disappears after substitution of TAI onto PLA (Figure 32a'). In the case of TAI-derivatized PLA/H0-5-1 (Figure 32b'), PLA/H0/BTA-1-1 (Figure 32c') and PLA/H0/BTA-5-1 (Figure 32d'), disappearance of *g* leaves *c'* uncovered. In addition, signal *c"* at 4.4 ppm is visible in TAI-derivatized samples and corresponds to the protons adjacent to TAI-terminated functional end groups in modified H0. As seen earlier in Figure 24b of TAI-terminated pristine H0 in section 4.2.2, the intensity of signal *c"* dominates the intensity of signal *c'*. The intensity ratio of signal *c"* to *c'* is 1.7 for PLA/H0-5-1. On addition of BTA as catalyst to the PLA/H0 system, the ratio of signal intensity *c"* to *c'* changes to 1.1 for PLA/H0/BTA-1-1 and and 0.8 for PLA/H0/BTA-5-1. A successful substitution of PLA onto H0 lowers the number of available free hydroxyl groups that can undergo termination with TAI, thereby lowering the ratio of signal intensity *c"* to *c'*. In other words, a distinctly lower signal intensity of *c"* in case of a PLA/H0 system catalyzed by BTA confirms a successful reaction between PLA and H0, unlike in the case of non-catalyzed PLA/H0 system. Thus, a partial modification of hyperbranched polyester with PLA can be confirmed for PLA/H0/BTA-1-1 and PLA/H0/BTA-5-1 systems in a melt mixing process, and a catalyst is required to support the esterification.

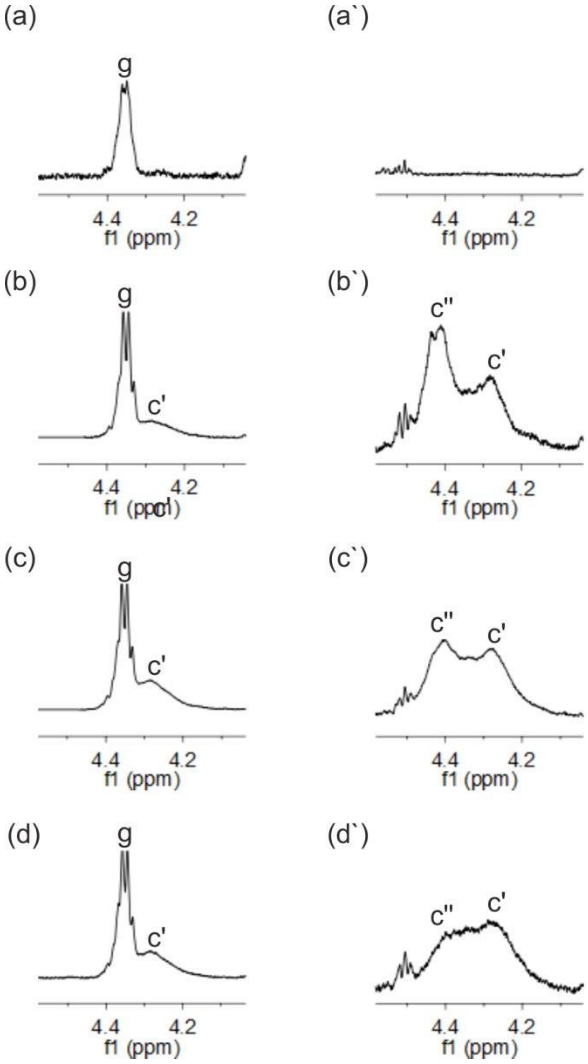

Figure 32: Portion of the ^{1}H-NMR of (a) PLA, (b) PLA/H0-5-1, (c) PLA/H0/BTA-1-1, (d) PLA/H0/BTA-5-1 and TAI derivative (a`) PLA, (b`) PLA/H0-5-1 (c`) PLA/H0/BTA-1-1, (d`) PLA/H0/BTA-5-1.

The thermal stability of PLA, PLA/H0-5-1, PLA/H0/BTA-1-1 and PLA/H0/BTA-5-1 was analyzed by thermogravimetric analysis. The samples were examined under nitrogen atmosphere at a heating rate of 10 °C/min. Figure 33 shows TG and DTG thermograms of various test specimens. Thermal decomposition of PLA/H0/BTA-1-1 and PLA/H0/BTA-5-1 samples occurs faster than in case of neat PLA and PLA/H0-5-1. The temperature of maximum decomposition rate obtained from DTG of PLA, PLA/H0-5-1, PLA/H0/BTA-1-1 and PLA/H0/BTA-5-1 is 371 °C, 369 °C, 277 °C and 275 °C, respectively. The reason for a sharp drop in the decomposition temperature of PLA/H0/BTA-1-1 and PLA/H0/BTA-5-1 could be related to the degradation due to the use of the catalyst in the melt mixing process. Besides the esterification activity, using tin as catalyst is known to cause back-biting reactions in PLA, leading to formation of lactide [173].

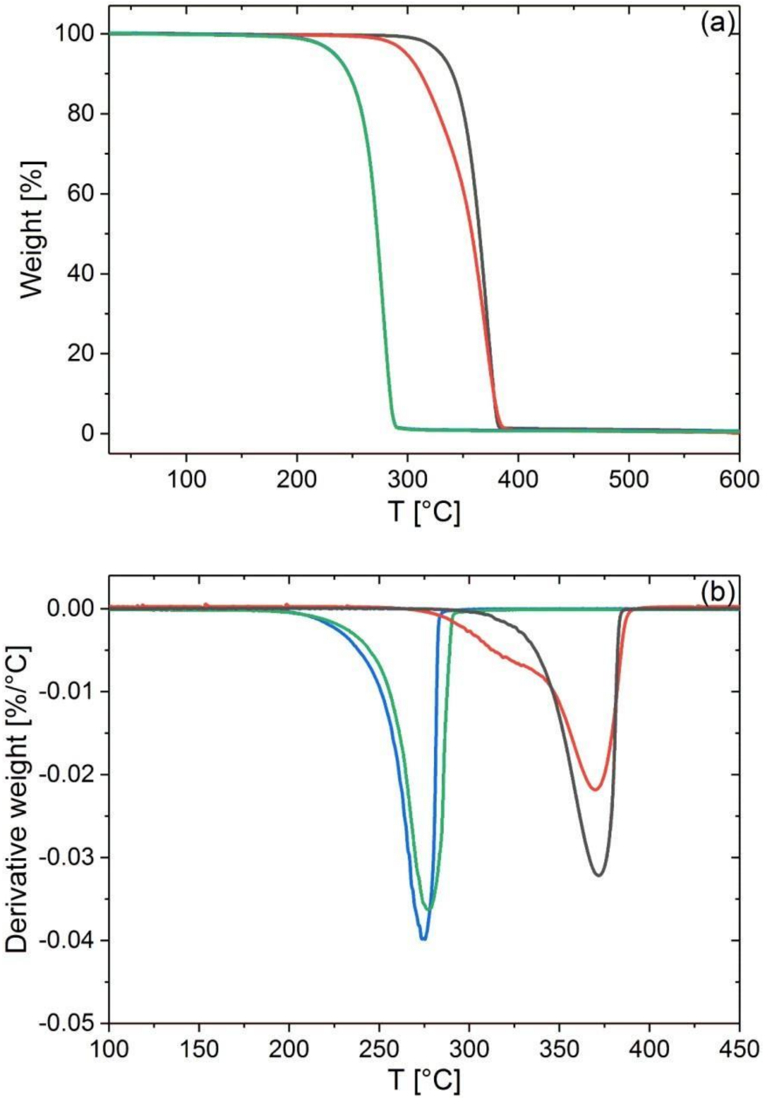

Figure 33: (a) TGA and (b) DTG curves of the thermal decomposition of PLA (black), PLA/H0-5-1 (red), PLA/H0/BTA-1-1 (green), PLA/H0/BTA-5-1 (blue).

In similar manner as previously mentioned, different amounts of BTA ranging from 0.2 % to 0.02 % were melt mixed with PLA in order to investigate the effect of the catalyst on the thermal properties of PLA. Figure 34 shows DTG thermograms of neat PLA and PLA containing different amounts of BTA.

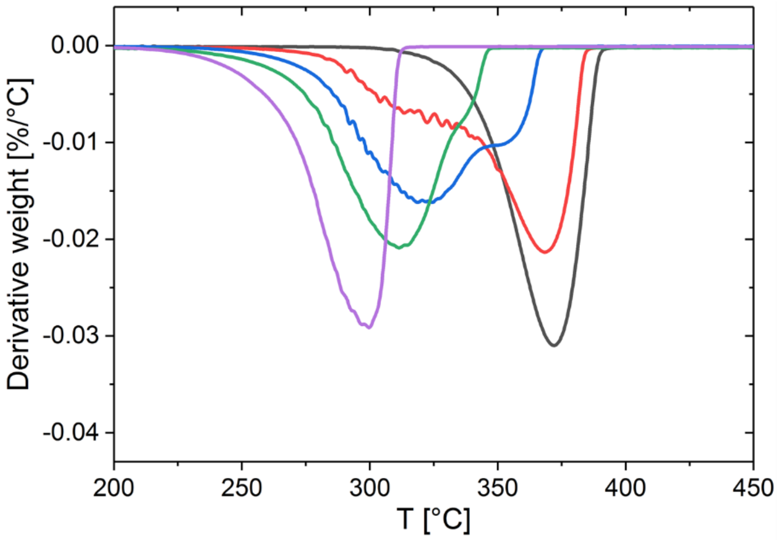

Sample	DTG_1 [°C]	DTG_2 [°C]
PLA	372	
PLA/0.02 BTA	368	325
PLA/0.05 BTA	322	358
PLA/0.075 BTA	311	340
PLA/0.2 BTA	298	

Figure 34: DTG curves of the thermal decomposition of PLA (black) and PLA containing 0.02 % (red), 0.05 % (blue), 0.075 % (green) and 0.2 % (purple) monobutyltin oxide.

As shown in the Figure 34, the maximum decomposition temperature of neat PLA is 372 °C (black curve). The addition of BTA to PLA causes a shift in the decomposition temperature and the extent of the temperature shift depends upon the amount of BTA content in PLA. As BTA content in PLA decreases from 0.2 % (purple curve) to 0.075 % (green curve), the maximum decomposition temperature shifts from lower temperature to higher temperature. In addition, a small shoulder peak in the range of 340 °C is observed, suggesting that the decomposition of PLA catalyzed with 0.075 % BTA occurs in two steps. The two-step decomposition is distinctly visible as the amount of BTA in PLA is reduced further to 0.05 % (blue curve). The maximum decomposition temperature shifts towards higher temperature, which means towards the maximum decomposition temperature of neat PLA. In the case of the PLA sample consisting of 0.02 % BTA (red curve), the maximum decomposition rate is 368 °C, which is almost as high as that for neat PLA (372 °C). The decomposition by 0.02 % BTA is 40 °C below the starting point of PLA decomposition, which is visible as a low temperature shoulder.

The two-step decomposition of PLA samples consisting of 0.02 %, 0.05 % and 0.075 % of BTA could be caused by tin-catalyzed PLA de-polymerization [25]. The literature suggests that PLA samples with substantial concentrations of tin catalysts decompose in two dominating pathways [174]. The low temperature decomposition occurs due to tin-catalyzed PLA de-polymerization that yields lactide, produced in a backbiting reaction. The high-temperature decomposition produces lactide, higher cyclic oligomers and nonselective decomposition products. It is likely that lactide and higher cyclic oligomers produced during the second step of decomposition are formed by radical cyclization or nucleophilic substitution reactions occurring randomly inside the polymer chain [174]. In the case of PLA consisting of 0.2 % BTA, a single decomposition step is observed, which could be due to the dominance of tin-catalyzed PLA de-polymerization initiated via free hydroxyl groups at the chain ends.

To understand the thermal degradation behavior of PLA and PLA catalyzed with BTA, ^{1}H-NMR analysis was examined on samples before and after extrusion, as shown in Figure 35. The samples for ^{1}H-NMR analysis were prepared in $CDCl_3$. The signal '*s*' in Figure 35 corresponds to the solvent. ^{1}H-NMR spectrum of neat PLA before and after extrusion does not show any evidence of change in the polymer structure, which might confirm that PLA does not undergo degradation during the extrusion process. However, in the case of PLA samples extruded with 0.2 % BTA (Figure 35c), new signals appear at 5 ppm (*k*) and 1.7 ppm (*j*), which could be related to the lactide unit formation, and confirms the material degradation during processing [172]. Signal '*k*' is related to methine proton in the ring and signal '*j*' to the methyl proton of the lactide unit. A drop in the catalyst amount in PLA to 0.02 % reduces the intensity of signal corresponding to lactide (Figure 35d), indicating that the tin-catalyzed PLA de-polymerization could be limited.

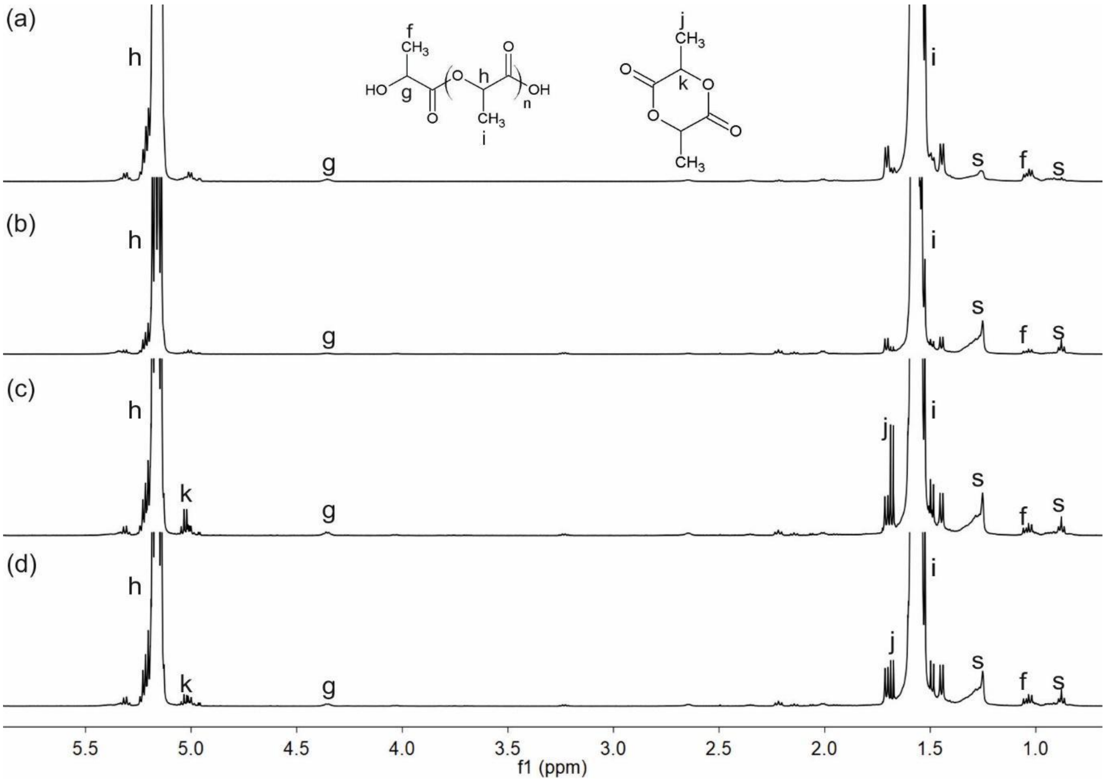

Figure 35: ^{1}H-NMR spectra and peak assignments of (a) PLA before extrusion (b) PLA after extrusion containing (c) 0.2 % BTA and (d) 0.02 % BTA. The spectrums were recorder in $CDCl_3$.

4.5. Synthesis of H08 and H12 modified PLA

The earlier section presented the possibility of modifying H0 with PLA in the presence of a catalyst such as BTA, in a reactive extrusion process. However, the amount of BTA is critical in terms of the degradation of PLA and an amount as high as 0.2 % could cause substantial degradation of PLA. The present section discusses melt extrusion of SA modified H0 and PLA in presence of BTA. First, a model experiment consisting of H08, PLA and 0.02 % BTA was conducted. H08 and PLA were mixed in molar ratio of 5:1 and 1:1. In addition, a model experiment consisting of H08 and PLA without BTA was conducted, which forms the reference. The model reactions were carried out in TGA equipment, and the reaction conditions, such as temperature and reaction time, were maintained identical to those in the reactive extrusion process. The aim of the model experiment was to evaluate if 0.02 % BTA is sufficient to catalyze the reaction between PLA and H08.

In order to facilitate dispersion of the reaction components, PLA, H08 and BTA were dissolved in dichloromethane. After evaporating dichloromethane, TAI termination of free hydroxyl groups was performed on each sample before and after the reaction in the melt. To perform the reaction in the melt, the samples were placed in a TGA pan and were heated up to 110°C for 2 hours to remove residual moisture. Finally, the samples were heated to 180°C. After 10 minutes, the samples were cooled rapidly to room temperature. As discussed in previous sections, TAI derivatization confirms the modification of hydroxyl groups of hyperbranched polyester polyol with PLA. Table 11 summarizes the composition of test samples.

Table 11: Sample composition with corresponding ^{1}H-NMR code as presented in Figure 36.

Sample code	PLA:H08 [molar ratio]	BTA [%]	Remark
PLA/H08-A	1:1	-	Prior reaction in melt
PLA/H08-A\`	1:1	-	After reaction in melt
PLA/H08-B	1:1	0.02	Prior reaction in melt
PLA/H08-B\`	1:1	0.02	After reaction in melt
PLA/H08-C	5:1	-	Prior reaction in melt
PLA/H08-C\`	5:1	-	After reaction in melt
PLA/H08-D	5:1	0.02	Prior reaction in melt
PLA/H08-D\`	5:1	0.02	After reaction in melt

The samples listed in Table 11 were characterized through ^{1}H-NMR spectroscopy. Figure 36 is an enlarged portion of the ^{1}H-NMR spectrum, showing signals attributed to protons adjacent to H08 end groups terminated with TAI.

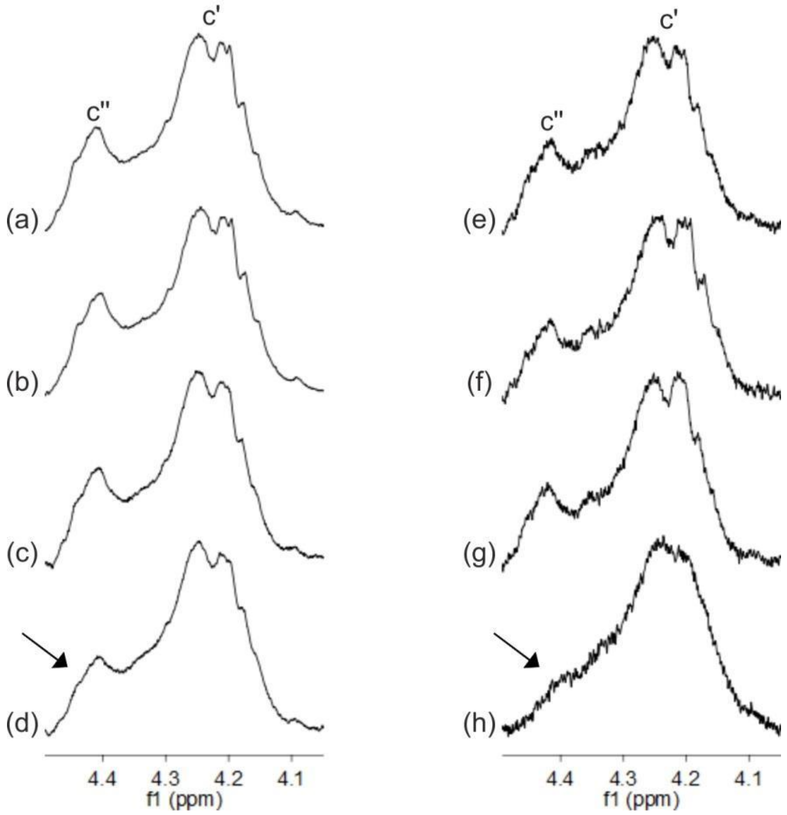

Figure 36: Expanded portion of the ^{1}H-NMR spectrum of TAI-terminated a) PLA/H08-A (b) PLA/H08-A\` (c) PLA/H08-B (d) PLA/H08-B\` (e) PLA/H08-C (f) PLA/H08-C\` (g) PLA/H08-D and (h) PLA/H08-D\`. The samples for ^{1}H-NMR spectroscopy were dissolved $CDCl_3$.

Figure 36a and Figure 36b show the enlarged portion of ^{1}H-NMR of TAI-terminated PLA/H08 samples mixed in molar ratio 1:1 without BTA, before and after a reaction in TGA, respectively. As shown in Figure 36a and Figure 36b, the ^{1}H-NMR overlap and no change in intensity of signal *c”* is observed. On addition of the catalyst to the reaction mixture, a slight change in intensity of signal *c”* between the samples before and after TGA process is observed, as shown in Figure 36c and 36d. Figure 36c and Figure 36d show enlarged portion of ^{1}H-NMR of TAI-terminated PLA/H08 samples mixed in molar ratio 1:1 containing 0.02 % BTA before and after a reaction in TGA, respectively. The change in intensity of signal *c”* could suggest that as less as 0.02 % BTA could support the reaction between free hydroxyl groups in H08 and PLA. As the molar ratio of PLA/H08 was increased to 5:1 without addition of BTA, similar behavior in ^{1}H-NMR of TAI-terminated PLA/H08 samples before and after a reaction in TGA was observed. As shown in Figure 36e and Figure 36f, there is no noticeable change in intensity of signal *c”* in ^{1}H-NMR spectrum. However, as shown by an arrow in Figure 36h, after addition of 0.02 % BTA to the reaction mixture, the signal intensity of signal *c”* almost disappears from the spectrum after the reaction in TGA. Figure 36g and Figure 36h show the enlarged portion of ^{1}H-NMR of TAI-terminated PLA/H08 samples mixed in molar ratio 5:1 containing 0.2 % BTA, before and after reaction in TGA, respectively. The disappearance of signal *c”* is a strong indication of a successful PLA functionalized H08. The reaction mixture of PLA/H08 with a molar composition 5:1 has a higher number of acid groups arising from PLA, and has a greater chance to functionalize hydroxyl groups of H08 with PLA, as compared to the reaction mixture of PLA/H08 with a molar composition 1:1.

Based on the observation made in the model reactions, PLA was melt blended with hyperbranched polyesters H08 and H12 in the presence of BTA in a JSW TEX twin-screw extruder. The sample PLA/H08/BTA-5-1 comprises of PLA/H08 having a molar composition 5:1 and 0.02 % BTA. The sample PLA/H12/BTA-5-1 comprises of PLA/H12 having a molar composition 5:1 and 0.02 % BTA. As explained earlier in section 4.3, H08 and H12 differ in the ratio of SA chains to free hydroxyl groups. In case of H08, the ratio of SA chains to free hydroxyl groups is approximately 1:1, whereas the ratio of SA chains to free hydroxyl groups in H12 is approximately 3:1. The extruded materials were derivatized with TAI, which is illustrated schematically in Figure 37.

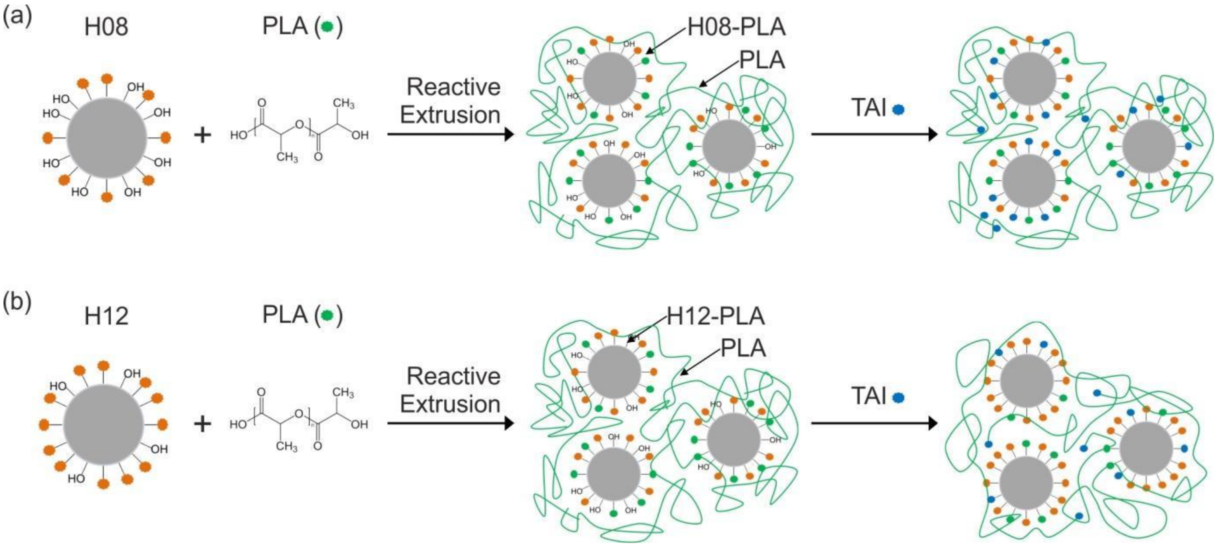

Figure 37: Schematic illustration of reaction between PLA and (a) H08, (b) H12 in PLA melt during reactive extrusion, followed by TAI derivatization of the extrudate.

The ^{1}H-NMR samples were prepared by dissolving the TAI derivatized extrudate in $CDCl_3$. ^{1}H-NMR spectrum of TAI-derivatized H08 and H12 forms the reference. The signals corresponding to protons adjacent to hydroxyl end groups terminated with TAI are marked as *c”* and these signals overlap with the signal *c’* of the methylene α to ester groups.

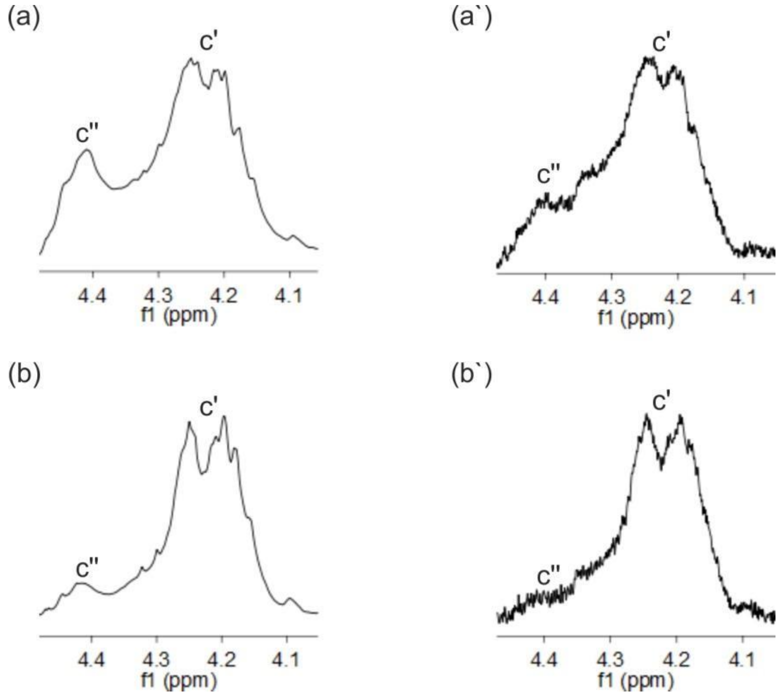

Figure 38: Enlarged portion of the 1H-NMR of TAI derivatized (a) H08 (a`) PLA/H08/BTA-5-1 (b) H12 and (b`) PLA/H12/BTA-5-1. The spectrums were recorded in $CDCl_3$.

The intensity of signal *c"* of TAI-derivatized H08 (Figure 38a) is significantly higher as compared to that of TAI derivatized PLA/H08/BTA-5-1 (Figure 38a'), which indicates the presence of a larger number of free hydroxyl groups in H08 as compared to PLA/H08/BTA-5-1. It can be inferred that functionalization of PLA onto H08 was effective in the presence of BTA. In case of TAI-derivatized H12 (Figure 38b), the signal intensity of *c"* is very weak and it yet again confirms the presence of a larger amount of free hydroxyl groups as compared to TAI-derivatized H08. The weak signal intensities make it difficult to draw a clear conclusion about the functionalization of PLA onto H12 in the presence of BTA (Figure 38b'). The intensity of signal *c"* in TAI derivatized H12 is much weaker than signal intensity of *c"* in TAI derivatized H08.

An attempt was made to investigate the utility of PLA/H08/BTA-5-1 and PLA/H12/BTA-5-1 as compatibilizers for PLA/PE binary blends. The ternary blends consisting of PLA/PE at a constant weight ratio of 80:20 wt% : wt% with PLA-modified H08 or PLA-modified H12 (5 or 10 wt%) were produced using a twin-screw extruder Process 11. The extrusion processes were characterized by pressure fluctuations and drop in melt pressure after addition of potential compatibilizer, from ~40 bar for binary blend to ~25 bar for ternary blend. The final material was highly deformed with visible melt instabilities and the resulting product was not suitable to be tested in a tensile testing equipment. Further investigation of processing parameters is required to obtain a homogeneous product.

4.6. Summary of hyperbranched polyester polyol modification with stearic acid and polylactic acid

A modification of a hyperbranched polymer into a star-shaped polymer comprising of stearic acid (SA) and poly lactic acid (PLA) arms was presented in this chapter. Boltorn™ HB20 (H0) is selected as the scaffold. An in-depth ^{1}H-NMR spectroscopy allowed quantification of the number of free -OH groups available for the H0 functionalization. A model study based on trichloracetylisocynate (TAI) was developed to quantify and verify the functionalization of H0 with stearic acid (SA) and PLA. ^{1}H-NMR spectroscopy analysis also helped to monitor the chemical changes occurring in H0 after TAI derivatization, SA and PLA substitution.

H0 was partially modified wit SA under melt conditions at two molar ratios; H0:SA / 1:8 (H8) and H0:SA / 1:12 (H12). The thermal stability of H08 and H12 increased with an increasing amount of end group modification. To study the conditions required for H08 and H12 functionalization with PLA, H0 was melt blended with PLA in a continuous extrusion process at different molar ratio of H0 and PLA along with 0.2 % butyl stannoic acid catalyst (BTA). The ^{1}H-NMR study of a TAI-derivatized extrudate revealed partial modification of hyperbranched polyesters with PLA in a catalyzed system, whereas there were no signs of reaction between PLA and H0 in a non-catalyzed system. A thermogravimetric analysis indicated that BTA causes material degradation during extrusion.

As low as 0.02 % BTA lowered the temperature of the maximum decomposition rate by 4°C as compared to neat PLA. The trigger temperature of decomposition was 40°C lower than that of neat PLA. The thermal stability of PLA was further affected by higher concentration of the catalyst.

Following the H0 and PLA reaction in presence of BTA, another reference study was conducted in order to evaluate PLA substitution onto H08 in presence of 0.02 % BTA. PLA and H08 were mixed in a molar ratio 1:1 and 5:1 and the reaction was performed in TGA under conditions that closely mimicked the conditions in an extrusion process. The samples were subjected to TAI derivatization before and after the reaction, and the samples were analyzed via ^{1}H-NMR spectroscopy. The TAI derivatization confirmed that as low as 0.02 % BTA supports the reaction between free hydroxyl groups in H08 and PLA. There was no sign of reaction between PLA and H08 in the absence of a catalyst. Finally, a reactive extrusion comprising of PLA:H08 / 5:1 and PLA:H12 / 5:1, in presence of 0.02 % BTA, was conducted. The resulting samples subjected to TAI derivatization and ^{1}H-NMR spectroscopy analysis confirmed a successful partial substitution of PLA onto H08. Owing to a low number of free hydroxyl groups and the resulting weak signal intensities in ^{1}H-NMR spectrum of H12 and PLA/H12/BTA-5-1 it was difficult to conclude a successful partial substitution of PLA onto H12.

5. Compatibilization of PLA and PE blends with epoxy functionalized PE. Degradation study on binary and ternary blends

5.1. General remarks

This chapter is divided into two subparts. The first part of this chapter presents compatibilization studies on PLA/PE blends using ethylene-glycidyl methacrylate (E-GMA) as the compatibilizer. The mechanical properties of the resulting PLA/PE/E-GMA ternary blends are investigated and compared against PLA/PE binary blends. The influence of E-GMA on the deformation behavior of the dispersed phase during uniaxial elongation is examined in detail.

In the second part of this chapter, the impact of PE and E-GMA on the natural weathering behavior of PLA is investigated. The sample preparation and the field set-up are explained. The methodology uses the variation in the thermal stability of the samples, changes in the chemical structure, and the molecular weight due to natural weathering to study sample degradation. The present research is the first of its kind to study the response of PLA/PE blends to natural outdoor conditions and environmental UV radiation.

5.2. Tensile testing and morphology investigation of PLA/PE/E-GMA ternary blends

The ternary blends were prepared at a constant weight ratio of PLA/PE/E-GMA / 80:20:5 / wt%: wt%: wt% using a twin-screw extruder Process 11, equipped with a slit die and conveyor belt at the die exit. The extruded material was drawn continuously at a draw ratio of 2. The dispersed phase of ternary blends comprises the PE types HDPE, LDPE, LLDPE and mPE. The elasticity modulus and elongation at break of the resulting blends were characterized in a tensile testing machine. The sample specimens for tensile testing were punched directly out of the extruded film. The tensile test data of E-GMA compatibilized PLA/PE ternary blends are summarized in Table 12. For comparison purposes, the tensile test data of neat PLA and PLA/PE binary blends from chapter 3 (section 3.1) are also included in the Table 12.

Table 12: Comparison of tensile properties of PLA, PLA/PE binary blends and E-GMA compatibilized PLA/PE ternary blends.

Sample	Composition	Elasticity Modulus (MPa)	Elongation at break (%)
PLA	100	1810 ± 188	8.6 ± 1.9
PLA/HDPE	80/20	1590 ± 95	11 ± 8
PLA/HDPE/E-GMA	80/20/5	1580 ± 70	384.0 ± 16
PLA/LDPE	80/20	1330 ± 29	5 ± 0.8
PLA/LDPE/E-GMA	80/20/5	1330 ± 50	342 ± 24
PLA/LLDPE	80/20	1400 ± 69	355 ± 34
PLA/LLDPE/E-GMA	80/20/5	1310 ± 85	396 ± 28
PLA/mPE	80/20	1390 ± 78	364 ± 30
PLA/mPE/E-GMA	80/20/5	1270 ± 25	419 ± 35

As previously discussed in chapter 3, the elongation at break of PLA/mPE and PLA/LLDPE is noticeably higher than neat PLA, PLA/HDPE and PLA/LDPE blends. Addition of E-GMA to the PLA/LLDPE and the PLA/mPE blends provides a negligible boost to the elongation at break as shown in Table 12. On the other hand, an addition of 5 % E-GMA to the PLA/HDPE and the PLA/LDPE blends has an enormous impact on the elongation at break as compared to that in the PLA/HDPE and the PLA/LDPE binary blends. Approximately an increase by 300 % in elongation at break of the PLA, the PLA/HDPE and the PLA/LDPE blends is obtained on addition of 5 % E-GMA to the blend composition. However, addition of E-GMA has a negligible impact on the elasticity modulus of the PLA/HDPE and the PLA/LDPE binary blends. Importantly, the presence of E-GMA does not deteriorate the elasticity modulus of the PLA/HDPE and the PLA/LDPE binary blends.

The morphology of PLA/PE/E-GMA ternary blends listed in Table 12 was investigated. A comparison of morphologies of PLA/PE binary and PLA/PE/E-GMA ternary blends is presented in Figure 39.

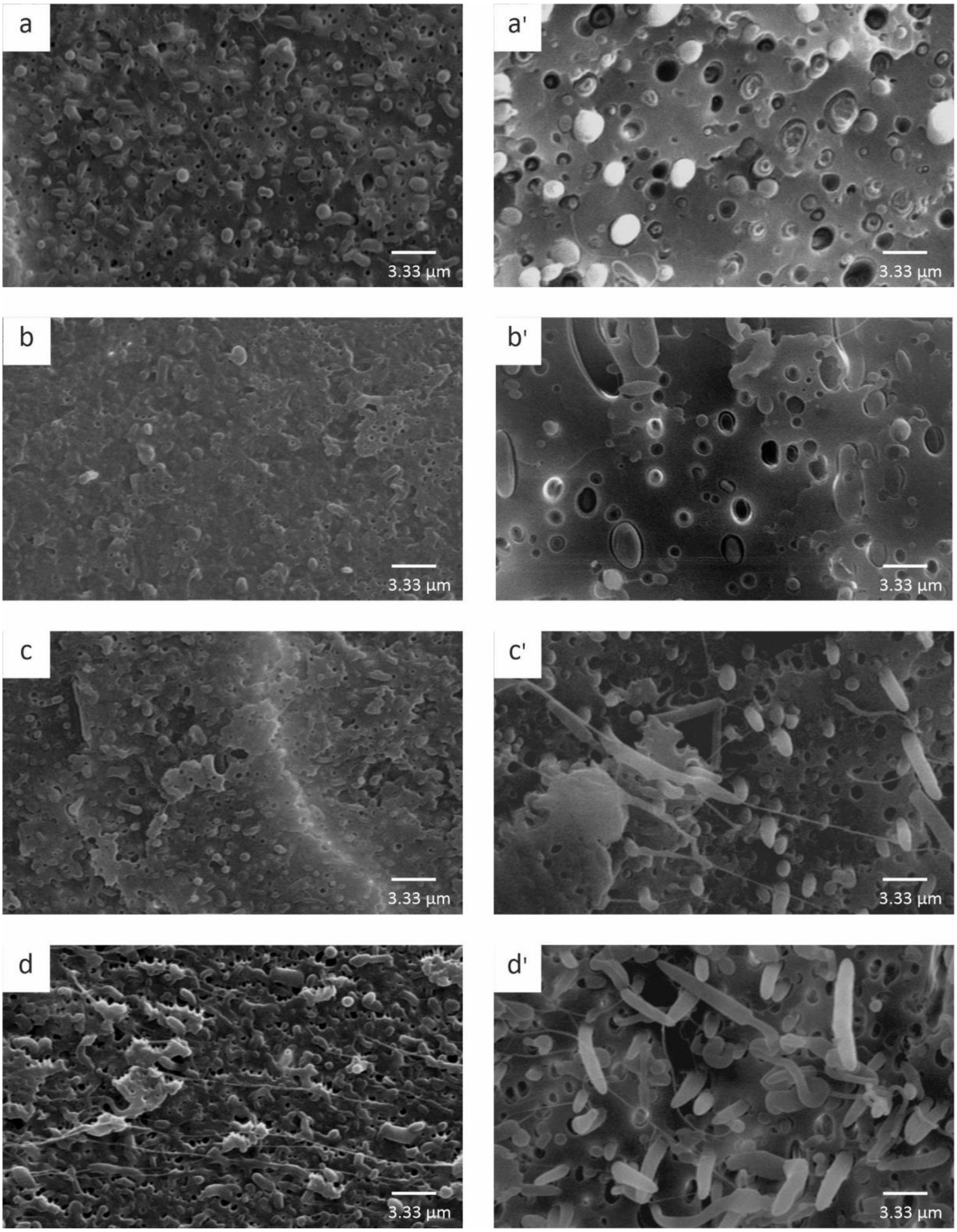

Figure 39: SEM morphologies of the cryogenically-fractured surface of compatibilized blends (a) PLA/HDPE/E-GMA, (b) PLA/LDPE/E-GMA, (c) PLA/LLDPE/E-GMA, (d) PLA/mPE/E-GMA and binary blends (a’) PLA/HDPE, (b’) PLA/LDPE, (c’) PLA/LLDPE and (d’) PLA/mPE.

Figure 39 indicates that addition of E-GMA to PLA/PE blend leads to a finer morphology of dispersed phase with very few cavities being visible on the fractured surface, in contrast to morphology of uncompatibilized blends. In particular, PLA/HDPE/E-GMA (Figure 39a) and

PLA/LDPE/E-GMA (Figure 39b) have a noticeably different morphology, where the size of the PE globules is much lesser as compared to that observed in the PLA/HDPE (Figure 39a') and the PLA/LDPE (Figure 39b') binary blends. The addition of an interfacial modifier like E-GMA results in a decrease in interfacial tension, which significantly decreases the particle size that is difficult to be deformed. The improvement of interfacial adhesion between the matrix and the dispersed phases could result in better stress transfer and subsequent improvement in elongation at break. Addition of a compatibilizer to PLA/LLDPE and PLA/mPE inhibits the coalescence of the dispersed phase. As discussed earlier in the chapter 3, coalescence might contribute to the development of elongated dispersed phase particles in binary blends. The merger of the droplets is prevented as the dispersed phase is coated with the compatibilizer [175]. Therefore, morphology of the PLA/LLDPE/E-GMA (Figure 39c) and the PLA/mPE/E-GMA blends (Figure 39d) is transformed into fine spherical particles dispersed in the matrix.

In order to confirm interfacial adhesion between the matrix and the dispersed phases, DSC analysis on pure PLA and PE-free PLA/E-GMA blends were performed. The amount of E-GMA in the PE-free PLA/E-GMA blend composition was varied. Figure 40 shows the DSC second heating thermograms of PLA (curve a) and different PLA/E-GMA blends (curve b to e) recorded at heating rate of 10 °C/min. The amount of E-GMA in the blend composition was increased from 5 wt% (curve b) to 20 wt% (curve e) in steps of 5 wt%.

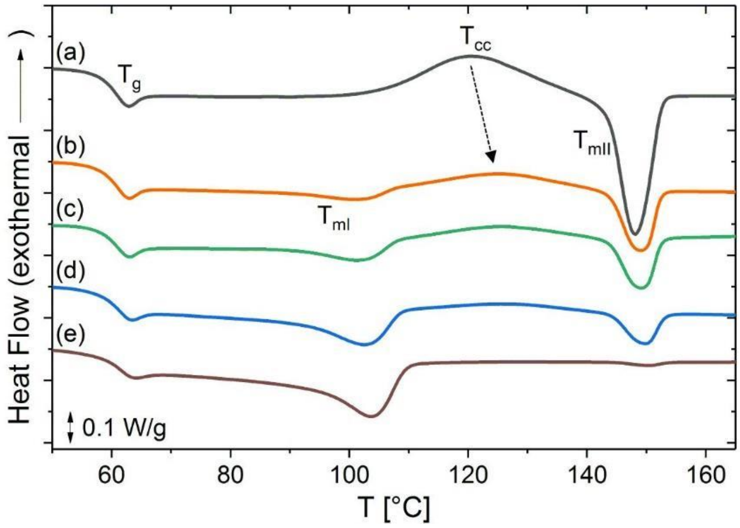

Figure 40: DSC heating curves of (a) PLA and PLA/E-GMA blends in different ratios of E-GMA (b) 95/5, (c) 90/10, (d) 85/15, (e) 80/20 recorded at the heating rate of 10 °C/min.

Figure 40 shows that addition of 5 wt% of E-GMA into PLA (curve b) results in a drop in enthalpy of cold crystallization and melting point enthalpy of PLA, whereas cold crystallization (T_{cc}) of PLA shifts to a higher temperature. A further increase in the amount of E-GMA in the blend composition causes a minor increase in the cold crystallization temperature of PLA, and a decrease in the melting point enthalpy of PLA. The melting point enthalpy of PLA is barely visible as the amount of E-GMA in the blend composition reaches 20 wt% (curve e). This diminishing of the melting enthalpy of PLA could be attributed to a chemical reaction between end carboxyl groups of PLA and epoxy groups of E-GMA, which also reduces the mobility of PLA chains and their ability to crystallize [176,177]. The DSC data of the PLA and the PLA/E-GMA blends are summarized in Table 13.

Table 13: Thermal parameters obtained from DSC heating scan of PLA and PLA/E-GMA blends recorded at a rate of 10 °C/min.

Sample	Composition (wt% / wt%)	T_g [°C]	T_{mI} [°C]	ΔH_{mI} [J/g]	T_{cc} [°C]	ΔH_{cc} [J/g]	T_{mII} [°C]	ΔH_{mII} [J/g]
PLA	100	58	-	-	121	15	148	15
PLA/E-GMA	95/5	58	102	3	125	7	149	7
PLA/E-GMA	90/10	58	102	4	126	5	149	5
PLA/E-GMA	85/15	58	103	7	127	3	150	3
PLA/E-GMA	80/20	59	104	10	-	-	150	0.2

5.3. Field setup

In this section, the impact of mPE and E-GMA on the weathering properties of PLA under natural environmental conditions is investigated. Blends of PLA/mPE with the weight ratio 80:20 and those of PLA/mPE/EGMA with the weight ratio 80:20:5 were prepared, and PLA was selected as a reference sample. The PLA, PLA/mPE binary and PLA/mPE/EGMA ternary blends were extruded through a film blowing extruder equipment. The pellet composition was added to a 25 L/D AxonBX25 extruder fitted with a blowing die of 70 mm diameter and an associated tower. The samples were melt mixed into a film of thickness 0.02-0.03 mm.

The samples were tested over five months from January to May 2017 (Australian summer-autumn period) at Pinjarra Hills, Queensland Australia. The field study was carried out during favorable meteorological conditions, where the atmospheric temperatures and humidity were high. At the trial site, the temperature, humidity and rainfall were recorded with the support of a weather station (Campbell Scientific Inc.). However, the soil conditions were not recorded. Figure 41 shows monthly average temperature and humidity data recorded by the weather station over the period of the field test. The total rainfall accumulation was 3 mm from January to end of February, 305 mm in March, 16 mm in April and 46 mm in May.

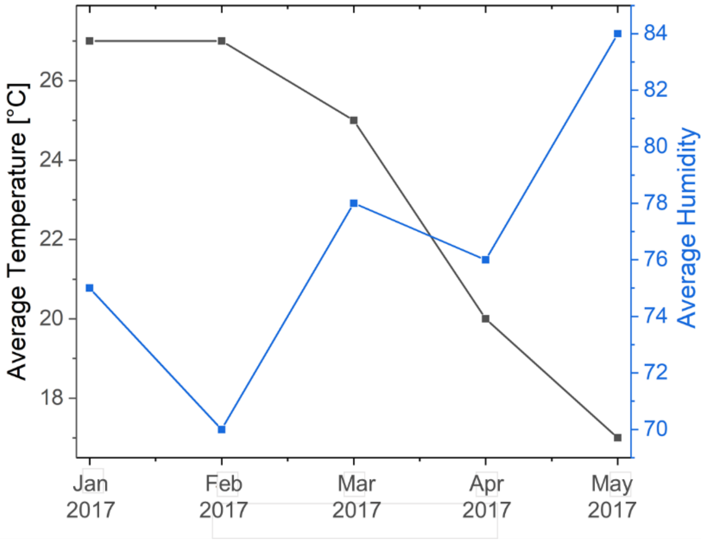

Figure 41: Monthly average temperature and humidity data recorded from January to May 2017 recorded by the weather station.

The samples were partially submerged in soil, as it is known that various environmental factors could affect degradation of the sample place either under or above the ground. Sunlight is the major source of UV radiation and temperature, whereas rain and atmospheric humidity are the source of moisture [178]. It is known that the chain scission in the PLA backbone and reduction in the molecular weight could occur as a consequence of UV irradiation, hydrolysis and/or microbial attack [178–180]. Figure 42a is a picture taken from the field, where PLA, PLA/mPE and PLA/mPE/E-GMA samples were partially submerged in soil. Figure 42b and 42c are schematic representations that show part of the film submerged in soil (UG) and part of the sample lieing above the soil (AG) from top view and cross-section, respectively.

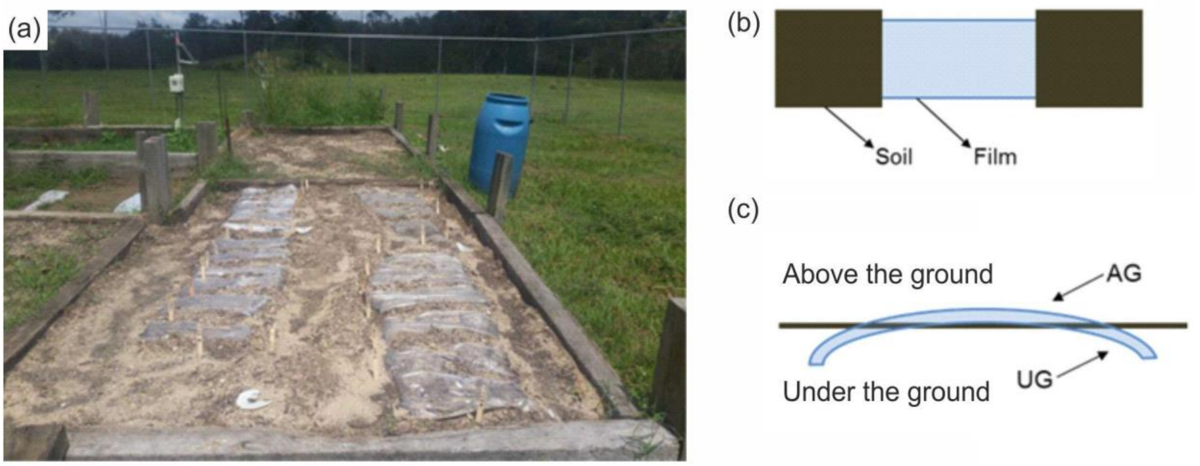

Figure 42: (a) PLA, PLA/mPE and PLA/E-GMA samples placed at the field in the outskirts of Brisbane, (b) schematic representation of sample placed at the field partially submerged in the soil from top and (c) cross-section.

5.4. Weathering behavior of PLA and PLA blends

The variation in thermal behavior of samples before and after weathering was used as a method to study sample degradation. Thermal gravimetric analysis (TGA) determines the thermal stability of the samples and it can be correlated to the material degradation, as the low molecular weight fraction derived from the degradation of the long chain polymer can volatilize easily [181]. Thermogravimetric analysis was performed on film specimens that were placed above the soil and under the soil. The film specimens were cleaned prior to the TGA analysis. Figure 43 shows temperatures obtained for all the samples at a mass loss of 10 % (T_{10}) and 50 % (T_{50}).

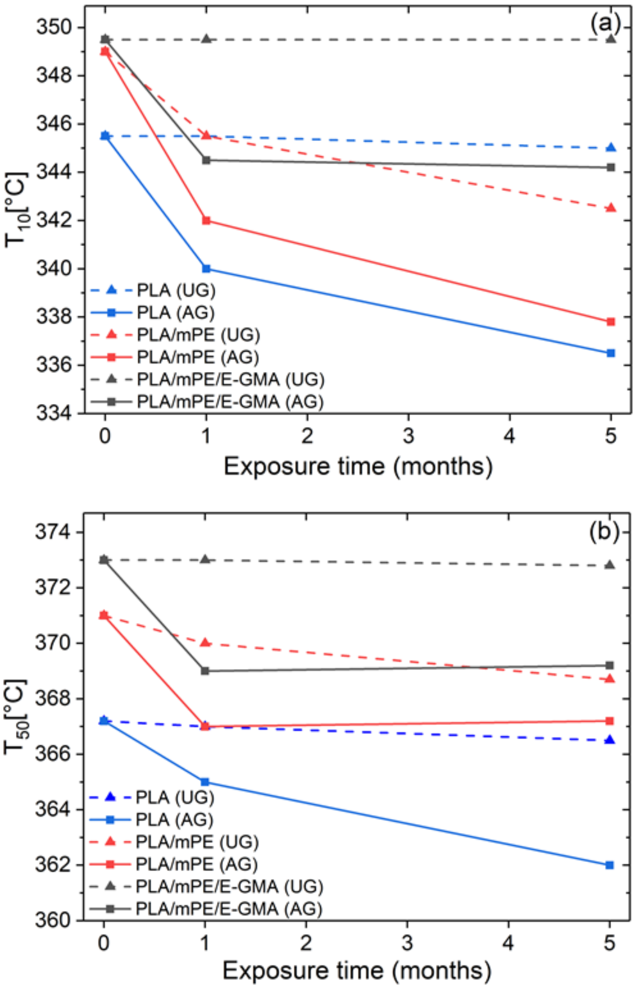

Figure 43: Effect of the exposure time on the thermal degradation temperature obtained at (a) 10 % mass loss and (b) 50 % mass loss for the sample specimen placed above the ground (AG solid line) and under the ground (UG dashed line).

At exposure time 0, an increase in thermal stability of PLA/mPE binary and PLA/mPE/EGMA ternary blends as compared to neat PLA is observed. The increase in initial degradation temperature of PLA/mPE and PLA/mPE/E-GMA could be related to polyethylene particles retarding the diffusion of oxygen into the polymer matrix [91]. Thus, the thermal oxidation of

PLA in either PLA/mPE or PLA/mPE/E-GMA blend is inhibited, resulting in enhancement of the thermal stability of the blend. A significant difference can be observed in thermal degradation temperatures of the sample specimen above the ground (solid line) and sample specimen under the ground (dashed line), which follows a similar pattern at a mass loss of 10 % and 50 %.

A decrease in the thermal stability of the PLA (blue solid line), the PLA/mPE (red solid line) and the PLA/mPE/E-GMA (black solid line) films placed above the ground is seen after just one month of exposure. The thermal stability of the PLA and PLA/mPE samples continues to decrease until the end of 5 months of exposure, whereas the addition of E-GMA inhibits the degradation process of PLA/mPE/E-GMA. The higher thermal stability of PLA/mPE/E-GMA compared to that of PLA/mPE could be a result of the stabilizing effect that E-GMA imparts at the blend interface. The morphology evaluation of the blown film was not feasible due to very low thickness of the film. However, as discussed in the sections 3.2 and 5.2, the morphology of PLA/mPE is characterized by micro voids at the interfacial region of the PLA and the mPE phases, whereas PLA/mPE/E-GMA morphology is more homogenous. The large amounts of micro voids might create space for water to penetrate into PLA/mPE, which could result in PLA hydrolysis and reduced thermal stability of the binary blend [182].

In case of films buried under the soil, no changes are observed in thermal behavior of PLA (Figure 43, blue dashed line) and PLA/mPE/EGMA (Figure 43, black dashed line) over the entire 5 months of exposure, thus providing no signs of degradation. However, just after one month of exposure, the thermal stability of the PLA/mPE sample buried under the soil (Figure 43, red dashed line) drops, which could be correlated to the presence of micro voids that promote water intake and subsequent PLA hydrolysis as explained earlier. Thus, the degradation rate of all sample specimens above the soil is faster, where the specimen has maximum exposure to UV radiation, compared to sample specimens underneath the soil.

FT-IR analysis of PLA (Figure 44a), PLA/mPE (Figure 44b) and PLA/mPE/EGMA (Figure 44c) was performed in order to reveal the changes in the chemical bonds of samples after weathering. In these figures, the sample specimen before exposure to natural weathering is denoted as sample I (black line), the sample specimen after five months of exposure to natural weathering underneath the soil is denoted as sample II (green line), and the sample specimen after five months of exposure to natural weathering and placed above the soil is denoted as sample III (red line).

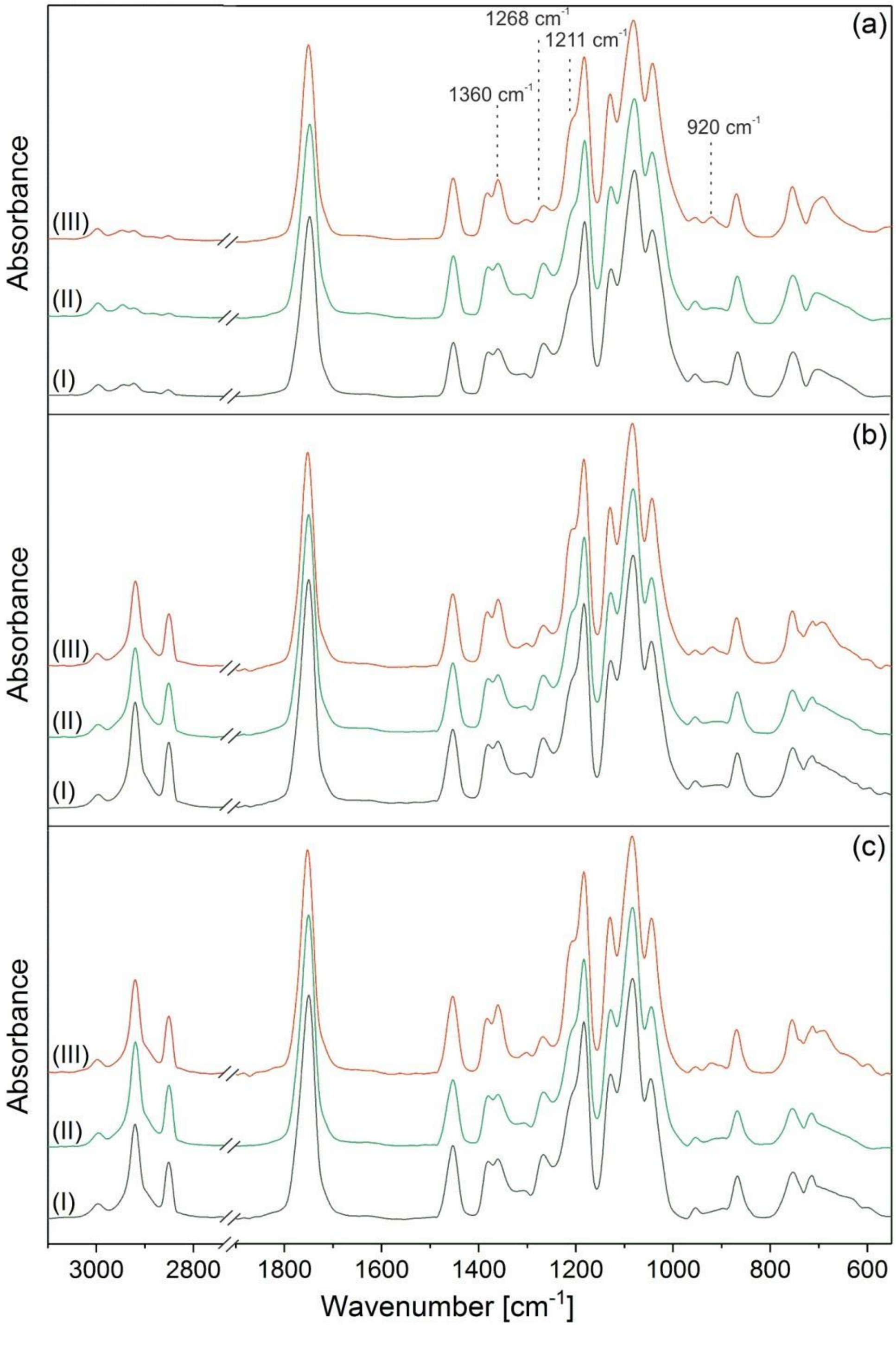

Figure 44: FT-IR spectrum of (a) PLA, (b) PLA/mPE and (c) PLA/mPE/EGMA. (I) Sample specimen before weathering, (II) sample specimen underneath the soil after 5 months and (III) sample specimen above the soil and exposure to the sun after 5 months.

As shown in Figure 44a, the characteristic bands in FT-IR spectrum of PLA before weathering (sample I) are in accordance with the FT-IR bands of PLA reported in the literature [180,183]. The individual FT-IR bands of PLA are summarized in Table 14.

Table 14: Characteristic bands in FT-IR spectrum of PLA.

Position [cm^{-1}]	Assignments
868	C-C stretching
1266, 1182, 1128,1080,1043	C-O stretching
1360, 1380, 1452	C-H deformation
1748,	C=O ester carbonyl groups
2996, 2923, 2852	C-H stretching

As shown in Figure 44a, the PLA sample specimen under the soil (sample II) and the PLA sample above the soil (sample III) do not show a shift to a higher or a lower signal intensity. However, the PLA sample III shows the presence of a new band at 920 cm^{-1}. With respect to PLA degradation, the band at 920 cm^{-1} can be ascribed to either vinyl unsaturated groups or the presence of alpha crystals [184–187]. It is reported that PLA photo-degradation might result into chain scission of ester backbone by the formation of C=C double bonds and carboxylic acids [184]. Another study reveals that the band at 920 cm^{-1} could represent a PLA crystalline structure, which appears as a consequence of the erosion of the amorphous parts due to hydrolysis [187]. Additionally, it is observed that the band at 1268 cm^{-1}, which corresponds to carbonyl ester groups, is less intense in the PLA sample III compared to PLA sample I and PLA sample II. The decrease in C-O stretching peak could be correlated to either photodegradation or hydrolysis of PLA, and either of these leads to chain scission of C-O bonds of the PLA ester backbone [178]. Consequently, it is observed that the amount of ester links is reduced, and the amount of carboxylic group is enhanced simultaneously, which reflects in a more intense band at 1211 cm^{-1} corresponding to –OC-O stretching of the carboxylic group [188]. In addition, the vibration of –CH group at 1360 cm^{-1} is sharper for the PLA sample III due to the different arrangement of chain conformations [188]. The observations and analysis so far suggest that photodegradation and hydrolysis are the possible route of PLA degradation. Structural differences between sample I and sample II are not observed. Thus, based on thermogravimetric and FT-IR analysis, it can be confirmed that PLA degradation under the soil was not present or was negligible. Slow rate of PLA degradation under the soil could be due to slow rate of hydrolysis at low temperatures and low water content, and relative scarcity of PLA degrading organisms [189]. Distribution of PLA-degrading microorganisms in a natural environment is limited, and thus, PLA degradation in soil is slow or does not occur [190]. As degradation of PLA underneath the soil is based mainly on the chemical hydrolysis and microbial activity, this process can be supported at elevated temperature in a medium that is rich in micro-organisms and that has a high capacity to hold water [191].

The outcome of the PLA/mPE and PLA/mPE/E-GMA tests is similar to that for PLA. In both cases, the sample specimen before weathering (sample I) and the sample specimen underneath the soil after exposure to natural weathering are identical and do not show traces of degradation. The sample III of the binary and ternary blends, which is the sample specimen above the soil and exposed to UV radiation, behaves similar to the PLA sample III, and which confirms that mPE or E-GMA do not deteriorate the degradation mechanism of PLA.

In order to confirm the changes caused by photo-oxidation, the extent of PLA degradation was evaluated by analyzing Weight Average Molecular Weight (Mw) through GPC analysis. PLA is completely soluble in chloroform ($CHCl_3$), whereas mPE and E-GMA are insoluble. Thus, PLA was extracted from the blends by dissolving the blends in $CHCl_3$, followed by filtration. GPC analysis was performed on the samples before natural weathering and on the samples placed above the ground after 5 months of natural weathering. Table 15 summarizes the average molar mass values and the percentage of Mw degradation.

Table 15: Mw and percentages of Mw degradation of samples under natural weathering.

Sample	Exposure time [months]	Mw [g/mol]	% Mw degradation
PLA	0	230943	-
PLA	5	220019	5
PLA extracted from PLA/mPE	0	223776	-
PLA extracted from PLA/mPE	5	170175	24
PLA extracted from PLA/mPE/E-GMA	0	230846	-
PLA extracted from PLA/mPE/E-GMA	5	174154	25

After 5 months of natural weathering Mw of PLA is reduced by 5 %. Higher decrease in Mw is observed for the PLA extracted from PLA/mPE (24 %) and PLA/mPE/E-GMA (25 %). The decrease in Mw could be associated with the structural changes observed in the FT-IR spectrum. Compared to neat PLA, an inhomogeneous morphology of PLA/mPE and PLA/mPE/EGMA blends could result into easier penetration of water, thus enhancing the rate of PLA degradation.

This reveals that mPE and E-GMA accelerate PLA degradation and simultaneously provide an improvement in the tensile properties of PLA.

5.5. Summary on PLA/PE blend compatibilization and degradation study

In this chapter, it was demonstrated that an addition of 5 % E-GMA compatibilizer to PLA/HDPE and PLA/LDPE blends significantly improved the elongation at break of the resulting ternary blends and closely matched the elongation at break of PLA/LLDPE and PLA/mPE binary blends. Following the addition of the compatibilizer, the blend morphology transferred from a coarse to a fine dispersed PE phase. DSC experiments on PLA/E-GMA blends confirmed strong interaction of PLA and E-GMA that likely contributed to an improved elongation at break properties of the PLA/HDPE and the PLA/LDPE ternary blends. The addition of an interfacial modifier to the PLA/LLDPE and the PLA/mPE blends converted the elongated dispersed phase particles to spherical small droplets. However, the morphology development for PLA/LLDPE/E-GMA and PLA/mPE/E-GMA did not significantly influence the tensile properties of the blend.

A field test was performed with the objective to investigate the impact of mPE and E-GMA on the degradation properties of PLA, PLA/mPE binary and PLA/mPE/E-GMA ternary blends, where the samples were partially submerged under soil over five months. The thermal properties of sample specimens underneath the soil and above the soil were conducted through TGA at a mass loss of 10 % and 50 %. TGA analysis confirmed that in case of sample specimens placed on top of the soil and exposed to direct sunlight, the PLA/mPE/E-GMA sample specimen has better thermal stability compared to the pure PLA and PLA/mPE blends, which could be related to the interfacial stability that E-GMA incorporates into the blend system. In case of sample specimens underneath the soil, PLA/mPE showed minor degradation, whereas pure PLA and PLA/mPE/E-GMA did not degrade. The degradation of PLA/mPE could be attributed to the presence of micro voids that promote water intake and subsequent PLA hydrolysis.

FT-IR spectroscopy analysis of the samples confirmed that mPE and E-GMA do not hinder the degradation process of PLA for the sample specimens above the soil and exposed directly to the UV radiation. There were no signs of degradation for the sample specimens underneath the soil as per FT-IR spectroscopy. Additionally, GPC analysis was conducted on the PLA before weathering and on the PLA extracted from PLA/mPE and PLA/mPE/E-GMA sample specimens above the ground after five months of weathering period. GPC analysis confirmed that a decrease in molecular weight of PLA extracted from the blends was more pronounced as compared to the decrease in the molecular weight of pure PLA. Thus, confirming that mPE and E-GMA might accelerate degradation process of PLA in blend.

6. Nucleating agent for Polylactide and its effect on PLA/PE blends

The objective of this chapter is to examine the use of terephthaloyl-bis-N, N'-naphthalimidester (TN) as a nucleating agent (NA) for PLA, PLA/mPE binary and PLA/mPE/E-GMA ternary blends. DSC is used to evaluate the nucleating ability of different nucleating agents on the crystallization kinetics of PLA and PLA blends. The first part of the chapter presents the nucleating potential of TN and other commercially available nucleating agents on the non-isothermal crystallization behavior of two different PLA types. The scope of the examination is extended to determine the impact of the nucleating agents at different concentrations and thermal cooling/heating rates on PLA under non-isothermal and isothermal conditions. In the second part of this chapter, the impact of TN and commercial nucleating agents on non-isothermal crystallization behavior of PLA/mPE binary and PLA/mPE/E-GMA ternary blends is investigated. The motivation behind this study is to ensure that TN does not have an antagonistic effect on tensile properties of PLA/mPE binary and PLA/mPE/E-GMA ternary blends.

6.1. Non-isothermal crystallization behavior of PLA and nucleated PLA

An important factor affecting crystallization rate of PLA is its optical purity [192]. Therefore, two types of PLA that differ in L/D isomer ratio were selected. The L/D isomer ratios of PLA grade 4043D and PLA grade 4032D are 96:4 and 98:2, respectively. The nucleating power of TN was compared against the following commercially available nucleating agents: tetramethylenedicarboxylic dibenzoylhydrazide (TMC-306, in the chapter marked as TMC) and orotic acid (OA) [118,121,130,133,137]. PLA grade 4043D and PLA grade 4032D were blended with 0.5 % TMC, 0.5 % TN and 0.5 % OA. Prior to compounding, the nucleating agents and PLA were dried in a vacuum oven. Later, the dried nucleating agents were pre-mixed with PLA in a plastic bag until the mixture was optically homogeneous. A twin-screw extruder Process 11 operating in co-rotating mode was used for compounding. The processing details of twin-screw extruder Process 11 are summarized in the experimental section 10.4.

The crystallization kinetics of neat PLA and nucleated PLA were analyzed under non-isothermal conditions. Since the thermogram of the first heating cycle correlates to the thermal history during processing, evaluations are based on the thermogram of the first cooling and second heating cycle. The melt crystallization (T_{cm}) and the enthalpy (ΔH_{cm}) were determined during the first cooling scan, whereas glass transition temperature (T_g), peak temperature (T_{cc}) and enthalpy of the cold crystallization (ΔH_{cc}), melting temperature (T_m) and enthalpy of melting

(ΔH_m) were determined during the second heating scan. Percentage crystallinity (X_c) of neat PLA and nucleated PLA was calculated using equation 12.

$$X_c = \frac{\Delta H_{cm}}{\Delta H_m^\circ} \cdot 100\% \qquad (12)$$

ΔH_m° is the melt enthalpy of completely crystalline PLA, and its value is 93.7 J/g [193].

6.1.1. Thermal properties of PLA 4043D and nucleated PLA 4043D

Figure 45 shows the DSC thermogram of neat PLA 4043D (blue curve), PLA 4043D blended with 0.5 % of TMC (orange curve), 0.5 % of TN (black curve) and 0.5 % OA (green curve). The DSC cooling and heating curves were recorded at a rate of 5 °C/min. Table 16 summarizes the absolute values of DSC thermograms corresponding to Figure 45.

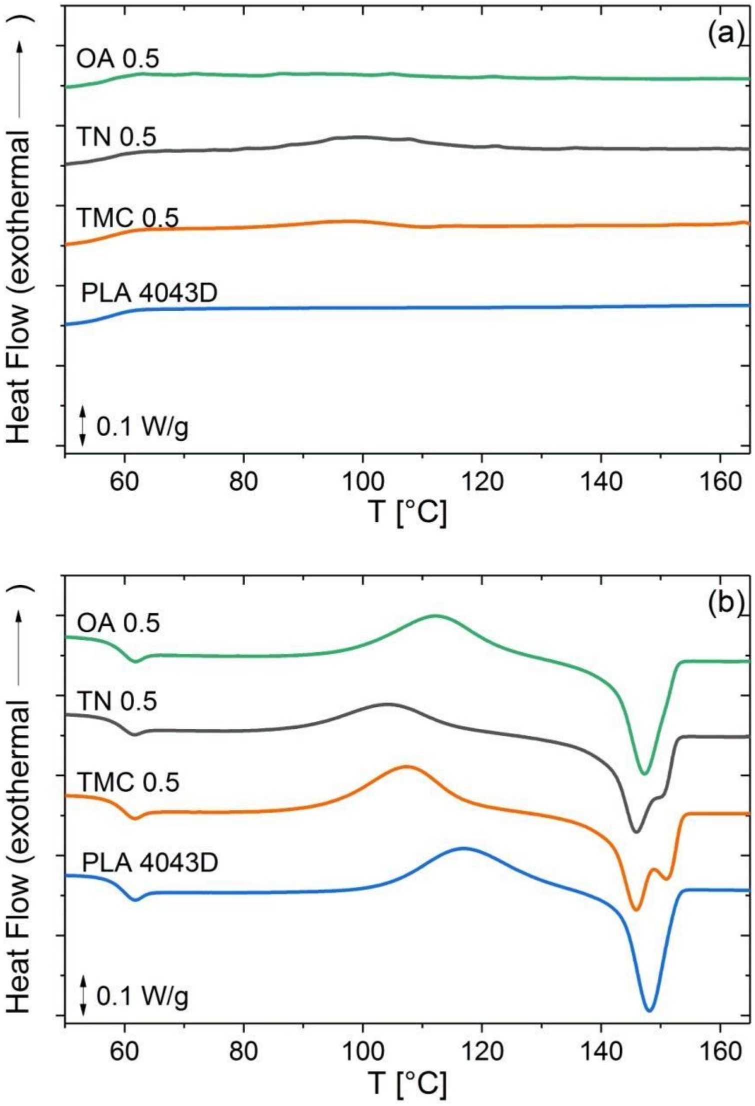

Figure 45: (a) DSC cooling curves and (b) subsequent DSC heating curves of the PLA 4043D (blue) and the nucleated PLA 4043D with 0.5 % of TMC (orange), TN (black) and OA (green) recorded at a rate of 5 °C/min.

The crystallization of PLA 4043D is not detectable in the cooling scan at cooling rate of 5 °C/min, which indicates an amorphous nature of PLA 4043D at room temperature. The kinetics are not fast enough to allow crystallization of PLA 4043D. In the subsequent DSC heating curve of PLA 4043D, after non-isothermal crystallization, glass transition (T_g) at 58 °C, cold crystallization peak (T_{cc}) at 117 °C and melting peak (T_m) at 148 °C are detected. The presence of T_{cc} peak indicates that the material is not amorphous but crystallizes at a very slow rate [130]. As shown in Table 16, the values of ΔH_{cc} and ΔH_m are similar and confirm the absence of crystals at room temperature.

Table 16: Thermal parameters obtained from DSC cooling and subsequent heating scans of neat PLA 4043D and PLA 4043D containing 0.5 % of TMC, 0.5 % of TN and 0.5 % of OA recorded at a rate of 5 °C/min.

PLA grade	NA	T_{cm} [°C]	ΔH_{cm} [J/g]	T_g [°C]	T_{cc} [°C]	ΔH_{cc} [J/g]	T_m [°C]	ΔH_m [J/g]	X_c [%]
PLA 4043D	-	-	-	58	117	22.5	148	22.5	0
	TMC	98	3	58	107	22	146/150	25	3
	TN	100	8	58	104	16	146/150	24	8
	OA	-	-	58	112	24	147	24	0

Upon cooling, the addition of TMC and TN to PLA 4043D induces crystallization at 98 °C and 100 °C, respectively. The addition of OA does not cause crystallization of PLA 4043D. In the subsequent heating process, a shift in T_{cc} of PLA 4043D to lower temperatures is observed after addition of TN and TMC, which could be an indication of a nucleating effect. In contrary to TN and TMC, OA has a limited nucleating effect on PLA 4043D, as T_{cc} of PLA 4043D undergoes a minimal change after addition of OA. The addition of TN and TMC to PLA shifts T_{cc} from 117 °C to 104 °C and 107 °C, respectively. In comparison to TMC-nucleated PLA, TN-nucleated PLA induces a slightly greater shift in T_{cc}, which indicates that the TN-nucleated sample crystallizes sooner upon heating.

In the heating scan of TN-nucleated and TMC-nucleated PLA 4043D, a double melting peak at 146 °C and 150 °C, respectively, is observed. When T_{cc} is below 120 °C, a double melting peak or a shoulder peak prior to the main melting peak might be an indication of the co-existence of two crystal forms, α- and α´-form crystal [130,194,195]. Only α´-form crystals are formed at T_{cc} below 100 °C, and α-form crystals are formed above 120 °C [196,197]. The α´- crystals are unstable and exhibit loose and disordered chain packing, and they transform into more stable and orderly packed α- crystals upon heating [194,197]. Consequently, the melting of preexisting α-crystals take place before the melting of the α-form crystals developed in the transition process [194,195].

6.1.2. Thermal properties of PLA 4032D and nucleated PLA 4032D

Figure 46 shows the DSC thermogram of neat PLA 4032D (blue), PLA 4032D blended with 0.5 % of TMC (orange), 0.5 % of TN (black curve) and 0.5 % OA (green). The DSC cooling and heating curves were recorded at the rate of 5 °C/min. Table 17 summarizes the absolute values of the DSC thermogram corresponding to Figure 46.

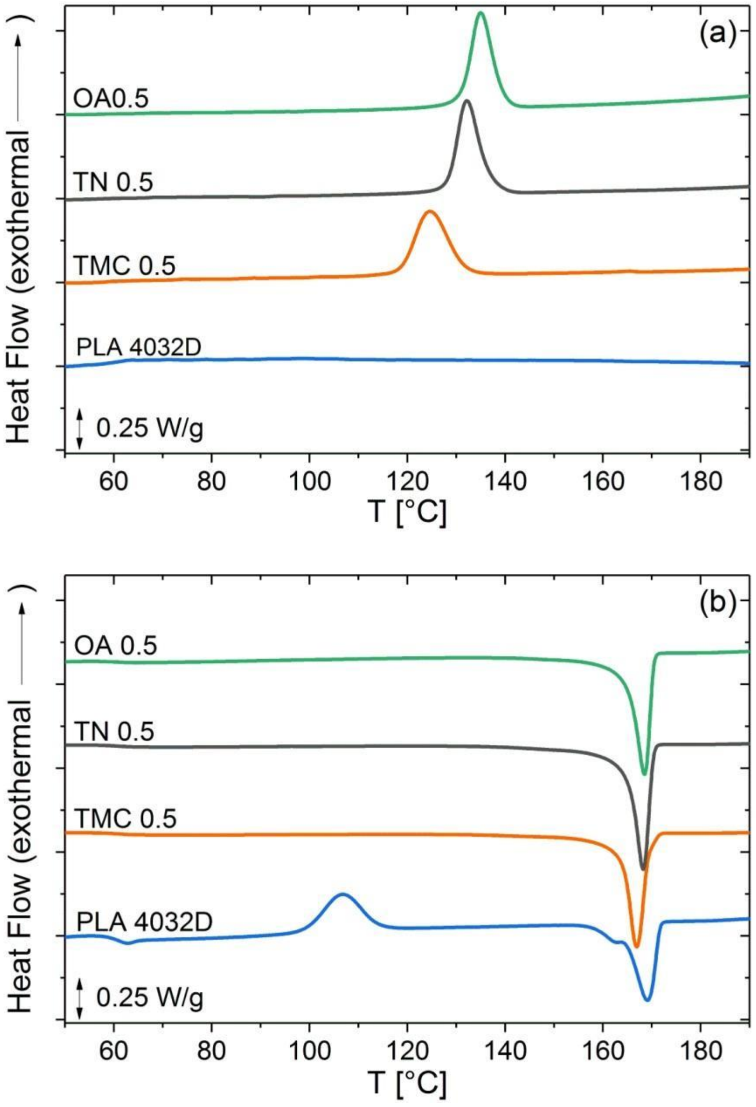

Figure 46: (a) DSC cooling and (b) subsequent heating curves of the PLA 4032D (blue) and the nucleated PLA 4032D with 0.5 % of TMC (orange), TN (black) and OA (green) recorded at a rate of 5 °C/min.

Crystallization of PLA 4032D upon cooling is not observed. Thus, regardless of the differences in optical purity, upon cooling, PLA 4032D follows a crystallization pattern similar to that of PLA 4043D. The presence of T_{cc} peak in the heating curve suggests that the material is not amorphous but crystallizes very slowly [130]. Furthermore, as shown in Table 17, identical ΔH_{cc} and ΔH_{m} values confirm the absence of crystals at room temperature. In addition to T_{g} at 61 °C and T_{cc} at 105 °C, a small shoulder peak at 163 °C prior to the main T_{m} at 169 °C is observed, which could be attributed to the melting-recrystallization-remelting process, as discussed earlier. The lower melting peak corresponds to melting of primary crystals, and the higher melting peak is associated with melting of the recrystallized crystals [123].

Table 17: Thermal parameters obtained from DSC cooling and subsequent heating scans of neat PLA 4032D and PLA 4032D containing 0.5 % of TMC, 0.5 % of TN and 0.5 % of OA recorded at a rate of 5 °C/min.

Polymer	NA	T_{cm} [°C]	ΔH_{cm} [J/g]	T_{g} [°C]	T_{cc} [°C]	ΔH_{cc} [J/g]	T_{m} [°C]	ΔH_{m} [J/g]	X_{c} [%]
PLA 4032D	-	-	-	61	106	32	163/169	32	0
	TMC	125	38	61	-	-	167	38	40
	TN	132	39	61	-	-	168	39	42
	OA	135	40	61	-	-	168	40	43

In the heating scan, a distinct difference in T_{cc} and T_{m} of PLA 4032D compared to PLA 4043D is observed, which can be associated with the difference in optical purity of two PLA samples. The stereoregularity of PLA 4043D is slightly disturbed by the presence of 4 % D-lactide configuration, hence it crystallizes slower upon heating (Figure 45b) contrary to PLA 4032D that has only 2 % D- lactide [198]. Moreover, as the D-lactide content increases, the melting point decreases [26].

As shown in the Figure 46a and Figure 46b, addition of TMC, TN and OA has a noticeable impact on the crystallization behavior of PLA 4032D. All the three nucleating agents dramatically enhance the crystallization exotherm of PLA 4032D. OA-nucleated PLA exhibits a higher peak crystallization temperature and enthalpy compared to TMC-nucleataed and TN-nucleated PLA, and affirm that the nucleating efficiency of OA is better than that of TMC and TN. The peak crystallization temperature and enthalpy for TN-nucleated PLA is 132 °C and 39 J/g, which confirms that the nucleating efficiency of TN is better than that of TMC-nucleated PLA (T_{cm} 125 °C and ΔH_{cm} 38 J/g). For all nucleated PLA samples, no traces of T_{cc} are observed during the heating scan, thus the crystallization of PLA is completed upon cooling. All the three nucleating agents drastically accelerate the crystallization of PLA 4032D.

6.1.3. Thermal properties of nucleated PLA 4032D at varying concentration of nucleating agents

In the previous section, the effect of different nucleating agents at a concentration of 0.5 % in PLA 4032D was examined. In the next step, the crystallization kinetics of the nucleated PLA under non-isothermal conditions and under varying concentration of the nucleating agents was analyzed. Two additional nucleating agents - ethylene bis-stearamide (EBS) and phthalimide (PI) - besides TMC, TN and OA, were included in the test matrix [26,117,121,125,126,135,199]. PLA 4032D was selected over PLA 4043D because it showed a distinctly better response to the nucleating agents as discussed earlier in section 6.1.2. The performance of different nucleating agents in PLA 4032D was investigated at concentration of 0.3 %, 0.5 % and 1 %. The DSC cooling and heating curves were recorded at a rate of 5 °C/min. Figure 47a- e are DSC thermograms of PLA 4032D nucleated with TMC, TN, OA, EBS and PI, respectively.

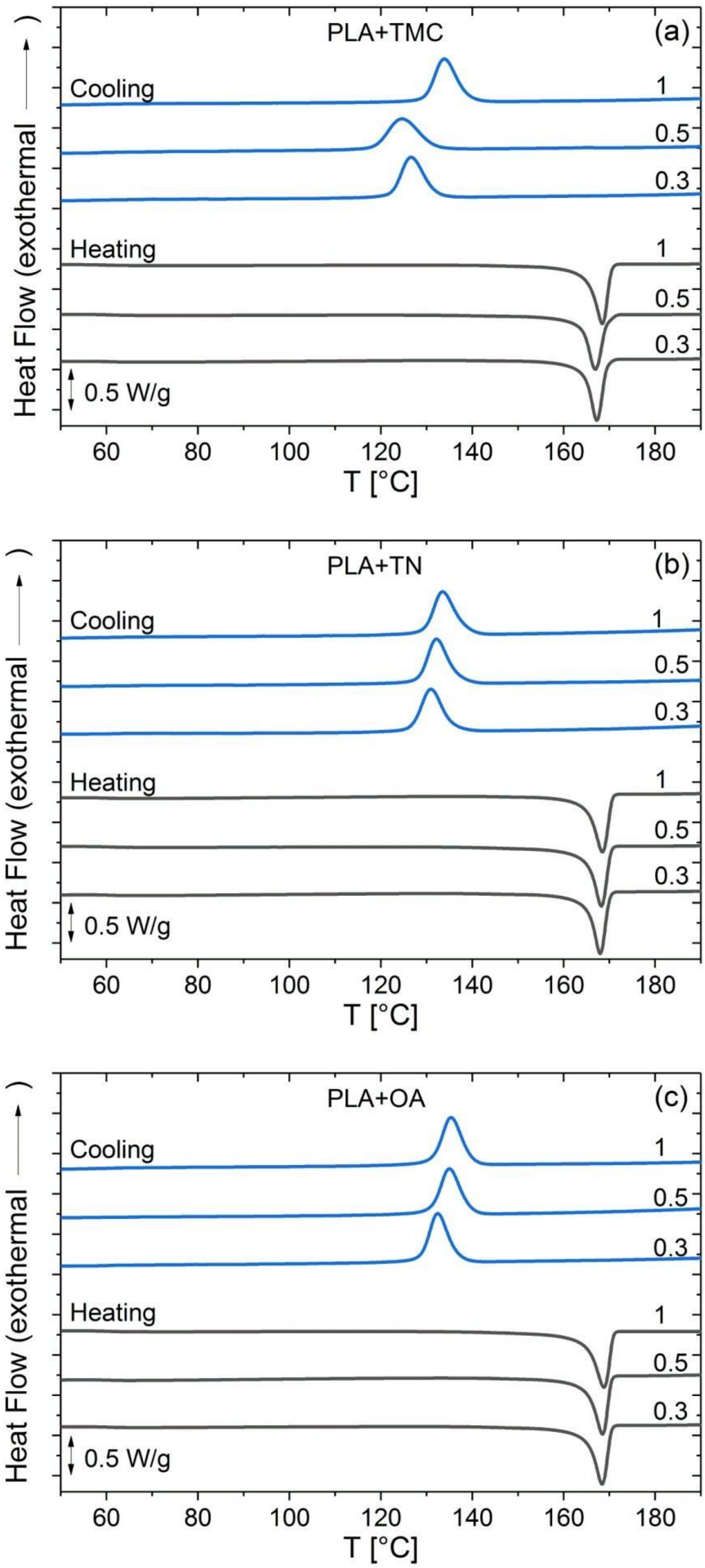
PLA+TMC
(a)
PLA+TN
(b)
PLA+OA
(c)
Cooling
Heating
1
0.5
0.3
0.5 W/g
Heat Flow (exothermal ⟶)
60
80
100
120
140
160
180
T [°C]

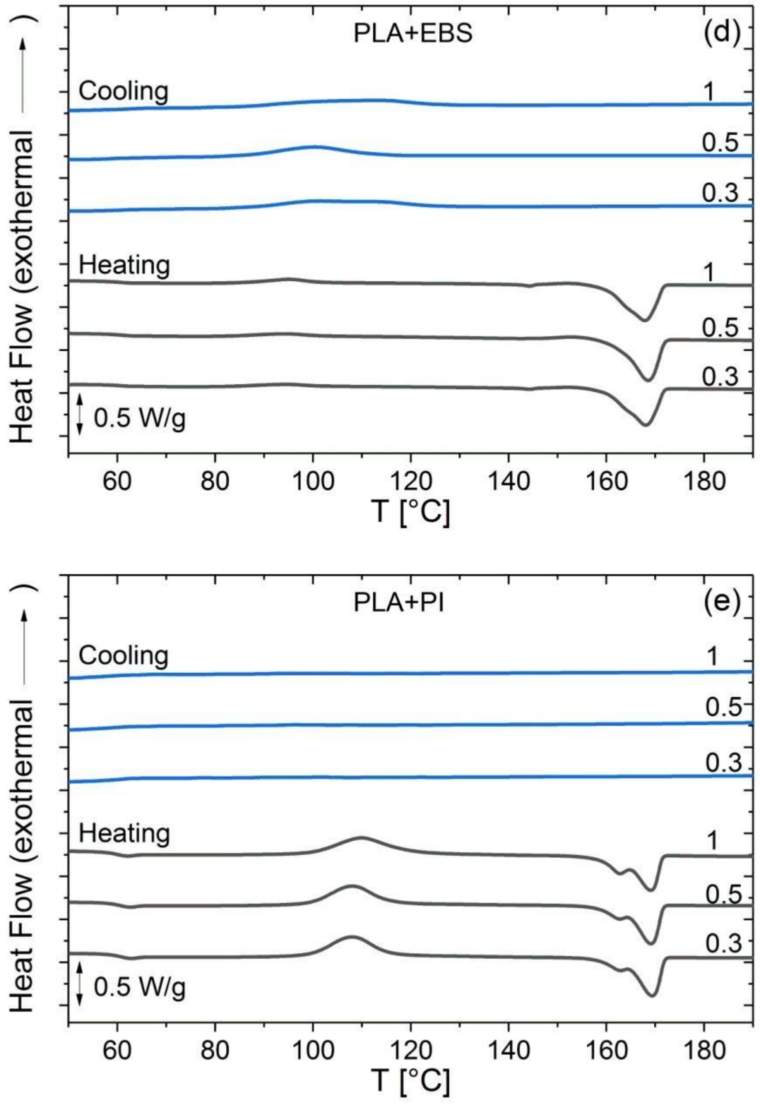

Figure 47: DSC cooling (blue) and subsequent heating curves (black) of PLA 4032D containing different loading (0.3 %, 0.5 % and 1 %) of (a) TMC (b) TN (c) OA (d) EBS and (e) PI recorded at 5 °C/min.

The cooling curves of TMC, TN and OA nucleated PLA 4032D indicate that adding only 0.3 % of each of the three nucleating agents improves crystallization of PLA 4032D. As discussed previously in section 6.1.2, PLA itself does not crystallize. As the loading of TMC, TN and OA in PLA 4032D increases, the crystallization peak of the nucleated PLA becomes sharper and shifts to a higher temperature. An exception is 0.5 % TMC, where a small drop in T_{cm} is observed. Upon addition of 0.3 % EBS, a tiny and broad crystallization peak appears on the cooling scan at approximately 100 °C, which is ~30 °C below T_{cm} of TMC, TN and OA nucleated PLA 4032D. No visible improvement in PLA crystallization behavior can be noticed with increasing addition of EBS, which confirms that EBS has a very limited influence on PLA crystallization. As shown in Figure 47e for PI-nucleated PLA, no crystallization peak appears for the additive loading in the range 0.3-1 % upon cooling at 5 °C/min. PI is not able to enhance the crystallization of PLA under the selected conditions.

The absence of a T_{cc} trace in the heating scan of TMC, TN and OA nucleated PLA 4032D confirms the completion of the crystallization of nucleated PLA upon cooling. In the heating scan of EBS nucleated PLA, the broad peak at 95 °C indicates cold crystallization of the amorphous zone. PI-nucleated PLA exhibits T_{cc} in the heating scans between 107-110 °C. Thus, EBS and PI have negligible influence on enhancing the crystallinity of PLA. Whereas, TMC, TN and OA play the role of efficient nucleating agents for PLA.

6.1.4. Thermal properties of nucleated PLA 4032D at varying cooling-heating rates

The thermal properties of PLA 4032D nucleated with varying concentration of TMC, TN and OA were investigated at heating and cooling rates of 10 °C/min and 20 °C/min, respectively. Based on the learnings from the previous section, EBS and PI were not included in the present study because both EBS and PI showed no effect on PLA 4032D. The information collected from the non-isothermal crystallization of PLA could be of use to model real industrial processes [200,201]. The peak of melt crystallization (T_{cm}) and degree of crystallinity (X_c) recorded from DSC cooling thermograms are plotted as a function of additive content in Figure 48.

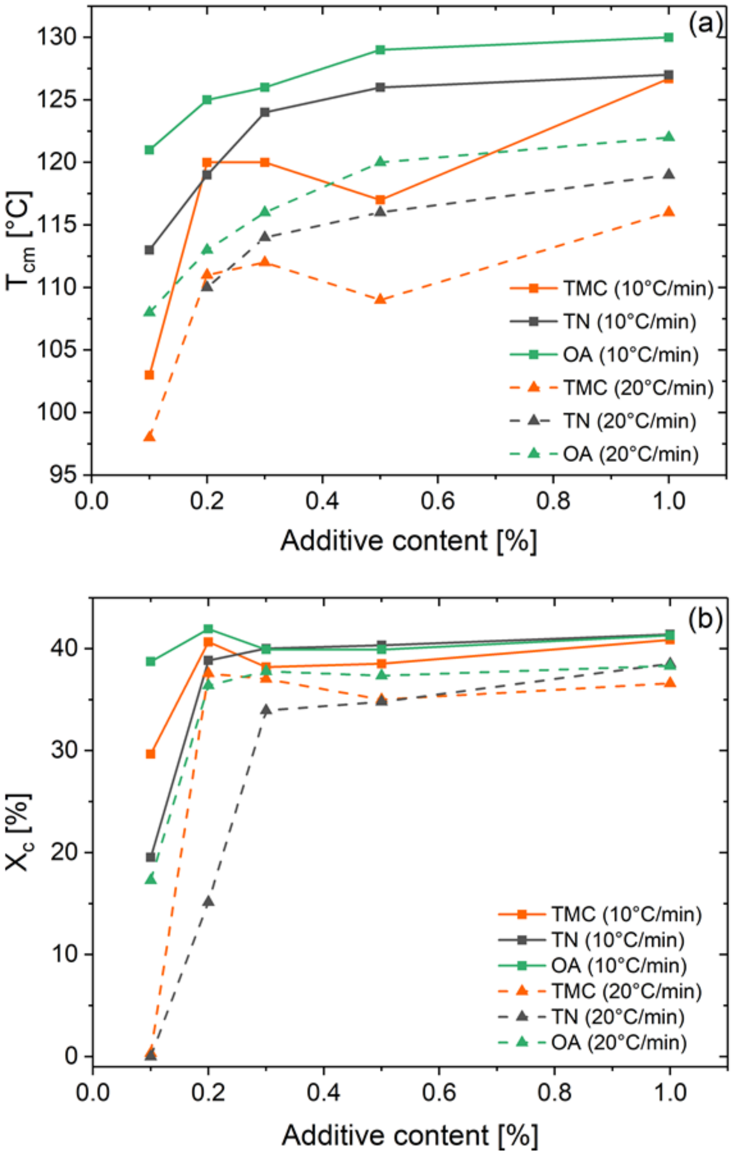

Figure 48: (a) Peak of melt crystallization (T_{cm}) and (b) crystallinity (X_c) of nucleated PLA 4032D as a function of additive content. Data obtained from DSC cooling traces recorded at 10 °C/min for (■): PLA/TMC, (■): PLA/TN, (■): PLA/OA and 20 °C/min for (▲): PLA/TMC, (▲): PLA/TN, (▲): PLA/TN.

Irrespective of the nucleating agent and the cooling rates, an increase in the amount of nucleating agent results in an increase in T_{cm} and X_c of nucleated PLA. A slight drop in T_{cm} of TMC-nucleated PLA is observed upon addition of 0.5 % TMC at 10 °C/min and 20 °C/min cooling rates. Whereas, a slight drop in X_c of TMC-nucleated PLA is observed at a concentration of 0.3 % at 10 °C/min and 20 °C/min cooling rates. Over the entire range of additive content and cooling rates, T_{cm} of TN-nucleated PLA is higher compared to TMC nucleated PLA, and slightly lower than OA-nucleated PLA. A similar pattern is observed in case of X_c as a function of additive concentration. Adding a very small amount of TN is effective in enhancing the melt crystallization of the PLA matrix. Even if the cooling rate is increased from 10 °C/min to 20 °C/min, TN nucleated PLA reaches up to 38 % crystallinity, which is very similar to that of

OA-nucleated PLA. The cooling rate of 20 °C/min is fast for standard DSC measurement, because higher cooling rates are considered to be uncontrollable in DSC measurement [202]. However, in order to predict nucleation ability in actual processing where cooling rates are faster, DSC measurement with heating /cooling rate of 30 °C/min for 1 % loading of TMC, TN and OA were conducted. Table 18 summarizes the corresponding DSC data.

Table 18: Thermal parameters obtained from DSC cooling and subsequent heating scans of PLA 4032D containing 1 % of either TMC, TN or OA recorded at a rate of 30 °C/min.

Composition	T_{cm} [°C]	ΔH_{cm} [J/g]	T_g [°C]	T_{cc} [°C]	ΔH_{cc} [J/g]	T_m [°C]	ΔH_m [J/g]	X_c [%]
PLA + 1 TMC	111	30	64	109	2	163	32	32
PLA + 1 TN	111	30	64	103	2	165	32	32
PLA + 1 OA	116	32	64	-	-	164	32	34

It is a common phenomenon that the higher the cooling rate, the lesser the time for the polymer chains to arrange regularly, and thus, the crystallization process is delayed [203]. Hence, a drop in T_{cm} and X_c of nucleated PLA samples is detected with an increased cooling rate. Nevertheless, the crystallization behavior of the nucleated PLA samples remains very good. Based on non-isothermal study, the nucleation ability of TN is comparable with that of TMC and OA, which are considered as very effective nucleating agents for PLA [129,130,133,137].

6.2. Isothermal crystallization behavior of PLA and nucleated PLA

To study the effect of a nucleating agent on the isothermal crystallization kinetics of PLA 4032D, the samples were cooled from the melt to the desired crystallization temperature T_{iso} and the samples were held at T_{iso} until the crystallization process was complete. The DSC isothermal crystallization exotherm curves of PLA (blue curve), PLA nucleated with 0.3 % of TMC (orange curve), TN (black curve) and OA (green curve) crystallized at 130 °C are shown in Figure 49. The neat PLA does not show a crystallization peak even after a crystallization time of 40 min. On addition of 0.3 % TMC, TN, or OA to PLA, a sharp crystallization peak appears and the crystallization process completes in less than 3 min for all nucleated samples.

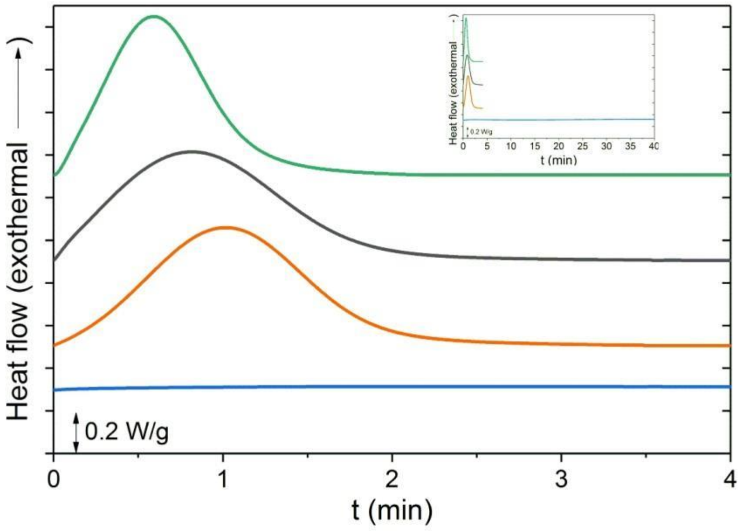

Figure 49: Isothermal crystallization exotherms of PLA 4032D (blue) and PLA 4032D nucleated with 0.3 % of TMC (orange), 0.3 % TN (black) and 0.3 % OA (green) at 130 °C.

Isothermal crystallization kinetics can be evaluated based on crystallization half-time $t_{1/2}$, which is defined as the time needed to achieve 50 % of the sample final crystallinity. The half-time $t_{1/2}$ can be directly obtained from the plot of relative crystallinity (X_t) as a function of t. The relative crystallinity (X_t) is expressed as the ratio of the area of the exotherm at crystallization time t to the total area of the exothermal peak, as per equation 13.

$$X_t = \frac{\int_0^t (dH/dt)dt}{\int_0^\infty (dH/dt)dt} \tag{13}$$

In equation 13, dH/dt is the heat flow rate at time t.

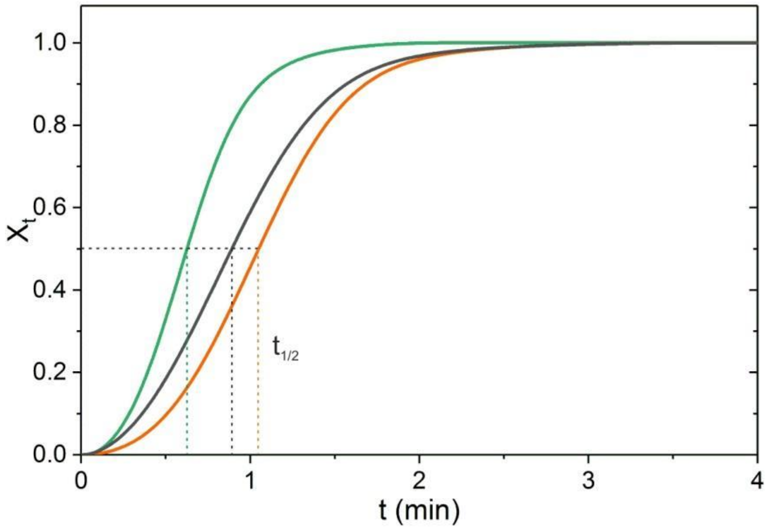

Figure 50: Relative crystallinity (X_t) as a function of crystallization time (t) of PLA 4032D nucleated with 0.3 % TMC (orange), 0.3 % TN (black) and 0.3 % OA (green) at 130 °C.

Figure 50 is the plot of X_t as a function of t for PLA nucleated with 0.3 % TMC (orange curve), 0.3 % TN (black curve) and 0.3 % OA (green curve). PLA nucleated with OA exhibits the highest crystallization rate, followed by PLA nucleated with TN, and PLA nucleated with TMC. The values of $t_{1/2}$ for each sample are summarized in Table 19.

Table 19: The crystallization halt-time $t_{1/2}$ obtained for nucleated PLA 4032D at 130 °C.

Composition	$t_{1/2}$ [min]
PLA + 0.3 % TMC	1.05
PLA + 0.3 % TN	0.88
PLA + 0.3 % OA	0.62

As shown in Table 19, an addition of 0.3 % TMC results in a crystallization half time of 1.05 min at 130 °C, which further decreases to 0.88 min upon addition of 0.3 % TN. The lowest value of crystallization half time of 0.62 min is achieved for PLA with 0.3 % OA. Thus, TN provides better nucleating efficiency compared to TMC, and is comparable to OA. A short crystallization half time is an important asset to industry processes like injection molding and compression molding, where rapid and uniform cooling of a molded object can result in increased productivity. Thus, it is possible that TN could serve as a powerful nucleating agent to facilitate quicker cooling and increased productivity.

Further, PLA was nucleated with different loadings of TN, such as 0.1 %, 0.2 % and 0.3 %, and the isothermal crystallization behavior of PLA in a temperature range between 130 °C and 145 °C was examined. Figure 51 is a plot of $t_{1/2}$ as a function of the TN content in PLA, where the black curve, blue curve and red curve show the isothermal crystallization behavior of PLA at 130 °C, 140 °C and 145 °C, respectively. The crystallization half time increases as the isothermal crystallization temperature increases from 130 °C to 145 °C. Moreover, with an increase in the concentration of the TN content in PLA, a progressive decrease of the crystallization half time is observed. The lowest $t_{1/2}$ value was achieved for PLA with 0.3 % TN at 130 °C. Thus, the level of improvement of the crystallization behavior of PLA by TN depends upon the crystallization temperature and the TN concentration.

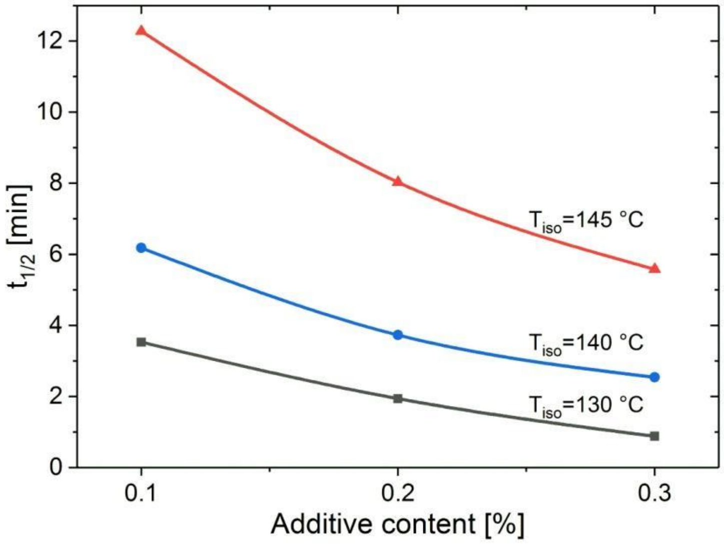

Figure 51: Dependency of crystallization half-time ($t_{1/2}$) on TN loading measured at crystallization temperature (T_{iso}) of 130 °C, 140 °C and 145 °C.

6.3. Non-isothermal crystallization behavior of non-nucleated and nucleated PLA/mPE binary and PLA/mPE/E-GMA ternary blends

Before analyzing the crystallization behavior of nucleated blends, the crystallization behavior of non-nucleated PLA/mPE binary and PLA/mPE/E-GMA ternary blends was studied. Thereafter, the tensile properties of nucleated binary and ternary blends were evaluated. As discussed in chapter 3 and chapter 5, PLA/mPE and PLA/mPE/E-GMA blends have superior tensile properties compared to pure PLA. Thus, the objective of this section is to understand the impact of TN on the tensile properties of the blends system.

All blends contain PLA 4032D as the matrix phase. The blends were prepared using an extruder equipped with slit die and conveyor belt at the die exit. The thermal properties of the resulting blends were evaluated via DSC thermogram of the first cooling and second heating cycle at cooling/heating rate of 10 °C/min.

6.3.1. Non-isothermal crystallization behavior of PLA/mPE and PLA/mPE/E-GMA blends

Before thermal properties of the blends were investigated, individual DSC cooling traces of mPE and E-GMA homopolymers were obtained. Figure 52 shows DSC cooling scans of mPE (gray trace) and E-GMA (blue trace) at a cooling rate of 10 °C/min.

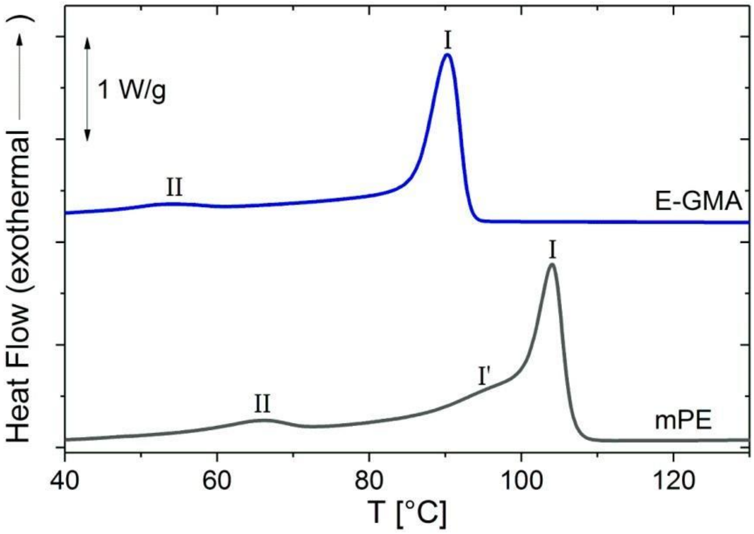

Figure 52: DSC cooling traces of mPE (black) and E-GMA (blue) recorded at a rate of 10 °C/min.

The DSC cooling curve of mPE reveals two main exotherms - exotherm I and exotherm II. Although mPE is considered as a homogenous material due to a narrow molecular weight distribution and uniform short-chain branch distribution, there is evidence that mPE possesses intra- and intermolecular heterogeneity, which could be related to the multiple exothermic peaks visible in Figure 52 [204,205]. The major crystallization exotherm I has a peak crystallization temperature at 104 °C and a broad shoulder at 95 °C (I'). The major crystallization exotherm I could be a result of the crystallization of heterogeneously nucleated long linear segments in mPE and are known as primary crystallization. The long linear segments in mPE crystallize faster than short chain crystalline sections, which usually crystallize at slightly lower temperatures, and are known as secondary crystallization (exotherm I') [206–209]. The tie molecules formed during the lamellar folding process are not incorporated into crystallization at a high temperature and remain in the melt due to a restriction in their topological movement through the already formed lamellas [209,210]. Nevertheless, at higher undercooling, tie molecules can aggregate locally into bundle-like inter-crystalline links leading to the second stage of secondary crystallization, and give rise to an exotherm II at 66 °C [209,210]. Similar to the cooling curve of mPE, two crystallization exotherms for E-GMA are observed. The peak crystallization exotherm I of E-GMA and secondary crystallization exotherm II occurs at 90 °C and 54 °C, respectively. As discussed in the previous sections, PLA itself does not crystallize during the cooling process.

In the next step, the crystallization behavior of PLA/mPE binary blends and PLA/mPE/E-GMA ternary blends was investigated. The PLA/mPE blend was extruded in the blend ratio of 80:20 / wt %: wt % / PLA/mPE. The ternary blend was prepared by adding 5 % E-GMA to the PLA/mPE binary blend. Figure 53 shows DSC cooling scans of the PLA/mPE binary and the

PLA/mPE/E-GMA ternary blends. Table 20 summarizes the DSC data corresponding to Figure 52 and Figure 53.

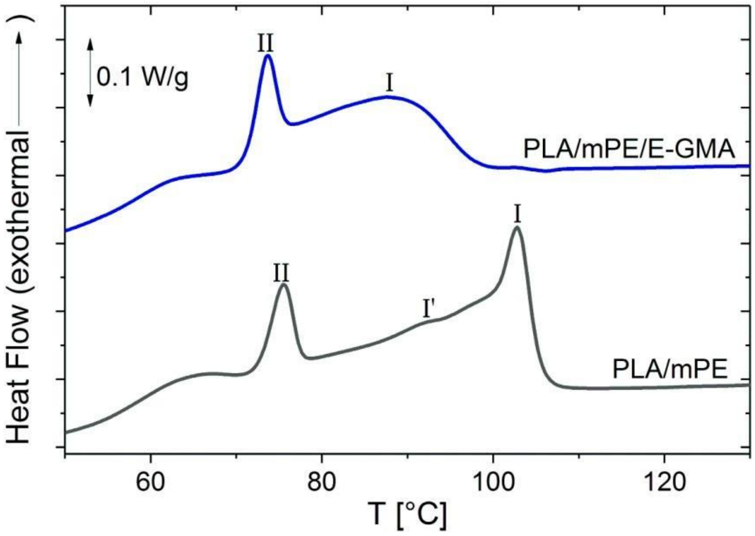

Figure 53: DSC cooling traces of PLA/mPE (black) and PLA/mPE/E-GMA (blue) recorded at a rate of 10 °C/min.

Table 20: Thermal parameters obtained from DSC cooling scans of mPE, E-GMA and their blends with PLA recorded at a rate of 10 °C/min.

Composition	T_{cm} [°C] (I)	(I')	(II)	$\Delta H_{cm(I+I'+II)}$ [J/g]
mPE	104	95	66	120
E-GMA	90	-	54	89
PLA/mPE	103	94	75	19
PLA/mPE/E-GMA	88	-	74	15

The cooling curve of the PLA/mPE binary blend exhibits a characteristic exotherm consisting of a high-temperature crystallization peak (I), a broad low-temperature crystallization peak located close to it (I'), and a very-low temperature crystallization peak (II). A separate crystallization peak that could be attributed to the crystallization of PLA matrix is not observed. In comparison to bulk mPE, the peak labeled I is shifted slightly to a lower crystallization temperature at 103 °C, whereas peak II is shifted to a higher crystallization temperature at 75 °C. The ratio of peak area in the PLA/mPE blend and bulk mPE is different.

The exotherm II in PLA/mPE is more prominent than that in neat mPE, which could be attributed to the fractionated crystallization of the dispersed mPE phase. In a bulk polymer, the crystallization is triggered by active heterogeneity that dominates the crystallization of the polymer [211]. The blending process divides the polymer into droplets that might contain heterogeneities as well as clean droplets that do not possess any impurities. The clean droplets undergo homogeneous nucleation on their own, giving rise to an exothermic peak at higher supercooling (exotherm II) [212]. During non-isothermal cooling, nucleation of the crystallizable polymer is restricted to the volume of the droplet [213]. It has been reported that nucleation in droplets is slightly more difficult than in bulk material, which could cause the shift of exotherm I to a lower crystallization temperature [211].

Addition of the compatibilizer E-GMA to the binary blend results in a distinctly different exotherm compared to the exotherm of the binary blend. The sharp crystallization exotherm I is not observed. Instead, a broad exotherm extending from 98 °C to 70 °C appears, which overlaps with the low temperature exotherm II at 74 °C. The lack of the sharp crystallization peak at the high temperature could be related to the change in morphology caused by the addition of E-GMA, as reported in chapter 5. In a compatibilized blend, there is an increase in the number of finely dispersed minor phase particles. Thus, the probability of finding heterogeneities in a large number of mPE droplets decreases, thereby favoring the possible activation of homogeneous nucleation [211]. Additionally, the olefin segments of E-GMA can be partially miscible with PE, which could cause deterioration of the crystallization of PE [214].

6.3.2. Non-isothermal crystallization behavior of nucleated PLA/mPE and PLA/mPE/EGMA blends

Figures 54a and 54b show DSC cooling scans of the PLA/mPE binary blend and the PLA/mPE/E-GMA ternary blend nucleated with 1 % of TMC (orange), TN (black) and OA (green), respectively.

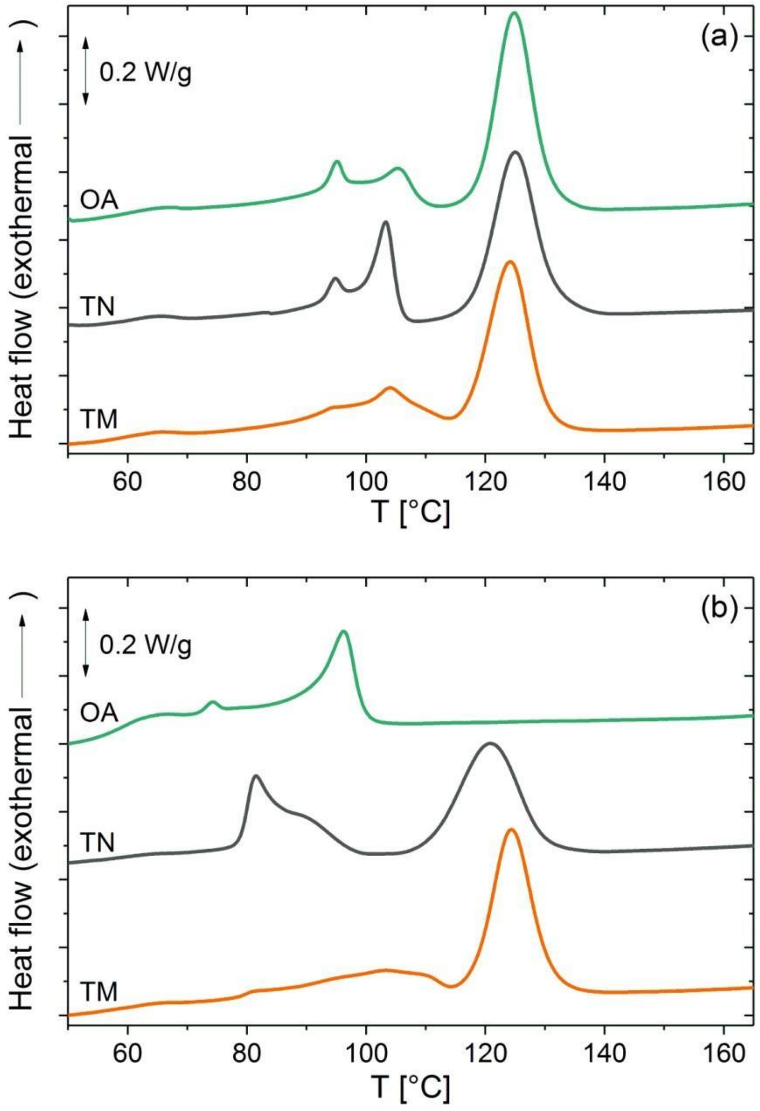

Figure 54: DSC cooling traces of (a) PLA/mPE and (b) PLA/mPE/E-GMA blends containing 1 % of TMC (orange), TN (black) or OA (green) recorded at a rate of 10 °C/min.

As shown in Figure 54a, an exothermic peak corresponding to the crystallization of PLA is observed upon addition of TMC, TN and OA to the binary PLA/mPE blend, unlike in the non-nucleated PLA/mPE binary blends (Figure 53). Contrary to the non-nucleated PLA/mPE blend, the nucleated PLA/mPE blend depicts a distinct two-step process of mPE crystallization that occurs between 110 °C and 80 °C, which could be attributed to crystallization of a less linear fraction of mPE triggered by the nucleating agent. Moreover, the low temperature crystallization exotherm (II) in mPE disappears and an overall decrease in crystallization enthalpy is observed. All three nucleating agents have similar impact on the crystallization behavior of the PLA/mPE binary blend.

In a manner similar to nucleated binary blends, upon addition of TN and TMC to E-GMA compatibilized PLA/mPE ternary blends, characteristic crystallization peaks of PLA are visible at 121 and 125 °C, respectively (Figure 54b). In case of the TN-nucleated ternary blend, a broad crystallization exotherm ranging from 101 to 67 °C with a peak at 81 °C is observed, and a high temperature shoulder appears at the position of mPE exotherm I. Whereas, for the TMC nucleated ternary blend, the crystallization exotherm of mPE is flattened. Addition of OA to the compatibilized blend does not cause crystallization of PLA, while only two crystallization peaks at 96 °C and 74 °C, which are characteristic of mPE, are visible. In fact, the cooling trace of the OA-nucleated ternary blend is similar to that of the non-compatibilized PLA/mPE blend upon cooling. The results indicate that the effectiveness to compatibilize the PLA/mPE blend by E-GMA decreases by addition of OA, which could be explained by a reaction between epoxide moieties and benzoic acid molecules [215]. A potential reaction between E-GMA epoxide functions and carboxyl group of OA results in the encapsulation of OA within the E-GMA phase and thereby prevents dispersion of the nucleating agent in the PLA phase. Thus, one could expect the inhibition of matrix crystallization. Table 21 summarizes the DSC data corresponding to Figures 54a and 54b.

Table 21: Thermal parameters obtained from DSC cooling scans of PLA/mPE and PLA/mPE/E-GMA blends containing 1 % of nucleating agent.

Composition	$T_{cm(PLA)}$ [°C]	ΔH_{cm} [J/g]	T_{cm} [°C]			$\Delta H_{cm(I+I'+II)}$ [J/g]
			(I)	(I')	(II)	
PLA/mPE/TMC	124	23	104	95	-	8
PLA/mPE/TN	125	27	103	95	-	13
PLA/mPE/OA	125	27	105	95	-	11
PLA/mPE/E-GMA/TMC	124	23	103	80	-	8
PLA/mPE/E-GMA/TN	121	23	90	81	-	13
PLA/mPE/E-GMA/OA	-	-	96	-	74	14

6.3.3. Effect of nucleating agents on the mechanical properties of the PLA/mPE binary blend and the PLA/mPE/E-GMA ternary blend

The sample specimens for tensile testing were punched directly out of the extruded film. The degree of crystallinity of the nucleated PLA/mPE binary blend and the nucleated PLA/mPE/E-GMA ternary blend presented so far were recorded at the second heating scan. However, the degree of crystallinity of the sample measured under controlled non-isothermal conditions does not represent the degree of crystallinity of the sample as obtained directly from processing.

Thus, the degree of crystallinity obtained from the first heating scan is referred while discussing mechanical properties of PLA blends.

Table 22 summarizes cold crystallization enthalpy (ΔH_{cc}) and enthalpy of melting (ΔH_m) of PLA 4032D and nucleated PLA 4032D after the first heating scan at 10 °C/min. PLA 4032D was blended with 1 % of TMC, TN or OA. As shown in Table 22, ΔH_{cc} and ΔH_m are similar for non-nucleated PLA 4032D and nucleated PLA 4032D, irrespective of the choice of nucleating agent. This is an indication that the extruded material, regardless of its composition, remains amorphous due to rapid cooling of the extruded film at the die exit.

Table 22: Thermal parameters obtained from the DSC first heating scan of PLA 4032D and PLA containing 1 % of either TMC, TN or OA, recorded at a rate of 10 °C/min.

Composition	ΔH_{cm} [J/g]	ΔH_m [J/g]
PLA 4032D	35	35
PLA + 1 TMC	35	35
PLA + 1 TN	35	35
PLA + 1 OA	31	31

The mechanical properties of PLA 4032D and PLA 4032D blended with 1% of TN, TMC and OA are investigated, and the test results are summarized in Table 23.

Table 23: Mechanical properties of PLA 4032D and PLA containing 1 % of either TMC, TN or OA.

Composition	Elasticity Modulus [MPa]	Elongation at break [%]
PLA 4032D	1955 ± 90	9 ± 2
PLA + 1 TMC	2240 ± 54	25 ± 12
PLA + 1 TN	2130 ± 31	18 ± 12
PLA + 1 OA	2200 ± 57	10.7 ± 1

The modulus of elasticity (E-modulus) and elongation at break of PLA 4032D increases upon addition of TN, TMC or OA, which is an indication that the additive acts as a filler to improve the material stiffness despite the absence of crystals. The increase in stiffness of PLA 4032D by addition of the nucleating agent is similar regardless of the choice of the nucleating agent.

Similar to nucleated and non-nucleated PLA 4032D, nucleated and non-nucleated PLA/mPE binary and PLA/mPE/E-GMA ternary blends do not show signs of crystalline behavior. In the next step, the mechanical properties of PLA 4032D, non-nucleated and nucleated PLA/mPE binary and PLA/mPE/E-GMA ternary blends are evaluated. 1 % TN, TMC or OA was added to each of the blends. The summary of the test results is shown in Table 24.

Table 24: Mechanical properties of PLA 4032D and nucleated PLA/mPE binary and PLA/mPE/E-GMA ternary blends. Each blend contains 1 % of nucleating agent.

Composition	Elasticity Modulus (MPa)	Elongation at Break (%)
PLA 4032D	1955 ± 90	9 ± 2
PLA/mPE	1439 ± 55	413 ± 29
PLA/mPE/TMC	1558 ± 20	85 ± 105
PLA/mPE/TN	1447 ± 40	7 ± 2
PLA/mPE/OA	1450 ± 61	6 ± 1
PLA/mPE/E-GMA	1386 ± 58	467 ± 8
PLA/mPE/E-GMA/TMC	1610 ± 53	376 ± 29
PLA/mPE/E-GMA/TN	1450 ± 56	442 ±17
PLA/mPE/E-GMA/OA	1330 ± 129	59 ± 61

Table 24 shows that addition of mPE to PLA 4032D results in a slight reduction in the elasticity modulus and a substantial increase in elongation at break. However, addition of TMC, TN or OA causes a substantial drop in elongation at break of the binary blends. The PLA/mPE blend with TN or OA exhibits a lower elasticity modulus and a lower elongation at break compared to the PLA/mPE blend with TMC.

The strong drop in elongation at break upon the addition of nucleating agent could be explained on the basis of the blend morphology shown in the Figure 55. The addition of TN to PLA/mPE blend significantly changes the morphology of the dispersed phase. The elongated mPE fibrils in PLA/mPE blend are responsible for a good stress transfer between PLA and mPE phase and therefore high elongation at break change into droplet upon addition of TN to the blend composition. It is expected that additive incorporation might have an impact on the viscosity of the blend components, which could explain the morphology alteration. Blend compatibilization with E-GMA leads to finer morphology of dispersed phase that contribute to the enhancement of elongation at break.

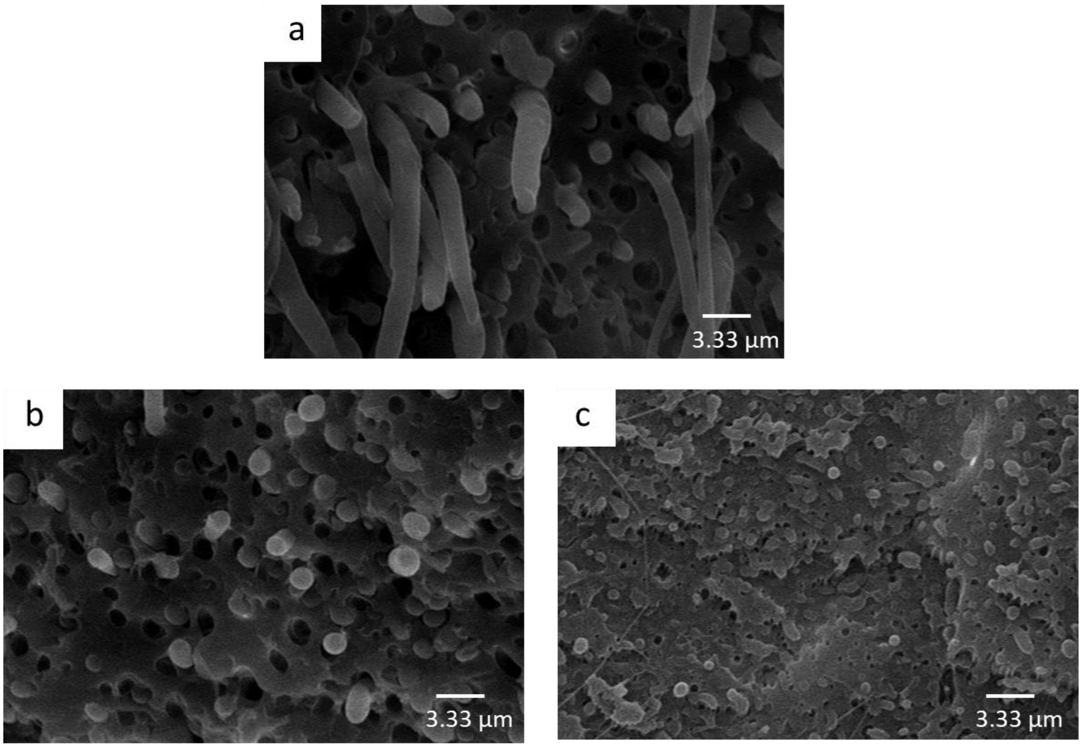

Figure 55: SEM morphologies of the cryogenically-fractured surface of (a) PLA/mPE, (b) PLA/mPE/TN and (c) PLA/mPE/E-GMA/TN.

Furthermore, Table 24 shows that addition of E-GMA to the PLA/mPE blend results in a slight reduction in the elasticity modulus and a substantial increase in elongation at break compared to the non-compatibilized PLA/mPE blend. Upon addition of TN and TMC to PLA/mPE/E-GMA, an improvement in the elasticity modulus is noticed. The effect of adding TN to the ternary blend on elongation at break is greater than that of adding TMC. The addition of TN increases the elongation at break to 442 % and E-modulus to 1450 MPa of the ternary blend, whereas, the addition of TMC increases the elongation at break to 376 % and E-modulus to 1610 MPa.

This ensures a relatively good balance of high stiffness and flexibility. Whereas, addition of OA to the PLA/mPE/E-GMA blend substantially deteriorates the elongation at break of the non-nucleated PLA/mPE/E-GMA blend.

6.4. Summary on nucleating agent for Polylactide and its effect on PLA/PE blends

The objective of this chapter was to investigate the nucleating ability of terephthaloyl-bis-N, N'-naphthalimidester (TN) on PLA and to compare the nucleating power of TN against commercial nucleating agents. Two PLA grades - PLA 4043D and PLA 4032D - were selected, which did not crystallize when slowly cooled from the melt.

Based on the crystallization kinetics study under non-isothermal conditions at heating/cooling rates of 5 °C/min, minimal response to various nucleating agents was noticed for PLA 4043D. Contrary to PLA 4043D, a noticeable improvement was observed in the crystallization behavior of PLA 4032D after addition of as less as 0.3 % of TN. Its nucleating ability was comparable to that of the commercial nucleating agent OA but superior to TMC. Whereas, the nucleating efficiency of two additional commercial nucleating agents EBS and PI was negligible on improvement of PLA 4032D crystallinity.

The scope of the investigation was broadened to varying heating/cooling rates of 10 °C/min, 20 °C/min and 30 °C/min and varying additive content. Almost over the entire range of evaluated additive concentration and cooling rates, OA was the most effective nucleating agent for PLA 4032D, followed by TN, which was consistently better than TMC. Even at a cooling rate of 30 °C/min, TN-nucleated PLA provided excellent crystallization temperature and enthalpy.

Under isothermal conditions, addition of 0.3 % TN, TMC or OA to PLA resulted in completion of the crystallization process at 130 °C in less than 3 minutes for all nucleated PLA samples. Based on the crystallinity half time $t_{1/2}$ analysis, a high crystallization rate for PLA nucleated with TN was confirmed, which could be an important asset in industry processes to improve productivity.

All three nucleating agents showed similar impact on the non-isothermal crystallization behavior of PLA in PLA/mPE blend, triggering an exothermic peak corresponding to the crystallization of PLA. In case of the PLA/mPE/E-GMA ternary blend, a characteristic crystallization peak of PLA was observed for TN and TMC nucleated ternary blends. Addition of OA to the compatibilized blend did not cause crystallization of PLA.

The tensile properties of PLA 4032D, PLA/mPE binary blends and PLA/mPE/E-GMA ternary blends with 1 % of TN, TMC or OA were tested. Finally, the samples subjected to the mechanical testing were not in the crystalline state. Blending PLA/mPE with TN, TMC or OA showed deterioration in the elongation at break, whereas addition of TN or TMC to E-GMA compatibilized PLA/mPE ternary blends increased the elasticity modulus but the elongation at break remained unaffected. Thus, the presence of E-GMA in the PLA/mPE blend system is necessary to sustain high elasticity modulus and elongation at break. Addition of OA to E-GMA compatibilized PLA/mPE ternary blends significantly deteriorated the elongation at break of non-additized ternary blend, while the elasticity modulus remained unaffected.

7. Summary

The objective of the present thesis was the improvement of the tensile properties and crystallization properties of PLA. Considering that the tensile properties of PLA is a vast field of research, the focus was laid on the enhancing of the elongation at break of PLA without deteriorating the degradation property of PLA. Another objective linked to the tensile property improvement was to develop a synthetic route to functionalize a commercially available hyperbranched polymer to enhance the compatibility of PLA/PE blends.

The strategy to improve the elongation at break was based on the theory of polymer blends. First, the binary blends comprising of PLA and different PE-types - HDPE, LDPE, LLDPE and mPE - were prepared in a twin-screw extruder. PLA-HDPE and PLA-LDPE blends exhibited a low elongation at break; whereas PLA-LLDPE and PLA-mPE blends exhibited a very high elongation at break. The addition of PE to PLA dropped the elasticity modulus of the PLA-PE blends, which could be due to the plasticizing effect induced by PE into the blend system. The morphology of the blends was thoroughly investigated, and correlations were drawn between the blend morphology and the elongation at break. The low elongation at break of PLA/HDPE and PLA/LDPE blends was related to weakly-adhered large globules of HDPE and LDPE in the PLA matrix. On the other hand, a very high elongation at break of PLA/LLDPE and PLA/mPE was related to elongated microfibrils of the dispersed phase, interpenetrated in the PLA matrix.

The impact of the drawing method on the morphology of PLA-PE blends was evaluated with a calendar roller system at the die exit, that imparted an elongation flow field on the extruded material. PLA-HDPE and PLA-mPE blends were prepared under three different conditions. In one case, the blends were cooled directly in a water bath, and in the other two cases, the blends were drawn continuously at a draw ratio of 4.5 and 9. The blends cooled directly in a water bath exhibited a globular morphology, which indicated poor interfacial adhesion properties. Upon drawing, PLA-mPE blend exhibited fine fibrillar morphology of mPE dispersed well in PLA matrix with very few cavities present. Similar observations were made at both draw ratios. In case of drawn PLA-HDPE blends, the diameter of HDPE droplets reduced progressively with an increasing draw ratio because of intensive stretching deformation.

The second strategy to improve the elongation was based on the use of compatibilizers in the blend composition. The topic of ternary blends consisted of two parts, functionalization of a hyperbranched polymer towards a potential new class of compatibilizers for PLA/PE blends and PLA/PE blends comprising of a compatibilizer such as E-GMA. Boltorn™ HB20 (H0), a commercially available hyperbranched polyester polyol was selected as a scaffold and was functionalized with stearic acid (SA) and PLA in a two-step process. Prior to the functionalization of H0 with SA and PLA, a model study was conducted to determine the degree of functionalized -OH groups. The so-called 'TAI-model' was based on trichloracetylisocyanate (TAI) functionalized H0, where the degree of functionalization was estimated via ^{1}H-NMR spectroscopy. The TAI-model was a very important tool that enabled quantification of the residual -OH groups during the functionalization of H0 with SA and PLA.

In the first step, SA was added to H0 in two molar ratios; H0:SA 1:8 (H08) and 1:12 (H12). A stearyl substitution of 48 % in H08 and 78 % in H12 was confirmed via ^{1}H-NMR spectroscopy. In addition, TGA analysis confirmed that the functionalization of SA onto H0 improved the thermal stability of H0. In the second step, PLA:H08 / 5:1 and PLA:H12 / 5:1 were blended with 0.02 % BTA catalyst in a reactive extrusion process. It was observed that BTA supported the reaction but BTA also affected thermal stability of PLA. ^{1}H-NMR spectroscopy confirmed functionalization of PLA on H08 in presence of BTA. However, the complete functionalization of PLA on H12 could not be confirmed owing to weak signal intensities. Finally, a blend comprising of PLA/mPE and PLA-modified H08 or PLA-modified H12 was prepared in a twin-screw extruder. The extrudate was highly deformed, and it was not possible to investigate the tensile properties of the resulting material.

Ternary blends comprising of PLA, different PE-types (HDPE, LDPE, LLDPE and mPE), and E-GMA were prepared in a twin-screw extruder. PLA/HDPE and PLA/LDPE blends compatibilized with 5 % E-GMA showed a major improvement in the elongation at break and nearly matched the elongation at break of PLA/mPE and PLA/LLDPE binary blends. Addition of E-GMA to PLA/LLDPE and PLA/mPE gave a slight boost to the elongation break of PLA/LLDPE and PLA/mPE binary blends. In case of all-ternary blends, the morphology of the dispersed phase was much finer, with a very few cavities on the fractured surface. The size of PE globules in HDPE and LDPE ternary blends dropped substantially and facilitated a better adhesion between the matrix and the dispersed phase, which was related to much improved elongation at break.

The impact of the dispersed phase and the compatibilizer on the weathering properties of PLA was investigated under hot and humid natural environmental conditions in Queensland, Australia. Blown film extrusion samples of PLA, PLA/mPE and PLA/mPE/E-GMA were placed above and underneath the soil over a period of 5 months. The weathering properties were correlated to the thermal stability data from TGA, as the low molecular weight species that originate from the degradation of long polymer chains can volatilize easily. Amongst the samples placed above the soil and with an exposure to direct sunlight, the thermal stability of PLA/mPE/E-GMA was better than that of PLA/mPE and was related to interfacial stability that

E-GMA incorporates in the ternary blend system. FT-IR spectroscopy confirmed that E-GMA and mPE did not hinder the degradation behavior of the PLA placed over the soil. In addition, GPC analysis confirmed that the molecular weight of PLA extracted from the PLA/mPE and PLA/mPE/E-GMA samples above the soil after five months of weathering period decreased compared to the molecular weight of PLA before weathering. This confirmed that mPE and E-GMA accelerate the degradation process of PLA in the blend. In the case of the sample specimens buried under the soil, PLA/mPE showed minor degradation in contrast to PLA and PLA/mPE/E-GMA that showed no signs of degradation. The degradation of PLA/mPE was attributed to the presence of micro voids that promoted water intake and subsequent PLA hydrolysis.

A novel nucleating agent, terephthaloyl-bis-N, N'-naphthalimidester (TN) was introduced in the present thesis. The nucleating ability of TN and different commercially-available nucleating agents, such as tetramethylenedicarboxylic dibenzoylhydrazide (TMC) and orotic acid (OA), on the crystallization capability of PLA, PLA/mPE and PLA/mPE/E-GMA was evaluated. First, the nucleating potential of TN, TMC, and OA under non-isothermal conditions was measured in two different PLA types - PLA 4032D (L/D; 98/2) compared to PLA 4043D (L/D; 95/5). All the nucleating agents significantly improved the crystallization kinetics of PLA 4032D compared to PLA 4043D. The nucleation efficiency of TN was comparable to OA and TMC, where only 0.3% of each nucleating agent improved the crystallization of PLA 4032D.

The nucleating efficiency of TMC, TN, and OA on the crystallization of PLA was investigated under isothermal conditions. An addition of 0.3% TMC, TN, and OA to PLA completed the crystallization process in less than 3 minutes. PLA nucleated with OA exhibits the highest crystallization rate, followed by PLA nucleated with TN, and PLA nucleated with TMC. It was found that crystallization is improved with an increase in crystallization temperature and the concentration of the nucleating agent.

The nucleation ability of TMC, TN, and OA in PLA/mPE binary blends and PLA/mPE/E-GMA ternary blend was evaluated under non-isothermal conditions. The blends were prepared in a twin-screw extruder and the blends were nucleated with 1 % of TMC, TN, and OA. The addition of TMC and TN had a positive impact on the crystallization behavior of binary blends, whereas the OA-nucleated ternary blend did not show any improvement in the crystallization behavior of PLA. The addition of TMC, TN, or OA caused a substantial drop in elongation at break of the binary blends. However, the addition of E-GMA to the blend composition improved the elongation at break. The ternary blend comprising of TN showed the maximum improvement, followed by the blend comprising of TMC. Addition of OA to the ternary blend substantially deteriorated the elongation at break.

8. Zusammenfassung

Das Ziel der vorliegenden Arbeit war die Verbesserung der Zug- und Kristallisationseigenschaften von PLA. In Anbetracht der Tatsache, dass die Zugfestigkeit von PLA ein weites Feld der Forschung ist, wurde der Schwerpunkt auf die Verbesserung der Bruchdehnung von PLA gelegt, ohne die Abbaueigenschaften von PLA zu beeinträchtigen. Ein weiteres Ziel im Zusammenhang mit der Verbesserung der Zugeigenschaften war die Entwicklung eines synthetischen Verfahrens zur Funktionalisierung eines kommerziell erhältlichen, hochverzweigten Polymers, mit der Absicht, die Kompatibilität von PLA/PE-Blends zu verbessern.

Die Strategie zur Verbesserung der Bruchdehnung basierte auf der Polymerblends-Theorie. Im ersten Schritt wurden die binären Mischungen aus PLA und verschiedenen PE-Typen (HDPE, LDPE, LLDPE und mPE) in einem Doppelschneckenextruder hergestellt. PLA-HDPE- und PLA-LDPE-Blends zeigten eine geringe Bruchdehnung, während PLA-LLDPE- und PLA-mPE-Blends eine sehr hohe Bruchdehnung aufwiesen. Die Zugabe von PE zu PLA senkte das Elastizitätsmodul der PLA-PE-Mischungen. Ein möglicher Erklärungsansatz stellt die plastifizierende Wirkung von PE dar. Morphologische Untersuchungen ergaben, dass ein Zusammenhang zwischen Bruchdehnung und Morphologie der Mischung besteht. PLA/HDPE- und PLA/LDPE-Blends zeigten geringe Bruchdehnungen, welche auf große Globuli aus HDPE und LDPE in der PLA-Matrix zurückzuführen sind. Diese sind lediglich schwach in die Matrix integriert. Andererseits war eine sehr hohe Bruchdehnung von PLA/LLDPE und PLA/mPE mit länglichen Mikrofibrillen der dispergierten Phase verbunden, welche in die PLA-Matrix interpenetriert sind.

Da je nach Zugbeanspruchung bei der Herstellung des Extrudats möglicherweise unterschiedliche Orientierung der Polymerkette erreicht wird, wurde die Auswirkung der verschiedenen Zugverhältnisse auf die Morphologie von PLA-PE-Mischungen evaluiert. Dafür wurde ein Kalenderwalzensystem verwendet, das dem extrudierten Material ein Dehnungsfeld verleiht, was wiederum die Morphologie und Materialeigenschaften beeinflusst. Die Mischungen von PLA-HDPE und PLA-mPE wurden unter drei verschiedenen Bedingungen hergestellt. Neben der direkten Wasserbadkühlung wurden zwei unterschiedliche Zugverhältnisse gewählt (4.5 und 9.0). Direkt im Wasserbad abgekühlte Mischungen zeigten eine kugelförmige Morphologie, was auf eine schlechte Grenzflächenhaftung hinweist. Interessanterweise zeigte die PLA-mPE-Mischung nach der Zugbeanspruchung eine fein fibrilläre Morphologie von gut dispergiertem mPE in der PLA-Matrix mit sehr wenigen vorhandenen Hohlräumen. Dies trägt potential zu einem Spannungsübertragung im System bei, was wiederum die Bruchdehnung steigert. Ähnliche Beobachtungen wurden bei beiden Zugverhältnissen festgestellt. Ein anderes Verhalten wurde bei PLA-HDPE Mischungen beobachtet. Mit zunehmendem Zugverhältnis reduziert sich schrittweise der Durchmesser der HDPE-Globuli aufgrund intensiver Streckverformung, wobei die Form der dispergierten Phase weiterhin kugelförmig bleibt.

Die zweite Strategie zur Verbesserung der Dehnung basierte auf dem Zusatz von Kompatibilisatoren zum binärem Blend. Das Thema der ternären Mischungen bestand aus zwei Teilen: Der Funktionalisierung eines hyperverzweigten Polymers in Richtung einer potenziell neuen Klasse von Kompatibilisatoren für PLA/PE-Blends, sowie der Herstellung von PLA/PE-Blends, die ein Kompatibilisierungsmittel (wie beispielsweise E-GMA) enthalten. Boltorn™ HB20 (H0), ein kommerziell erhältliches, hochverzweigtes Polyesterpolyol, wurde als Gerüst ausgewählt und in einem zweistufigen Prozess mit Stearinsäure (SA) und PLA funktionalisiert. Vor der Funktionalisierung von H0 mit SA und PLA wurde eine Modellstudie durchgeführt, um den Grad der funktionalisierten -OH-Gruppen zu bestimmen. Das so genannte TAI-Modell basierte auf dem Trichloracetylisocyanat (TAI) funktionalisierten H0, wobei der Funktionalisierungsgrad mittels 1H-NMR-Spektroskopie bestimmt wurde. Das TAI-Modell war ein sehr wichtiges Werkzeug, das die Quantifizierung der Funktionalisierung von H0 mit SA und PLA durch Bestimmung der restlichen -OH Gruppen ermöglichte.

Im ersten Schritt wurde SA zu H0 in zwei Molverhältnissen hinzugefügt; H0:SA 1:8 (H08) und 1:12 (H12). Eine Stearyl-Substitution von 48 % in H08 und 78 % in H12 wurde mittels ^{1}H-NMR-Spektroskopie nachgewiesen. Darüber hinaus bestätigte die TGA-Analyse, dass die Funktionalisierung von H0 mit SA die thermische Stabilität von H0 verbessert. Im zweiten Schritt wurden PLA:H08 / 5:1 und PLA:H12 / 5:1 mit 0,02 % BTA-Katalysator in einem reaktiven Extrusionsprozess vermischt. Es wurde beobachtet, dass BTA die Reaktion unterstützt, jedoch gleichzeitig die thermische Stabilität von PLA beeinflusst. Die 1H-NMR-Spektroskopie bestätigte die Funktionalisierung von H08 mit PLA in Gegenwart von BTA. Vollständige Funktionalisierung von PLA auf H12 ließ sich aufgrund schwacher Signalintensitäten nicht eindeutig bestätigen. Schließlich wurde in einem Doppelschneckenextruder eine Mischung aus PLA/mPE und PLA-modifiziertem H08 oder PLA-modifiziertem H12 hergestellt. Das extrudierte Material war stark verformt, sodass eine Untersuchung der Zugeigenschaften nicht zielführend gewesen wäre.

Ternäre Mischungen aus PLA, verschiedenen PE-Typen (HDPE, LDPE, LLDPE und mPE) und E-GMA wurden in einem Doppelschneckenextruder hergestellt. PLA/HDPE- und PLA/LDPE-Blends, die mit 5 % E-GMA kompatibilisiert wurden, zeigten eine deutliche Verbesserung der

Bruchdehnung und erreichten nahezu die Kennwerte von PLA/mPE- und PLA/LLDPE-binären Blends. Die Zugabe von E-GMA zu PLA/LLDPE und PLA/mPE führte zu einem leichten Anstieg der Bruchdehnung von PLA/LLDPE und PLA/mPE Binärmischungen. Bei morphologischen Untersuchungen der Bruchfläche zeigte sich bei allen ternären Mischungen eine feine dispergierte Phase mit einem geringen Anteil an Hohlräumen. Die Größe der PE-Globuli in ternären Mischungen aus HDPE und LDPE nahm erheblich ab und ermöglichte eine bessere Haftung zwischen der Matrix und der dispergierten Phase. Hieraus resultierte eine signifikante Verbesserung der Bruchdehnung.

Der Einfluss der dispergierten Phase und des Kompatibilisators auf die Witterungseigenschaften von PLA wurde in Queensland, Australien, unter heißen und feuchten natürlichen Umweltbedingungen untersucht. Dabei wurden mittels Blasfolienanlage 0.02-0.03 mm dicke Filme aus PLA, PLA/mPE und PLA/mPE/E-GMA hergestellt und unter- und oberhalb des Bodens über einen Zeitraum von 5 Monaten platziert.

Die Verwitterungseigenschaften wurden mit den Daten der Thermogravimetrischen Analyse (TGA) korreliert. Niedermolekulare Verbindungen, welche durch Degradationsprozesse aus langen Polymerketten gebildet werden, weisen eine geringe thermische Stabilität in der TGA auf und verflüchtigen sich daher früher. Proben von PLA/mPE/E-GMA, die über dem Boden platziert und direkter Sonneneinstrahlung ausgesetzt wurden, wiesen eine höhere thermische Stabilität als die unter gleichen Bedingungen gealterten PLA/mPE-Folien auf. Grund hierfür ist die Grenzflächenstabilität, welche durch E-GMA erreicht wurde. Durch FT-IR-Spektroskopie wurde belegt, dass E-GMA und mPE das Abbauverhalten der über dem Boden platzierten PLA nicht behindern.

Darüber hinaus wurde durch GPC-Analyse aufgeklärt, dass bei PLA die fünf monatige Bewitterungszeit zu einem Molekulargewichtsabbau führt. Dieses wurde aus Proben von PLA/mPE- und PLA/mPE/E-GMA-Proben extrahiert. Dies bestätigte, dass mPE und E-GMA den Abbauprozess von PLA in der Mischung beschleunigen. Bei den unter dem Boden platzierten Proben zeigte PLA/mPE einen geringeren Abbau im Gegensatz zu PLA und PLA/mPE/E-GMA, die keine Anzeichen eines Abbaus zeigten. Der Abbau von PLA/mPE wurde auf das Vorhandensein von Mikrohohlräumen zurückgeführt, welche die Wasseraufnahme und die anschließende PLA-Hydrolyse förderten.

Ein neuartiges Nukleierungsmittel, Terephthaloyl-bis-N,N'-Naphthalimidester (TN), wurde in der vorliegenden Arbeit zum Einsatz gebracht. Die Nukleierfähigkeit von TN und verschiedenen kommerziell verfügbaren Nukleierungsmitteln, wie Tetramethylendicarbonsäure-

Dibenzoylhydrazid (TMC) und Orotsäure (OA), wurde hinsichtlich der Kristallisationsfähigkeit von PLA, PLA/mPE und PLA/mPE/E-GMA untersucht. Zunächst wurde das Keimbildungspotenzial von TN, TMC und OA unter nicht-isothermen Bedingungen in zwei verschiedenen PLA-Typen, PLA 4032D (L/D; 98/2) und PLA 4043D (L/D; 95/5), analysiert. Alle Nukleierungsmittel verbesserten signifikant die Kristallisationskinetik von PLA 4032D, im Gegensatz zu PLA 4043D. Interessanterweise war die Keimbildungseffizienz von TN vergleichbar mit OA und TMC, wobei nur 0,3% jedes Keimbildungsmittels die Kristallisation von PLA 4032D verbesserten.

Die Keimbildungseffizienz von TMC, TN und OA auf die Kristallisation von PLA wurde ebenfalls unter isothermen Bedingungen untersucht. Aufgrund der Zugabe von 0,3% TMC, TN oder OA erfolgte die Beendung des Kristallisationsprozesses von PLA in weniger als 3 Minuten. PLA, das mit OA nukleiert wurde, weist die höchste Kristallisationsrate auf, gefolgt von PLA, das mit TN nukleiert wurde, und PLA, das mit TMC nukleiert wurde. Es wurde festgestellt, dass die Kristallisation mit einer Erhöhung der Kristallisationstemperatur und der Konzentration des Keimbildners verbessert wird. Die aufgeführten Ergebnisse qualifizieren TN für den Einsatz als Nukleierungsmittel in der Schmelzeverarbeitung.

Die Keimbildungsfähigkeit von TMC, TN und OA in PLA/mPE-Binärmischung und PLA/mPE/E-GMA-Ternärmischung wurde unter nicht-isothermen Bedingungen untersucht. Die mit 1 % TMC, TN oder OA nukleierten Mischungen wurden in einem Doppelschneckenextruder hergestellt. Die Zugabe von Nukleierungsmitteln hatte einen positiven Einfluss auf das Kristallisationsverhalten von binären Blends, während die OA-nukleierten ternäre Blends keine Verbesserung des Kristallisationsverhaltens von PLA zeigten. Die Zugabe von TMC, TN oder OA führte zu einem erheblichen Rückgang der Bruchdehnung der binären Mischungen. Die Zugabe von E-GMA zur Blend-Composition verbesserte jedoch die Bruchdehnung. Die ternäre Mischung mit Zusatz von TN, zeigte die maximale Verbesserung, gefolgt von der Mischung mit TMC. Die Zugabe von OA zur ternären Mischung führte dagegen zu einer erheblichen Verschlechterung der Bruchdehnung.

9. Outlook

It was shown that the choice of the dispersed phase in the blend composition has a substantial impact on the blend morphology and the resulting tensile properties. The control over the blend morphology played an important role in tailoring the elongation at break of PLA/PE blends that was achieved through the use of slit die and calendar roller at the die exit of a twin-screw extruder. As subsequent work, one could take a deeper look into the shear viscosity and the uniaxial elongation of the blend components to predict the most suitable PE type for in-situ fibrillation within the PLA matrix.

It was confirmed during the degradation field study that mPE accelerated the degradation rate of PLA. The blends investigated in the degradation field study contained PE particles smaller than 4 µm, which might degrade faster compared to larger PE particles. As PE itself has a very slow rate of degradation, the addition of PE prodegradants based on transition metal salts or carboxylates (such as stearates) to the blend composition might be another approach to be explored to accelerate the photo-degradation [216].

The functionalization of hyperbranched polymer (HBP) with SA and PLA through reactive melt blending presented a promising approach to develop a new class of compatibilizer for PLA/PE blends. The presence and concentration of tin catalyst was detected as a crucial factor that impacts the residual lactide level due to a reversible equilibrium polymerization reaction [217]. The residual monomer can induce processing instabilities due to viscosity and rheological changes leading to poor mechanical properties of the final product. It would be beneficial to explore organotin(IV) catalysts used in industrial (trans)esterification processes, and comparing its catalytic activities might help to optimize HBP functionalization reaction and reduce the amount of side reactions [218]. In addition, the focus of the current system was on modifying the second generation HBP. The functionalization of HBP with SA and PLA can be extended to higher generation of HBP with greater concentration of reactive sites. This could be an interesting approach towards tailoring interfacial properties of immiscible polymer blends and reducing the compatibilizer loading. Moreover, fatty acids with longer aliphatic tails can be chosen to ensure a better interaction with PE in PLA/PE blend.

The crystallization properties of PLA were improved through the use of a nucleating agent in the PLA/PE blend composition. Terephthaloyl-bis-N,N'-naphthalimidester (TN), which was introduced in the present thesis, was confirmed to be very efficient, and comparable or better than commercially-available nucleating agents for PLA. The strong nucleating ability of TN was confirmed based on crystallization study under non-isothermal and isothermal conditions.

Polarized optical microscopy accompanied by Atomic Force Microscopy (AFM) is yet another helpful tool to study crystallite growth, organization, and morphology. Understanding the dispersion of a nucleating agent and its solubility in the PLA melt can help to tune the crystal morphology and consequently, tailoring the permeability coefficient of the PLA film. This might be of great benefit in designing PLA-based food packaging materials [31]. Because PLA heat deflection temperature, strength, and stiffness are influenced by PLA crystallinity, it would be worthwhile to focus on fabrication of TN-nucleated goods via injection molding and process optimization, towards the development of high crystalline PLA molded articles [117].

10. Experimental

10.1. Material

Table 25 summarizes the list of polymers and Table 26 summarizes the list of additives and reagents used in the present work.

Table 25: List of polymers.

Polymer	Trade name	Supplier
PLA	Ingeo 4043D	Resinex
PLA	Ingeo 4032D	Resinex
mPE	Exceed 2018HA	ExxonMobil
LLDPE	LL 1001XV	ExxonMobil
LDPE	LD 185BW	ExxonMobil
HDPE	HTA 108	ExxonMobil
E-GMA	Lotader AX8840	Arkema
Boltorn	HB20	Perstorp

Table 26: List of additives/reagents.

Additive and reagents	Supplier
Tetramethylenedicarboxylic dibenzoylhydrazide	Oriental Faith
N-hydroxynaphthalimide	Sigma-Aldrich
Terephthalic acid dichloride	Sigma-Aldrich
Orotic acid	Sigma-Aldrich
Ethylene bis-stearamide	Münzing
Phthalimid	Sigma-Aldrich
Stearic acid	Sigma-Aldrich
p-toluensulfonic acid	Sigma-Aldrich
FASCAT 4100 (butyl stannoic acid catalyst)	PMC Organometallix
Trichloracetylisocyanate	Sigma-Aldrich

10.2. Synthesis

10.2.1. Terephthaloyl-bis-N, N'-naphthalimidester

N-hydroxynaphthalimide (28.7 g, 0.135 mol, 2.5 eq.) was dissolved in 800 mL dry pyridine at 55 °C in a dry 1 L three-neck round bottom flask with nitrogen inlet and gas bubbler. Terephthalic acid dichloride (10.95 g, 0.054 mol, 1 eq.) was added to the solution and the mixture was stirred under nitrogen for 6 hours at 50 °C. The precipitated product was washed with 5 % hydrochloric acid and with water and then dried for 12 h at 80 °C in a vacuum oven. Product with the yield of 93 % (28 g) was obtained. The decomposition temperature of 380 °C was determined using TGA.

^{1} **H-NMR** (ODCB, 300 MHz) δ [ppm] = 7.41 (t, 4H), 7.83 (d, 4H), 8.12 (s, 4H), 8.34 (d, 4H)

10.2.2. Stearic acid modified H0

Preparation of H08

Boltorn H20 (50 g, 0.029 mol, 1 eq.), stearic acid (65.12 g, 0.229 mol, 8 eq.) and p-toluensulfonic acid (2 g, 0.011 mol, 0.38 eq.) were placed in a 250 mL three-neck round bottom flask with an argon inlet. The flask containing the mixture was attached to vacuum line. The mixture was heated to 140 °C under argon (the reactants melt at 140 °C) and stirred for 16 hours. The water that condensed over the progress of the reaction was removed by applied vacuum. The resulting product was washed with ethanol and dried in vacuum oven. The decomposition temperature of 410 °C was determined using TGA.

^{1} **H-NMR** ($CDCl_3$, 500 MHz) δ [ppm] = 0.88 (t, 0.32H), 1.25 (m, 3.42H), 1.58 (m, 0.21H), 2.30 (m, 0.21H), 3.63 (m, 0.49H), 4.24 (m, 0.51H)

Preparation of H12

Boltorn H20 (35 g, 0.029 mol, 1 eq.), stearic acid (65.12 g, 0.229 mol, 8 eq.) and p-toluensulfonic acid (2 g, 0.011 mol, 0.38 eq.) were placed in a 250 mL three-neck round bottom flask with an argon inlet. The flask containing the mixture was attached to vacuum line. The mixture was heated to 140 °C under argon (the reactants melt at 140 °C) and stirred for 16 hours. The water that condensed over the progress of the reaction was removed by applied vacuum. The resulting product was washed with ethanol and dried in vacuum oven. The decomposition temperature of 420 °C was determined using TGA.

^{1} **H-NMR** ($CDCl_3$, 500 MHz) δ [ppm] = 0.88 (t, 0.51H), 1.25 (m, 5.26H), 1.58 (m, 0.34H), 2.30 (m, 0.34H), 3.63 (m, 0.36H), 4.24 (m, 0.64H)

10.3. TAI derivatization procedure

A polymer sample (3-10 mg) was dissolved in an aprotic solvent ($CDCl_3$ or DMSO-d_6) (0.5 mL). Afterwards, the dissolved mixture was transferred to a NMR tube. Derivatization with trichloroacetyl isocyanate (TAI) was performed in NMR tube upon addition of TAI (5-10 μL).

10.4. Compounding

10.4.1. Process 11 parallel twin-screw extruder

Polymer blends and PLA comprising of the nucleating agent (chapter 3, 5 and 6) were prepared by melt extrusion using parallel co-rotating twin-screw extruder Process 11 from Thermo Scientific. The screw had 11 mm screw diameter and length to diameter ratio (L/D) of 40. The laboratory scale extruder enabled to compound small amount of product and at the same time simulate an industrial process. The screw design consisted of feed, push, and mixing elements as shown in the Figure 56. The processed formulations were extruded with degassing vent.

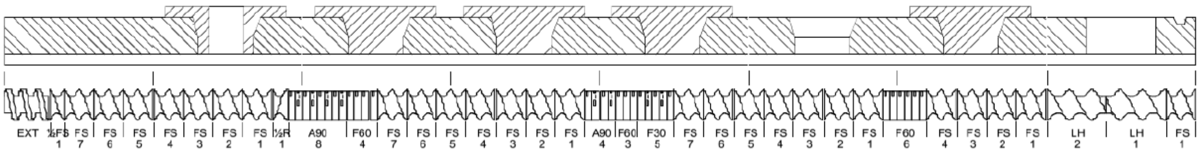

Figure 56: Screw profile of Process 11 twin screw extruder used in processing of polymer blends and PLA comprising of a nucleating agent.

Due to a small dimension of extruder, polymers were grounded in Retsch SM200 cutting mill. All polymers were dried in a vacuum oven prior to blending in order to avoid hydrolytic degradation of PLA during melt processing. PLA was dried at 80 °C for 24 hours under vacuum whereas the PE types, E-GMA and additives were dried at 60 °C for 8 hours under vacuum. Prior to the extrusion of compounds, components in a desired concentration were intimately mixed in a plastic bag for optical homogeneity. Blending of the components was carried out in extruder operating at a screw speed of 200 rpm and feed rate of 0.8 kg/h. The extruder was equipped with a slit die which was 30 mm wide and 0.4 mm thick.

Figure 57: Extruder equipped with slit die.

The temperature profile was set from 180 °C in the feed zone to 200 °C at the die. Extruded material was drawn continuously into film using either conveyer belt or stretching rolls in a three-roll calendar set-up. The three-roll calendar was used to tailor the morphology of PLA/PE blends. In the case of conveyor belt, the draw ratio of 2 was applied and extrudate was cooled with nitrogen flow. For three roll calendar the temperature was set to 15 °C and the draw ratio was set to 4.5 or 9.0. The draw ratio was defined as the ratio of the linear velocity of take-up device (conveyor belt or three roll calendar) to the linear velocity of the extrudate. The conveyor belt and calendar roll are shown in Figure 58.

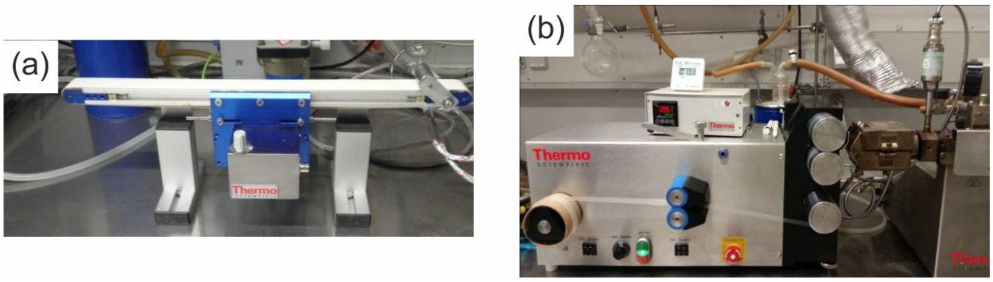

Figure 58: (a) Conveyor belt and (b)calendar roll.

10.4.2. JSW TEX 32 twin-screw extruder

Experiments to modify the hyperbranched polyester (chapter 4) were conducted in JSW TEX 32 co-rotating twin screw extruder, having 32 mm screw diameter and a length to diameter ratio (L/D) of 52. The screw design is presented in the Figure 59.

Figure 59: Screw profile of JSW TEX 32 twin screw extruder, employed in experiments on modification of hyperbranched polyester.

Prior to blending, PLA was dried at 60 °C for 12 hours in dehumidifying hopper, whereas hyperbranched polyester (H0, H08 and H12) were dried at 30 °C for 24 hours under vacuum. The extruder was loaded through two gravimetric dosage units. One unit was used for PLA, while another for hyperbranched polyester (H0, H08 or H12) and catalyst in powder form. Therefore, a precise control over the formulation concentration was ensured. The components were blended in an extruder operating at a screw speed of 300 rpm and feed rate of 5 kg/h at 180 °C. The extrudate was air-cooled and pelletized.

10.4.3. AxonBX25 extruder

Films for the degradation study (chapter 5, section 5.3) were prepared by melt extrusion using AxonBX25 extruder with single general-purpose screw having a length to diameter ratio (L/D) of 25. The extruder was fitted with a blowing die of 70 mm in a diameter with inner and outer air stream and associated tower. All polymers were dried in a vacuum oven prior to blending so as to avoid hydrolytic degradation of PLA during melt processing. PLA was dried at 80 °C for 24 hours under vacuum whereas the PE and E-GMA were dried at 60 °C for 8 hours under vacuum. Prior to extrusion, compounds were mixed in desired concentration in a plastic bag for optical homogeneity. The pellet composition was added to extruder and blending of the components was carried out in extruder operating at a screw speed of 30 rpm. Samples were compounded/melt mixed into film with the thickness of about 0.02-0.03 mm.

10.5. Analytical methods

10.5.1. Thermogravimetric analysis (TGA)

The thermogravimetric analysis was conducted on Mettler-Toledo TGA/DSC1 instrument in a nitrogen flow (50 ml/min) using ceramic crucible. Post the isothermal step at 35 °C (5 min), samples were heated to 600 or 700 °C at a rate of 10 °C/min. The data evaluation was carried out with STARe evaluation software form Mettler-Toledo AG. Thermogravimetric analysis was used as a method to determine thermal chain degradation, whereby temperatures for certain mass losses were detected. From the plot of first derivative of the TGA curve (DTG curve), the temperature of the maximum decomposition rate was obtained.

10.5.2. Differential scanning calorimeter (DSC)

The thermal properties of homopolymers and blends were measured using a differential scanning calorimeter (Mettler Toledo DSC 822E) in a nitrogen flow (20 ml/min). The DSC was calibrated periodically with indium and zinc standards. For the measurements, 7 (±0,1) mg of formulation or homopolymer was weighed and sealed in 40 µL aluminum pan. Prior to measurements, sample was dried for 12 hours at 60 °C in vacuum oven. The data evaluation was carried out with STARe evaluation software form Mettler-Toledo AG.

Non-isothermal measurement

All samples were measured under nitrogen atmosphere in the temperature range of 25-200 °C. Samples were heated from 25 °C to 200 °C at a rate of 10 °C/min (first heating cycle). After a period of 5 min the sample was cooled at a defined cooling rate (5, 10, 20 or 30 °C/min) to 25 °C (first cooling cycle) and reheated to 200 °C at a rate used previously for cooling (5, 10, 20 or 30 °C/min) (second heating cycle). In order to evaluate material properties without processing effects, thermograms of the first cooling and second heating cycle were analyzed. The thermograms from the first heating cycle were used only to evaluate the thermal history during processing. From the heating scan, glass transition temperature (T_g), peak temperature (T_{cc}) and enthalpy of the cold crystallization (ΔH_{cc}), melting temperature (T_m) and enthalpy of melting (ΔH_m) were detected, whereas melt crystallization (T_{cm}) and enthalpy (ΔH_{cm}) were measured during cooling scan.

Isothermal measurement

Samples were heated from 25 °C to 200 °C at a rate of 10 °C/min (first heating cycle). After a period of 5 min, samples were cooled at a rate of 80 °C/min to the desired temperature. The samples were at the desired temperature until the crystallization was complete.

10.5.3. Scanning electron microscopy (SEM)

Scanning electron microscopy (SEM) was used to investigate the blend morphology. The extruded film was fractured in liquid nitrogen at a direction perpendicular to the machine direction. The specimens were dried, attached to specimen mounts through conductive tape and the surface was sputter coated with gold within 180 s. The morphology was observed under a scanning electron microscope, Topcon SM 300, operated at 20 kV acceleration voltage.

10.5.4. Size-exclusion chromatography

To determine the average molar mass of PE, a High-Temperature Gel Permeation Chromatograph (HT-GPC), PL 220 (Agilent, Waldbronn, Germany), was used. The temperature of the injection sample block and of the column compartment was set at 150 °C. The flow rate of the mobile phase was 1 mL/min. The polymer was dissolved in 1,2,4- trichlorobenzene (TCB) (Merck, Darmstadt, Germany) at a concentration of 1 mg/mL at 150 °C and 200 μL of a polymer solution was injected. Polystyrene standards (Polymer Standards Service, PSS, Mainz, Germany) were used for calibration of a column set (3 x PL gel Olexis columns). The sample was detected using an infrared detector (model IR4, PolymerChar, Valencia, Spain). The data evaluation was carried out with the software WinGPC Unity.

The average molecular weight of PLA was determined by means of an Agilent 1100 HPLC System with RI-Detection (Agilent 1260 Infinity RI Detector). The temperature of the column compartment was set at 35 °C. The flow rate of the mobile phase was 1 mL/min. The polymer was dissolved in chloroform (Merck, Darmstadt, Germany) at a concentration of 2 mg/mL. 100 μL of a polymer solution was injected. Polystyrene standards (Polymer Standards Service, PSS, Mainz, Germany) were used for calibration of a column set (2 x PL Mixed columns). The data evaluation was carried out with the software WinGPC Unity.

10.5.5. Nuclear magnetic resonance spectroscopy (NMR)

The ^{13}C-NMR spectra of PE were recorded in a Varian Mercury-VX 400 NMR spectrometer (9.4 T, Palo Alto, US). 50 mg of each PE sample (mPE, LLDPE, HDPE and LDPE) were dissolved in 2 mL 1,2,4-trichlorobenzene at 160 °C upon addition of 1 mg Irganox B225 as stabilizer and ca. 14 mg $Cr(acac)_3$ as relaxation reagent. 0.5 mL deuterated 1,2-dichlorobenzene-d_4 was added. The inverse-gated -^{1}H-decoupling pulse sequence was used to acquire quantitative ^{13}C-NMR spectra. Further parameters were set as followed: temperature=140 °C, spectrometer frequency= 100.62 MHz, spectral with=25 kHz, acquisition time=1.3 s, relaxation delay=15 s, number of scans=4,400 – 16,000 depends on sample, chemical shift axis was referenced to the PE signal of repeating CH_2-units at 29.98 ppm.

The ^{1}H NMR spectrum of Terephthaloyl-bis-N, N'-naphthalimidester was acquired on a Varian Mercury-VX 400 NMR spectrometer (9.4 T, Palo Alto, US). 3 mg of the sample was dissolved in 1 mL 1,2,4-trichlorobenzene at 160 °C upon. 0.5 mL deuterated 1,2-dichlorobenzene-d_4 was added. For the 1H NMR measurement the following parameters were used: temperature=120 °C, spectrometer frequency= 400.13 MHz, spectral with=6.4 kHz, acquisition time=5.1 s, relaxation delay=25 s, number of scans=7936, chemical shift axis was referenced to the solvent.

The ^{1}H NMR spectra presented in chapter 6 were recorded using a Bruker Biospin Av500 spectrometer. The samples were dissolved in either $CDCl_3$ or DMSO-d_6 (as stated in the text, chapter 6). The parameters were set as followed: temperature=25 °C, spectrometer frequency= 500.53 MHz, spectral with=10 kHz, acquisition time=3.3 s, relaxation delay=2 s, number of scans=128, chemical shift axis was referenced to the solvent.

The data evaluation was carried out with the software MestReNova (Version 11.0.3). The signal assignments with corresponding numbers are presented in the associated figure.

10.5.6. Fourier transform infrared spectroscopy (FTIR)

IR spectra were recorded with Nicolet Nexus FTIR spectrometer in attenuated total reflectance (ATR) mode within the wavenumber range of 4000 to 525 cm^{-1} at an optical resolution of 4 cm^{-1} (64 scans), gain of 8 and a mirror velocity of 0.6329 cm/s. The data evaluation was carried out with the software OMNIC (Version 7.3).

10.5.7. Tensile test

The dog bone tensile test samples (25 mm · 4 mm · 0.3-0.45 mm; length · width · thickness) were punched out of the extruded film. These specimens were kept under ambient temperature for at least 48h prior to testing (23 °C, 50 % relative humidity). The tensile properties were measured at room temperature. The test was performed on a tensile tester Zwick/Roell, Germany at room temperature. The sample specimens were clamped between test jaws and the clamping force was manually adjusted by means of set screws. The test was performed with a pre-load of 5 N and crosshead speed of 20 mm/min. The elasticity modulus was measured with a test speed of 1 mm/min in the range of 0.05 to 0.25 % elongation.

I ^{13}C NMR Determination of PE Branching

Nomenclature used [219]:

- xB_n where n is the length of the branch and x is the carbon number starting with the methyl group as “1”
- for the backbone carbons, Greek letters and “br” are used instead of x for the methylenes and a branch point, respectively

HDPE

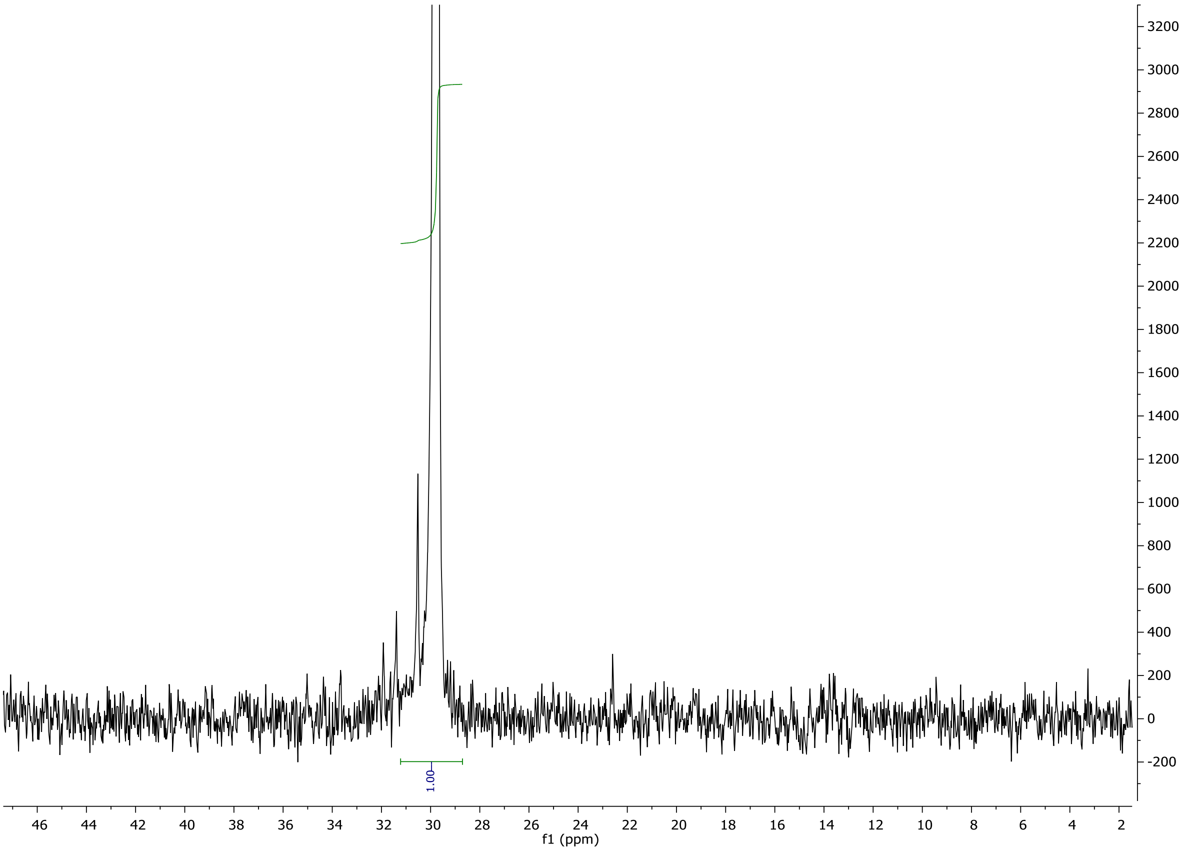

Figure 60: ^{13}C NMR spectrum of HDPE.

Table 27: HDPE- ^{13}C NMR chemical shift and assignments [219].

Chem. Shift (ppm)	Integral	Assignments
30	1	δB

LDPE

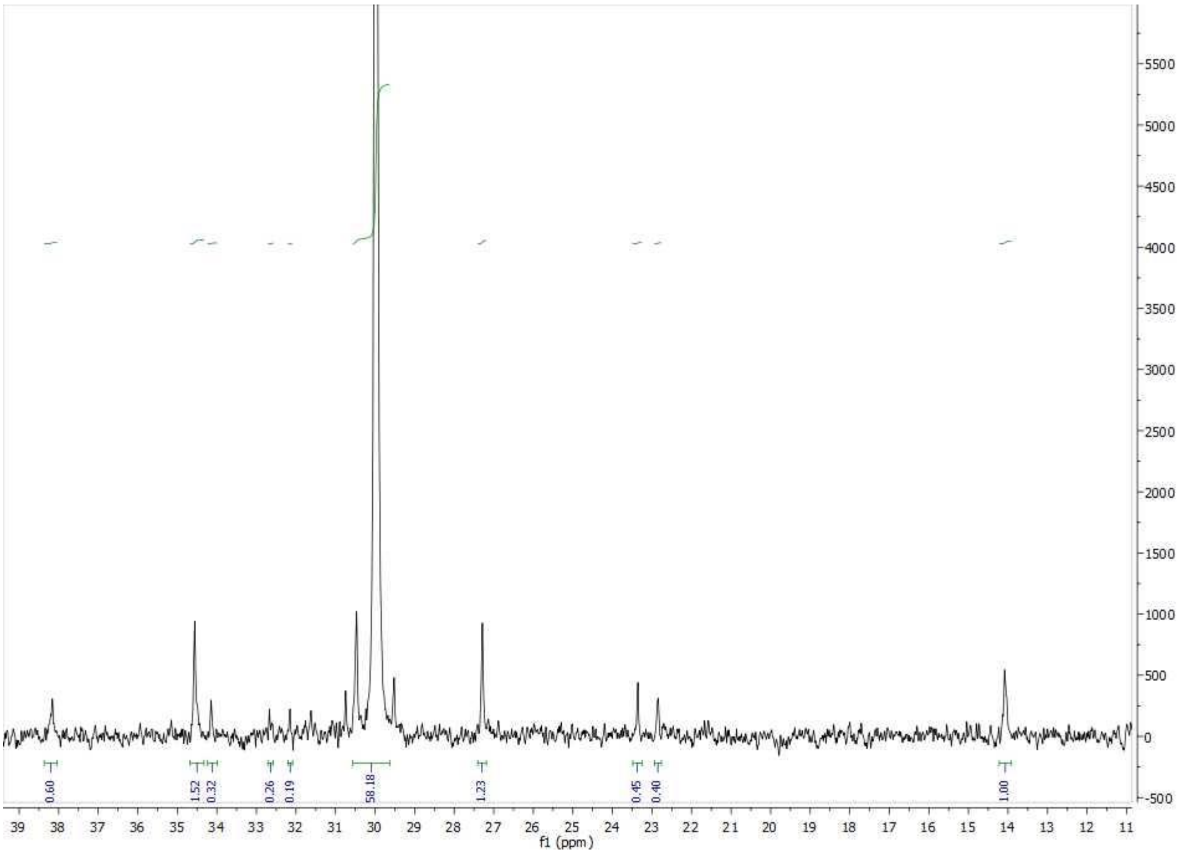

Figure 61: ^{13}C NMR spectrum of LDPE.

Table 28: LDPE- ^{13}C NMR chemical shift and assignments [219].

Chem. Shift (ppm)	Integral	Assignments
14.09	1	$1B_4$
22.84	0.4	$2B_5$
23.36	0.45	$2B_4$
27.3	1.23	βB_n
30	58.18	δB
32.15	0.19	$3B_6$
32.67	0.26	$3B_5$
34.15	0.32	$4B_4$
34.56	1.52	αB_n
38.16	0.6	brB_n

Branching	Branch degree (per 1000 Carbon)
Butyl branches	7
Amyl branches	4
Long branches	3

LLDPE

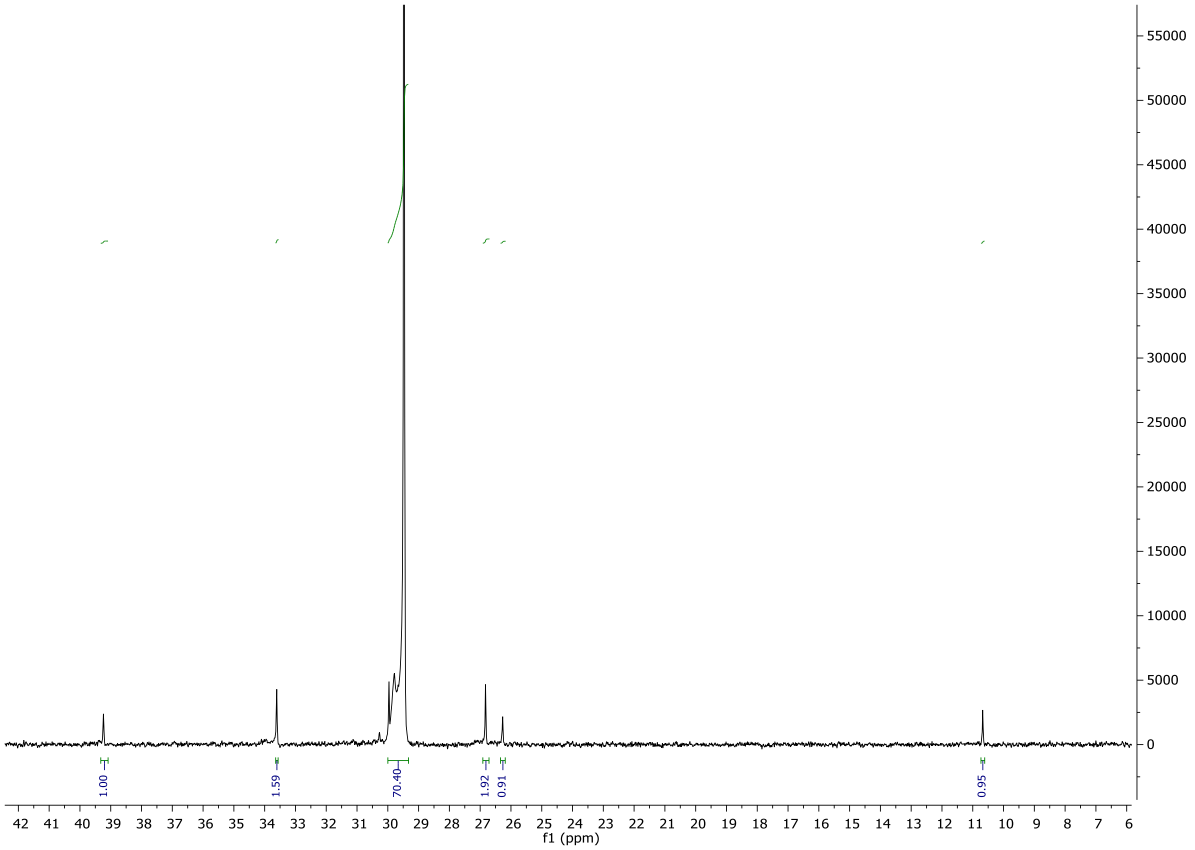

Figure 62: ^{13}C NMR spectrum of LLDPE.

Table 29: LLDPE- ^{13}C NMR chemical shift and assignments [219].

Chem. Shift (ppm)	Integral	Assignments
11.2	0.95	$1B_2$
26.8	0.91	$2B_2$
27.35	1.92	βB_2
30	70.4	δB
34.14	1.59	αB_2
39.76	1	brB_2

Branching	Branch degree (per 1000 Carbon)
Ethyl branches	13

mPE

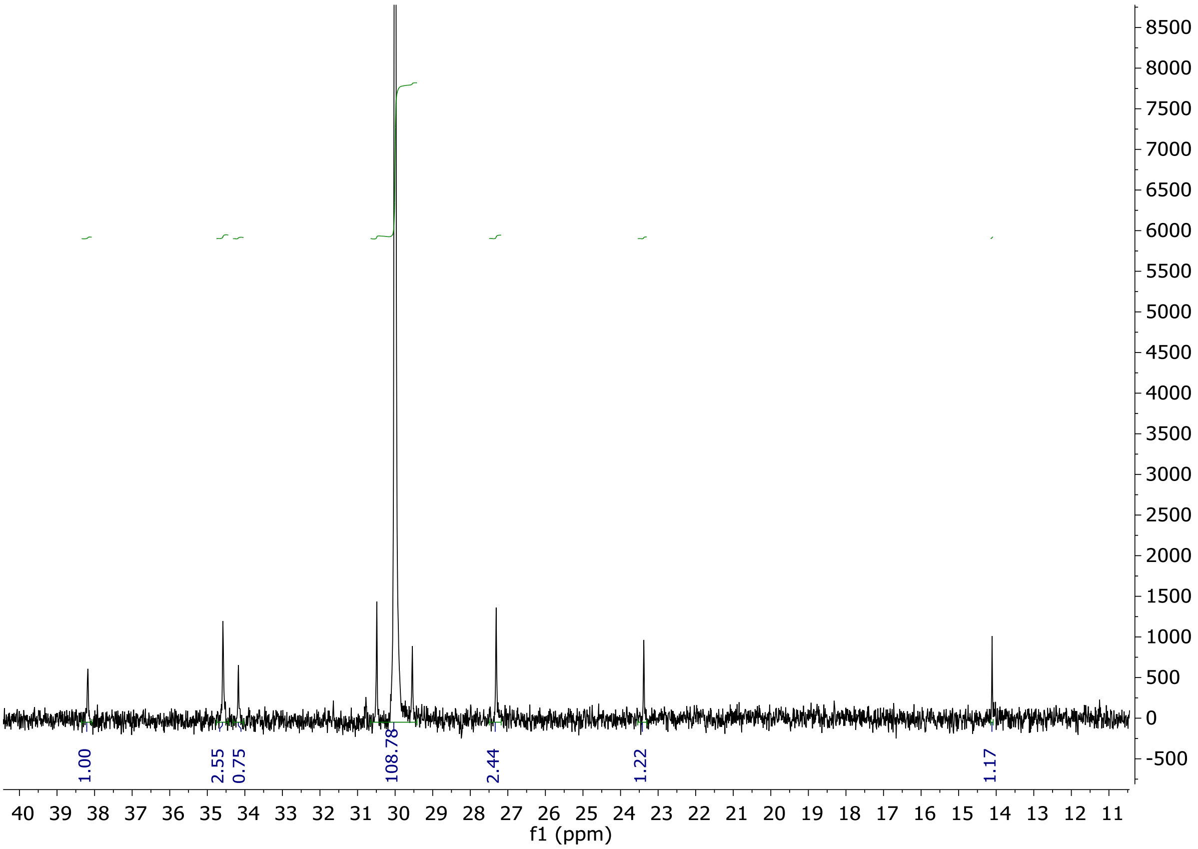

Figure 63: ^{13}C NMR spectrum of mPE.

Table 30: mPE- ^{13}C NMR chemical shift and assignments [219].

Chem. Shift (ppm)	Integral	Assignments
14.11	1.17	1B$_4$
23.38	1.22	2B$_4$
27.31	2.44	βB$_4$
30	108.78	δB
34.17	0.75	4B$_4$
34.58	2.55	αB$_4$
38.18	1	brB$_4$

Branching	Branch degree (per 1000 Carbon)
Butyl branches	10

II ^{1}H-NMR spectrum of H12 in CDCl$_3$

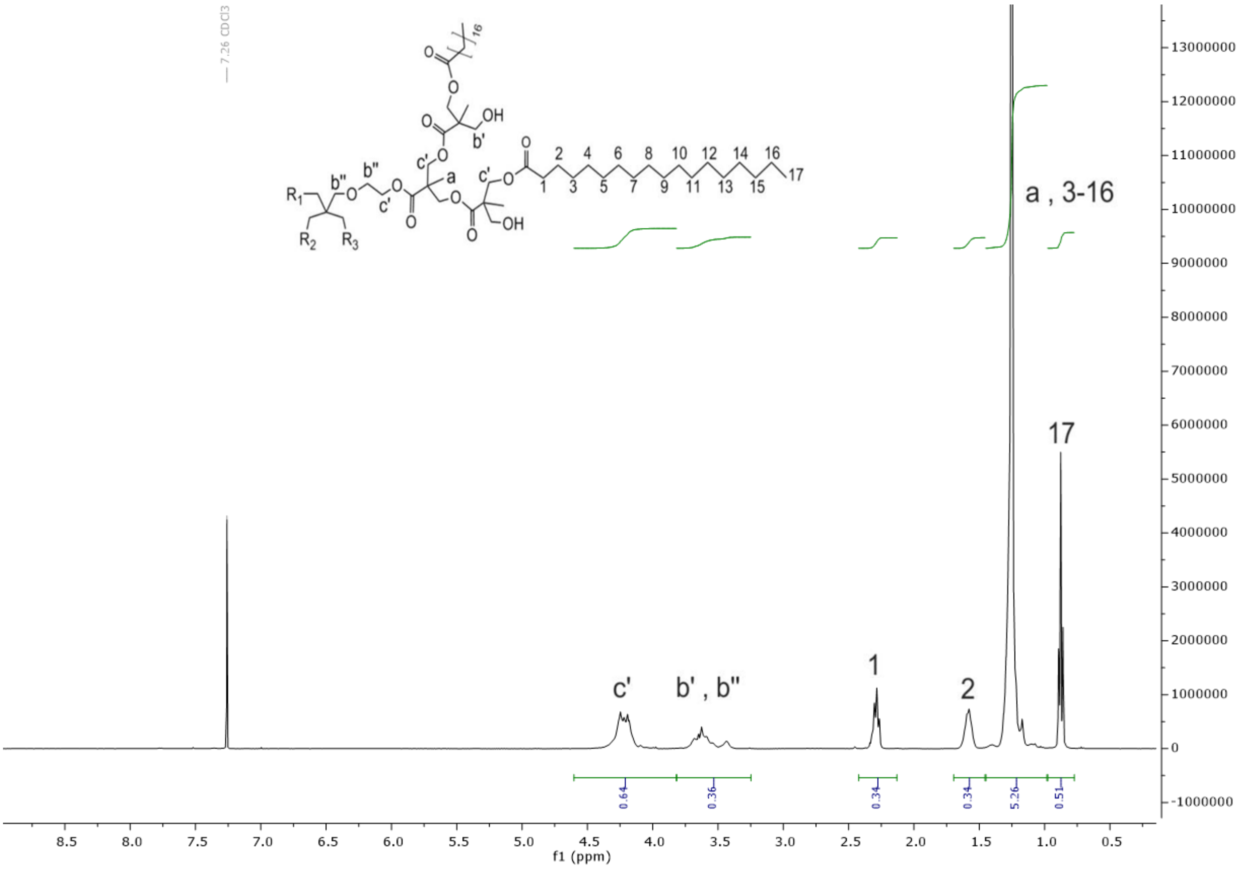

Figure 64: ^{1}H-NMR spectrum of H12 in CDCl$_3$.

List of figures

List of tables

Bibliography

[1] D. Greene, *EM Magazine, Solid Waste Management* **2017**.

[2] *Plastics Today: Community for plastics professiolanl* **2019 (online)**, https://www.plasticstoday.com/business/global-market-plastic-products-reach-1175-trillion-2020/13590261257995.

[3] *Center for International Environmental Law: Fossils, Plastics & Petrochemical Feedstocks* **2019 (online)**, http://www.ciel.org/wp-content/uploads/2017/09/Fueling-Plastics-Fossils-Plastics-Petrochemical-Feedstocks.pdf.

[4] *Plastics Europe: Plastics-The Facts 2017* **2019 (online)**, https://www.plasticseurope.org/application/files/5715/1717/4180/Plastics_the_facts_2017_FINAL_for_website_one_page.pdf.

[5] Ellen MacArthur Foundation Report, *The New Plastics Economy: Rethinking the future of plastics* **2016**.

[6] R. Geyer, J. R. Jambeck, K. L. Law, *Science advances* **2017**, *3*, 1.

[7] *Plastic Oceans* **2019 (online)**, https://www.futureagenda.org/insight/plastic-oceans.

[8] R. C. Thompson, C. J. Moore, F. S. Vom Saal, S. H. Swan, *Philosophical transactions of the Royal Society of London. Series B, Biological sciences* **2009**, *364*, 2153.

[9] Y. Zhu, C. Romain, C. K. Williams, *Nature* **2016**, *540*, 354.

[10] K. Madhavan Nampoothiri, N. R. Nair, R. P. John, *Bioresource technology* **2010**, *101*, 8493.

[11] R. Auras, *Poly(lactic acid): Synthesis, structures, properties, processing, and applications*, Wiley, Hoboken, N.J. **2010**.

[12] R. E. Conn, J. J. Kolstad, J. F. Borzelleca, D. S. Dixler, L. J. Filer, B. N. Ladu, M. W. Pariza, *Food and Chemical Toxicology* **1995**, *33*, 273.

[13] M. Jamshidian, E. A. Tehrany, M. Imran, M. Jacquot, S. Desobry, *Comprehensive Reviews in Food Science and Food Safety* **2010**, *9*, 552.

[14] E. Castro-Aguirre, F. Iñiguez-Franco, H. Samsudin, X. Fang, R. Auras, *Advanced drug delivery reviews* **2016**, *107*, 333.

[15] M. J. Stanford, A. P. Dove, *Chemical Society reviews* **2010**, *39*, 486.

[16] R. E. Drumright, P. R. Gruber, D. E. Henton, *Adv. Mater.* **2000**, *12*, 1841.

[17] E. T.H. Vink, S. Davies, *Industrial Biotechnology* **2015**, *11*, 167.

[18] V. H. Sangeetha, H. Deka, T. O. Varghese, S. K. Nayak, *Polym. Compos.* **2018**, *39*, 81.

[19] M. Karamanlioglu, R. Preziosi, G. D. Robson, *Polymer Degradation and Stability* **2017**, *137*, 122.

[20] A. Calmon, S. Guillaume, V. Bellon-Maurel, P. Feuilloley, F. Silvestre, *J Polym Environ* **1999**, *7*, 157.

[21] Y.-X. Weng, Y.-J. Jin, Q.-Y. Meng, L. Wang, M. Zhang, Y.-Z. Wang, *Polymer Testing* **2013**, *32*, 918.

[22] G. Perego, G. D. Cella, C. Bastioli, *J. Appl. Polym. Sci.* **1996**, *59*, 37.

[23] J. R. Sarasua, A. L. Arraiza, P. Balerdi, I. Maiza, *Polym. Eng. Sci.* **2005**, *45*, 745.

[24] J. Huang, M. S. Lisowski, J. Runt, E. S. Hall, R. T. Kean, N. Buehler, J. S. Lin, *Macromolecules* **1998**, *31*, 2593.

[25] G. Liu, X. Zhang, D. Wang, *Advanced materials (Deerfield Beach, Fla.)* **2014**, *26*, 6905.

[26] S. Saeidlou, M. A. Huneault, H. Li, C. B. Park, *Progress in Polymer Science* **2012**, *37*, 1657.

[27] Z. Tang, C. Zhang, X. Liu, J. Zhu, *J. Appl. Polym. Sci.* **2012**, *125*, 1108.

[28] Y. Srithep, P. Nealey, L.-S. Turng, *Polym Eng Sci* **2013**, *53*, 580.

[29] H. Tsuji, R. Okino, H. Daimon, K. Fujie, *J. Appl. Polym. Sci.* **2006**, *99*, 2245.
[30] H. J. Lehermeier, J. R. Dorgan, J.D. Way, *Journal of Membrane Science* **2001**, *190*, 243.
[31] H. Bai, C. Huang, H. Xiu, Q. Zhang, H. Deng, K. Wang, F. Chen, Q. Fu, *Biomacromolecules* **2014**, *15*, 1507.
[32] T. Tabi, I. E. Sajo, F. Szabo, A. S. Luyt, J. G. Kovacs, *expresspolymlett* **2010**, *4*, 659.
[33] R. Pantani, F. de Santis, A. Sorrentino, F. de Maio, G. Titomanlio, *Polymer Degradation and Stability* **2010**, *95*, 1148.
[34] L. Wang, Y.-N. Wang, Z.-G. Huang, Y.-X. Weng, *Materials & Design* **2015**, *66*, 7.
[35] M. Huda, L. Drzal, A. Mohanty, M. Misra, *Composites Science and Technology* **2006**, *66*, 1813.
[36] J. T. Wertz, T. C. Mauldin, D. J. Boday, *ACS applied materials & interfaces* **2014**, *6*, 18511.
[37] R. M. Rasal, A. V. Janorkar, D. E. Hirt, *Progress in Polymer Science* **2010**, *35*, 338.
[38] M. Murariu, A. Da Silva Ferreira, M. Alexandre, P. Dubois, *Polym. Adv. Technol.* **2008**, *19*, 636.
[39] V. Nagarajan, A. K. Mohanty, M. Misra, *ACS Sustainable Chem. Eng.* **2016**, *4*, 2899.
[40] A. Marra, C. Silvestre, D. Duraccio, S. Cimmino, *International journal of biological macromolecules* **2016**, *88*, 254.
[41] P. van Wouwe, M. Dusselier, E. Vanleeuw, B. Sels, *ChemSusChem* **2016**, *9*, 907.
[42] *Bioplastics Important Player in Sustainable Procurement* **2018 (online)**, http://www.mypurchasingcenter.com/commodities/commodities-articles/bioplastics-important-player-sustainable-procurement/.
[43] *Growth in PLA bioplastics* **2019 (online)**, http://www.bioplasticsmagazine.com/en/news/meldungen/PLA_Growth.php.
[44] G.-X. Chen, H.-S. Kim, E.-S. Kim, J.-S. Yoon, *Polymer* **2005**, *46*, 11829.
[45] J. J. Scobbo, L. A. Goettler, in *Polymer Blends Handbook* (Ed.: L. A. Utracki), Springer Netherlands. Dordrecht **2003**, p. 951.
[46] T. Sabu, B. Abderrahimc, I. Laurent, C. Yves, in *Handbook of Multiphase Polymer Systems* (Eds.: A. Boudenne, L. Ibos, Y. Candau, S. Thomas), John Wiley & Sons, Ltd. Chichester, UK **2011**, p. 1.
[47] Z. Starý, in *Characterization of Polymer Blends* (Eds.: S. Thomas, Y. Grohens, P. Jyotishkumar), Wiley-VCH Verlag GmbH & Co. KGaA. Weinheim, Germany **2014**, p. 93.
[48] J. N. Coupland, *An Introduction to the Physical Chemistry of Food*, Springer New York, New York, NY **2014**.
[49] P. Jyotishkumar, T. Sabu, Y. Grohens, in *Characterization of Polymer Blends* (Eds.: S. Thomas, Y. Grohens, P. Jyotishkumar), Wiley-VCH Verlag GmbH & Co. KGaA. Weinheim, Germany **2014**, p. 1.
[50] N.C. Liu, H. Huang, in *Reactive Polymer Blending* (Ed.: W. Baker), Carl Hanser & Co; Central Book Services New Zealand. Muchen, Mitcham, VIC, Australia **2001**, p. 14.
[51] S. Thomas, C. Harrats, G. Groeninckx, in *Micro- and nanostructured multiphase polymer blends systems: Phase morphology and interfaces* (Eds.: C. Harrats, S. Thomas, G. Groeninckx), Taylor & Francis. Boca Raton **2006**, p. 1.
[52] P. Van Puyvelde, P. Moldenaers, in *Micro- and nanostructured multiphase polymer blends systems: Phase morphology and interfaces* (Eds.: C. Harrats, S. Thomas, G. Groeninckx), Taylor & Francis. Boca Raton **2006**, p. 421.

[53] J.-C. Majesté, A. Santamaría, in *Handbook of Multiphase Polymer Systems* (Eds.: A. Boudenne, L. Ibos, Y. Candau, S. Thomas), John Wiley & Sons, Ltd. Chichester, UK **2011**, p. 311.
[54] U. Sundararaj, in *Micro- and nanostructured multiphase polymer blends systems: Phase morphology and interfaces* (Eds.: C. Harrats, S. Thomas, G. Groeninckx), Taylor & Francis. Boca Raton **2006**, p. 133.
[55] L. A. Utracki, in *Polymer Blends Handbook* (Ed.: L. A. Utracki), Springer Netherlands. Dordrecht **2003**, p. 1.
[56] L. A. Utracki, *Can. J. Chem. Eng.* **2002**, *80*, 1008.
[57] S. Datta, in *The Science and Technology of Rubber* (Eds.: E. Mark, Burak Erman, Mike Roland), Elsevier **2013**, p. 547.
[58] C. W. Macosko, P. Guégan, A. K. Khandpur, A. Nakayama, P. Marechal, T. Inoue, *Macromolecules* **1996**, *29*, 5590.
[59] W.E. Baker, G.-H. Hu, in *Reactive Polymer Blending* (Ed.: W. Baker), Carl Hanser & Co; Central Book Services New Zealand. Muchen, Mitcham, VIC, Australia **2001**, p. 1.
[60] J.-B. Zeng, K.-A. Li, A.-K. Du, *RSC Adv* **2015**, *5*, 32546.
[61] R. K. Sadi, R. S. Kurusu, G. J. M. Fechine, N. R. Demarquette, *J. Appl. Polym. Sci.* **2012**, *123*, 3511.
[62] W.-C. Jung, K.-Y. Park, J.-Y. Kim, K.-D. Suh, *J. Appl. Polym. Sci.* **2003**, *88*, 2622.
[63] N. Kalfoglou, *Polymer* **1995**, *36*, 4453.
[64] Y.-J. Sun, G.-H. Hu, M. Lambla, H. K. Kotlar, *Polymer* **1996**, *37*, 4119.
[65] C. M. Lee, E. S. Kim, J.-S. Yoon, *J. Appl. Polym. Sci.* **2005**, *98*, 886.
[66] C. Orr, *Polymer* **2001**, *42*, 8171.
[67] G. H. Hu, J. T. Lindt, *J. Polym. Sci. A Polym. Chem.* **1993**, *31*, 691.
[68] J.-C. Lepers, B. D. Favis, C. Lacroix, *J. Polym. Sci. B Polym. Phys.* **1999**, *37*, 939.
[69] K. L. Wooley, J. M.J. Fréchet, C. J. Hawker, *Polymer* **1994**, *35*, 4489.
[70] I. Sendijarevic, A. J. McHugh, *Macromolecules* **2000**, *33*, 590.
[71] C. M. Nunez, B.-S. Chiou, A. L. Andrady, S. A. Khan, *Macromolecules* **2000**, *33*, 1720.
[72] R. Mesias, E. Murillo, *Polímeros* **2018**, *25*, 748.
[73] G. Jannerfeldt, L. Boogh, J.-A. E. Mnson, *J. Polym. Sci. B Polym. Phys.* **1999**, *37*, 2069.
[74] G. Jannerfeldt, L. Boogh, J.-A.E. Månson, *Polymer* **2000**, *41*, 7627.
[75] G. Jannerfeldt, L. Boogh, J.-A. E. Månson, *Polym Eng Sci* **2001**, *41*, 293.
[76] W. Tang, Y. Huang, W. Meng, F.-L. Qing, *European Polymer Journal* **2010**, *46*, 506.
[77] C. Gao, D. Yan, *Progress in Polymer Science* **2004**, *29*, 183.
[78] C. Vasile, M. Pascu, *Practical guide to polyethylene*, RAPRA Technology, Shrewsbury **2005**.
[79] F. S. Qureshi, S. H. Hamid, A. G. Maadhah, M. B. Amin, *Polymer-Plastics Technology and Engineering* **1989**, *28*, 663.
[80] C. D. Rojas Gante, B. Pascat, *Packag. Technol. Sci.* **1990**, *3*, 97.
[81] A.-C. Albertsson, C. Barenstedt, S. Karlsson, T. Lindberg, *Polymer* **1995**, *36*, 3075.
[82] J. H. Khan, S.H. Hamid, *Polymer Degradation and Stability* **1995**, *48*, 137.
[83] Y. Lin, *J. Appl. Polym. Sci.* **1997**, *63*, 811.
[84] T. C. Rodrigues, M. I. B. Tavares, Pita, Victor Jayme Roget Rodriguez, *Macromol. Symp.* **2006**, *245-246*, 166.
[85] C. A. P. Joziasse, M. D. C. Topp, H. Veenstra, D. W. Grijpma, A. J. Pennings, *Polymer Bulletin* **1994**, *33*, 599.

[86] D. W. van Krevelen, K. t. Nijenhuis, *Properties of polymers: Their correlation with chemical structure; their numerical estimation and prediction from additive group contributions*, Elsevier, Amsterdam, Boston **2009**.
[87] M. A. Hillmyer, *J. Appl. Polym. Sci.* **2003**, *89*, 3757.
[88] K. Hamad, M. Kaseem, F. Deri, *ACES* **2011**, *01*, 208.
[89] K. Hamad, M. Kaseem, F. Deri, *Asia-Pac. J. Chem. Eng.* **2012**, *7*, S310-S316.
[90] S. Djellali, T. Sadoun, N. Haddaoui, A. Bergeret, *Polym. Bull.* **2015**, *72*, 1177.
[91] H. Balakrishnan, A. Hassan, M. U. Wahit, *Journal of Elastomers and Plastics* **2010**, *42*, 223.
[92] G. Jiang, H.-X. Huang, Z.-K. Chen, *Polymer-Plastics Technology and Engineering* **2011**, *50*, 1035.
[93] M. A. Hillmyer, *Polymer* **2004**, *45*, 8809.
[94] G. F. Brito, P. Agrawal, E. M. Araújo, Mélo, Tomás J. A. de, *Polímeros* **2012**, *22*, 427.
[95] A. P. M. Araújo, P. Agrawal, S. N. Cavalcanti, A. M. Alves, G. F. Brito, T. J. A. Mélo, *Macromol. Symp.* **2014**, *343*, 59.
[96] L. As'habi, S. H. Jafari, H. A. Khonakdar, L. Häussler, U. Wagenknecht, G. Heinrich, *Thermochimica Acta* **2013**, *565*, 102.
[97] L. As'habi, S. H. Jafari, H. A. Khonakdar, B. Kretzschmar, U. Wagenknecht, G. Heinrich, *J. Appl. Polym. Sci.* **2013**, *130*, 749.
[98] S.-M. Lai, K.-C. Hung, H. C. Kao, L.-C. Liu, X. F. Wang, *J. Appl. Polym. Sci.* **2013**, *130*, 2399.
[99] F.-C. Pai, H.-H. Chu, S.-M. Lai, *Journal of Polymer Engineering* **2011**, *31*.
[100] Y. F. Kim, C. N. Choi, Y. D. Kim, K. Y. Lee, M. S. Lee, *Fibers Polym* **2004**, *5*, 270.
[101] M. H. Abdolrasouli, H. Nazockdast, Sadeghi, Gity Mir Mohamad, J. Kaschta, *J. Appl. Polym. Sci.* **2015**, *132*, 2.
[102] M. Chanda, S. K. Roy, *Plastics technology handbook*, CRC Press, Boca Raton **2007**.
[103] Hans-Georg Elias (Ed.), *Makromoleüle Physikalische Strukturen und Eigenschaften*, Wiley-VCH, Weinheim **2001**.
[104] Y. P. Khanna, *Macromolecules* **1993**, *26*, 3639.
[105] R. J. Young, P. A. Lovell, *Introduction to polymers*, CRC Press, Boca Raton **2011**.
[106] H.-W. Zoch, G. Spur, *Handbuch Wärmebehandeln und Beschichten: Hans-Werner Zoch, Günter Spur*, Hanser, München **2015**.
[107] W. D. Callister, *Materials science and engineering: An introduction*, Wiley, New York, NY **2007**.
[108] B. J. Chisholm, P. M. Fong, J. G. Zimmer, R. Hendrix, *J. Appl. Polym. Sci.* **1999**, *74*, 889.
[109] R. D. Maier, M. Schiller, *Handbuch Kunststoff Additive*, Carl Hanser Verlag GmbH & Co. KG, München **2016**.
[110] D. M. Bigg, *Adv. Polym. Technol.* **2005**, *24*, 69.
[111] A. Komesu, Oliveira, Johnatt Allan Rocha de, Martins, Luiza Helena da Silva, M. R. Wolf Maciel, R. Maciel Filho, *BioResources* **2017**, *12*.
[112] J. J. Kolstad, *J. Appl. Polym. Sci.* **1996**, *62*, 1079.
[113] H.-Y. Yin, X.-F. Wei, R.-Y. Bao, Q.-X. Dong, Z.-Y. Liu, W. Yang, B.-H. Xie, M.-B. Yang, *CrystEngComm* **2015**, *17*, 4334.
[114] H. Abe, Y. Kikkawa, Y. Inoue, Y. Doi, *Biomacromolecules* **2001**, *2*, 1007.
[115] R. Vasanthakumari, A. J. Pennings, *Polymer* **1983**, *24*, 175.
[116] J. Ahmed, J.-X. Zhang, Z. Song, S. K. Varshney, *J Therm Anal Calorim* **2009**, *95*, 957.

[117] A. M. Harris, E. C. Lee, *J. Appl. Polym. Sci.* **2008**, *107*, 2246.

[118] Y. Feng, P. Ma, P. Xu, R. Wang, W. Dong, M. Chen, C. Joziasse, *International journal of biological macromolecules* **2018**, *106*, 955.

[119] H. Li, M. A. Huneault, *Polymer* **2007**, *48*, 6855.

[120] H. Tsuji, H. Takai, N. Fukuda, H. Takikawa, *Macromol. Mater. Eng.* **2006**, *291*, 325.

[121] L. Jiang, T. Shen, P. Xu, X. Zhao, X. Li, W. Dong, P. Ma, M. Chen, *e-Polymers* **2016**, *16*, 1.

[122] H. Nakajima, M. Takahashi, Y. Kimura, *Macromol. Mater. Eng.* **2010**, *295*, 460.

[123] P. Song, Z. Wei, J. Liang, G. Chen, W. Zhang, *Polym Eng Sci* **2012**, *52*, 1058.

[124] H. Bai, W. Zhang, H. Deng, Q. Zhang, Q. Fu, *Macromolecules* **2011**, *44*, 1233.

[125] B. Mallet, K. Lamnawar, A. Maazouz, *Polym Eng Sci* **2014**, *54*, 840.

[126] Q. Xing, X. Zhang, X. Dong, G. Liu, D. Wang, *Polymer* **2012**, *53*, 2306.

[127] T. Shen, Y. Xu, X. Cai, P. Ma, W. Dong, M. Chen, *RSC Adv.* **2016**, *6*, 48365.

[128] P. Ma, Y. Xu, D. Wang, W. Dong, M. Chen, *Ind. Eng. Chem. Res.* **2014**, *53*, 12888.

[129] N. Kawamoto, A. Sakai, T. Horikoshi, T. Urushihara, E. Tobita, *J. Appl. Polym. Sci.* **2007**, *103*, 198.

[130] H. Bai, C. Huang, H. Xiu, Q. Zhang, Q. Fu, *Polymer* **2014**, *55*, 6924.

[131] G.-X. Zou, Q.-W. Jiao, X. Zhang, C.-X. Zhao, J.-C. Li, *J. Appl. Polym. Sci.* **2015**, *132*, 1.

[132] Y. Cai, S. Yan, J. Yin, Y. Fan, X. Chen, *J. Appl. Polym. Sci.* **2011**, *121*, 1408.

[133] T. Xu, A. Zhang, Y. Zhao, Z. Han, L. Xue, *Polymer Testing* **2015**, *45*, 101.

[134] Y. Fan, J. Zhu, S. Yan, X. Chen, J. Yin, *Polymer* **2015**, *67*, 63.

[135] D. He, Y. Wang, C. Shao, G. Zheng, Q. Li, C. Shen, *Polymer Testing* **2013**, *32*, 1088.

[136] J. Li, D. Chen, B. Gui, M. Gu, J. Ren, *Polym. Bull.* **2011**, *67*, 775.

[137] Z. Qiu, Z. Li, *Ind. Eng. Chem. Res.* **2011**, *50*, 12299.

[138] P. Song, L. Sang, L. Zheng, C. Wang, K. Liu, Z. Wei, *RSC Adv.* **2017**, *7*, 27150.

[139] G. F. Brito, P. Agrawal, T. J. A. Mélo, *Macromol. Symp.* **2016**, *367*, 176.

[140] S. Djellali, N. Haddaoui, T. Sadoun, A. Bergeret, Y. Grohens, *Iran Polym J* **2013**, *22*, 245.

[141] Y. Feng, Y. Hu, J. Yin, G. Zhao, W. Jiang, *Polym Eng Sci* **2013**, *53*, 389.

[142] G. Singh, H. Bhunia, A. Rajor, R. N. Jana, V. Choudhary, *J. Appl. Polym. Sci.* **2010**, *118*, 496.

[143] G. Singh, H. Bhunia, A. Rajor, V. Choudhary, *Polym. Bull.* **2011**, *66*, 939.

[144] N. Khanoonkon, R. Yoksan, A. A. Ogale, *European Polymer Journal* **2016**, *76*, 266.

[145] N. Khanoonkon, R. Yoksan, A. A. Ogale, *Carbohydrate Polymers* **2016**, *137*, 165.

[146] R. Mesias, E. A. Murillo, *J. Appl. Polym. Sci.* **2015**, *132*, n/a-n/a.

[147] M. Srisa-ard, Y. Baimark, *J. of Applied Sciences* **2010**, *10*, 1937.

[148] R. Bhardwaj, A. K. Mohanty, *Biomacromolecules* **2007**, *8*, 2476.

[149] G. Jiang, L. Wang, H. Yu, C. Chen, X. Dong, T. Chen, Q. Yang, *Polymer* **2006**, *47*, 12.

[150] L. R. Hart, N. A. Nguyen, J. L. Harries, M. E. Mackay, H. M. Colquhoun, W. Hayes, *Polymer* **2015**, *69*, 293.

[151] S. Sivakova, S. J. Rowan, *Chemical Society reviews* **2005**, *34*, 9.

[152] J. Liu, H. Liang, C. Li, F. Hu, *Polym Eng Sci* **2019**, *59*, E133-E143.

[153] J. Jang, J. H. Oh, S. I. Moon, *Macromolecules* **2000**, *33*, 1864.

[154] J. K. Nath, J. B. Baruah, *CrystEngComm* **2015**, *17*, 8575.

[155] R. Pfaendner, E. Metzsch-Zilligen, M. Stec, *Use of organic oxy imides as flame retardants for plastic and flame-retardantplastics composition and mouldings produced therefrom* **2014**.

[156] C. Janiak, *J. Chem. Soc., Dalton Trans.* **2000**.
[157] E. Žagar, M. Žigon, S. Podzimek, *Polymer* **2006**, *47*, 166.
[158] E. Žagar, M. Žigon, *Progress in Polymer Science* **2011**, *36*, 53.
[159] L. Chikh, M. Tessier, A. Fradet, *Polymer* **2007**, *48*, 1884.
[160] A. Burgath, A. Sunder, H. Frey, *Macromol. Chem. Phys.* **2000**, *201*, 782.
[161] E. Žagar, M. Huskić, M. Žigon, *Macromol. Chem. Phys.* **2007**, *208*, 1379.
[162] E. Žagar, M. Žigon, *Journal of Chromatography A* **2004**, *1034*, 77.
[163] E. Žagar, M. Žigon, *Macromolecules* **2002**, *35*, 9913.
[164] E. Žagar, J. Grdadolnik, *Journal of Molecular Structure* **2003**, *658*, 143.
[165] E. Žagar, M. Huskić, J. Grdadolnik, M. Žigon, A. Zupančič-Valant, *Macromolecules* **2005**, *38*, 3933.
[166] D. K. Wang, D. J. T. Hill, F. A. Rasoul, A. K. Whittaker, *J. Polym. Sci. A Polym. Chem.* **2012**, *50*, 1143.
[167] A. R. Donovan, G. Moad, *Polymer* **2005**, *46*, 5005.
[168] A. Postma, T. P. Davis, A. R. Donovan, G. Li, G. Moad, R. Mulder, M. S. O'Shea, *Polymer* **2006**, *47*, 1899.
[169] X. Fernández-Francos, D. Foix, À. Serra, J. M. Salla, X. Ramis, *Reactive and Functional Polymers* **2010**, *70*, 798.
[170] Y. C. Brito, D. A.C. Ferreira, Fragoso, Danielle M. de A., P. R. Mendes, C. M.J. d. Oliveira, M. R. Meneghetti, S. M.P. Meneghetti, *Applied Catalysis A: General* **2012**, *443-444*, 202.
[171] A. B. Ferreira, A. Lemos Cardoso, M. J. da Silva, *ISRN Renewable Energy* **2012**, *2012*, 1.
[172] W. Chumeka, P. Pasetto, J.-F. Pilard, V. Tanrattanakul, *Polymer* **2014**, *55*, 4478.
[173] T. Kanno, H. T. Oyama, S. Usugi, *European Polymer Journal* **2014**, *54*, 62.
[174] F.-D. Kopinke, M. Remmler, K. Mackenzie, M. Möder, O. Wachsen, *Polymer Degradation and Stability* **1996**, *53*, 329.
[175] S. Fakirov, D. Bhattacharyya, R. J. T. Lin, C. Fuchs, K. FRIEDRICH, *Journal of Macromolecular Science, Part B* **2007**, *46*, 183.
[176] J. Jiang, L. Su, K. Zhang, G. Wu, *J. Appl. Polym. Sci.* **2013**, *128*, 3993.
[177] N. C. Thanh, C. Ruksakulpiwat, Y. Ruksakulpiwat, *MSCE* **2015**, *03*, 102.
[178] C. Kaynak, B. Sarı, *Applied Clay Science* **2016**, *121-122*, 86.
[179] N. R. Nair, V. C. Sekhar, K. M. Nampoothiri, *Indian journal of microbiology* **2016**, *56*, 59.
[180] C. Kaynak, I. Kaygusuz, *Journal of Composite Materials* **2016**, *50*, 365.
[181] M. Bijarimi, S. Ahmad, R. Rasid, *Journal of Reinforced Plastics and Composites* **2013**, *32*, 1656.
[182] H. Balakrishnan, A. Hassan, M. Imran, M. U. Wahit, *J Polym Environ* **2011**, *19*, 863.
[183] E. Rudnik, D. Briassoulis, *J Polym Environ* **2011**, *19*, 18.
[184] L. Zaidi, M. Kaci, S. Bruzaud, A. Bourmaud, Y. Grohens, *Polymer Degradation and Stability* **2010**, *95*, 1751.
[185] M. Oliveira, E. Santos, A. Araújo, G. J.M. Fechine, A. V. Machado, G. Botelho, *Polymer Testing* **2016**, *51*, 109.
[186] D. Rasselet, A. Ruellan, A. Guinault, G. Miquelard-Garnier, C. Sollogoub, B. Fayolle, *European Polymer Journal* **2014**, *50*, 109.
[187] G. Gorrasi, R. Pantani, *Polymer Degradation and Stability* **2013**, *98*, 1006.
[188] J. Palacio, V. H. Orozco, B. L. López, *J. Braz. Chem. Soc.* **2011**.

[189] R. L. Shogren, W. M. Doane, D. Garlotta, J. W. Lawton, J. L. Willett, *Polymer Degradation and Stability* **2003**, *79*, 405.
[190] Y. Tokiwa, B. P. Calabia, *Applied microbiology and biotechnology* **2006**, *72*, 244.
[191] M. Karamanlioglu, G. D. Robson, *Polymer Degradation and Stability* **2013**, *98*, 2063.
[192] J.-R. Sarasua, R. E. Prud'homme, M. Wisniewski, A. Le Borgne, N. Spassky, *Macromolecules* **1998**, *31*, 3895.
[193] E. W. Fischer, H. J. Sterzel, G. Wegner, *Kolloid-Z.u.Z.Polymere* **1973**, *251*, 980.
[194] P. Pan, W. Kai, B. Zhu, T. Dong, Y. Inoue, *Macromolecules* **2007**, *40*, 6898.
[195] C.-C. Tsai, R.-J. Wu, H.-Y. Cheng, S.-C. Li, Y.-Y. Siao, D.-C. Kong, G.-W. Jang, *Polymer Degradation and Stability* **2010**, *95*, 1292.
[196] J. Zhang, K. Tashiro, H. Tsuji, A. J. Domb, *Macromolecules* **2008**, *41*, 1352.
[197] S. Molinaro, M. Cruz Romero, M. Boaro, A. Sensidoni, C. Lagazio, M. Morris, J. Kerry, *Journal of Food Engineering* **2013**, *117*, 113.
[198] M. Pluta, *J. Polym. Sci. B Polym. Phys.* **2006**, *44*, 3392.
[199] J. Odent, J.-M. Raquez, P. Leclère, F. Lauro, P. Dubois, *Polym. Adv. Technol.* **2015**, *26*, 814.
[200] K. Rinawa, S. N. Maiti, R. Sonnier, J.-M. L. Cuesta, *Bull Mater Sci* **2015**, *38*, 1315.
[201] B. Reddy (Ed.), *Advances in Diverse Industrial Applications of Nanocomposites*, InTech **2011**.
[202] N. Kawamoto, A. Sakai, T. Horikoshi, T. Urushihara, E. Tobita, *J. Appl. Polym. Sci.* **2007**, *103*, 244.
[203] Z. Gui, C. Lu, S. Cheng, *Polymer Testing* **2013**, *32*, 15.
[204] Q. Fu, F.-C. Chiu, K. McCreight, M. Guo, W. Tseng, S. Cheng, M. Keating, E. Hsieh, P. DesLauriers, *J. of Macromolecular Sc., Part B* **1997**, *36*, 41.
[205] Q. Fu, F.-C. Chiu, T. He, J. Liu, E. T. Hsieh, *Macromol. Chem. Phys.* **2001**, *202*, 927.
[206] M. Run, J. Gao, Z. Li, *Thermochimica Acta* **2005**, *429*, 171.
[207] M. L. Arnal, A. J. Müller, *Macromol. Chem. Phys.* **1999**, *200*, 2559.
[208] H. Wu, S. Guo, G. Chen, H. Shi, *J. Appl. Polym. Sci.* **2004**, *94*, 2522.
[209] M. van Drongelen, P. C. Roozemond, E. M. Troisi, A. K. Doufas, G.W.M. Peters, *Polymer* **2015**, *76*, 254.
[210] E. Tarasova, T. Poltimäe, A. Krumme, A. Lehtinen, A. Viikna, *J Polym Res* **2011**, *18*, 207.
[211] M. L. Arnal, M. E. Matos, R. A. Morales, O. O. Santana, A. J. Müller, *Macromolecular Chemistry and Physics* **1998**, *199*, 2275.
[212] R. M. Michell, A. J. Müller, *Progress in Polymer Science* **2016**, *54-55*, 183.
[213] T. S. Omonov, C. Harrats, P. Moldenaers, G. Groeninckx, *Polymer* **2007**, *48*, 5917.
[214] S. Mbarek, C. Carrot, Y. Chalamet, M. Jaziri, B. Elleuch, *Int J Mater Form* **2008**, *1*, 635.
[215] P. Martin, J. Devaux, R. Legras, M. van Gurp, M. van Duin, *Polymer* **2001**, *42*, 2463.
[216] E. Gauthier, M. Nikolić, R. Truss, B. Laycock, P. Halley, *J. Appl. Polym. Sci.* **2015**, *132*, 1.
[217] D. L. Kaplan, *Biopolymers from Renewable Resources*, Springer Berlin Heidelberg, Berlin, Heidelberg **1998**.
[218] M. R. Meneghetti, S. M. P. Meneghetti, *Catal. Sci. Technol.* **2015**, *5*, 765.
[219] G. B. Galland, R. F. de Souza, R. S. Mauler, F. F. Nunes, *Macromolecules* **1999**, *32*, 1620.

Erklärungen laut Promotionsordnung

§8 Abs. 1 lit. c PromO

Ich versichere hiermit, dass die elektronische Version meiner Dissertation mit der schriftlichen Version übereinstimmt und für die Durchführung des Promotionsverfahrens vorliegt.

§8 Abs. 1 lit. d PromO

Ich versichere hiermit, dass zu einem vorherigen Zeitpunkt noch keine Promotion versucht wurde und zu keinem früheren Zeitpunkt an einer in- oder ausländischen Hochschule eingereicht wurde. In diesem Fall sind nähere Angaben über Zeitpunkt, Hochschule, Dissertationsthema und Ergebnis dieses Versuchs mitzuteilen.

§9 Abs. 1 PromO

Ich versichere hiermit, dass die vorliegende Dissertation selbständig und nur unter Verwendung der angegebenen Quellen verfasst wurde.

§9 Abs. 2 PromO

Die Arbeit hat bisher noch nicht zu Prüfungszwecken gedient.

Darmstadt 13. April 2021

Maria Gokhale-Stec

Curriculum Vitae

Name: Maria Gokhale-Stec

Date of Birth: 14.08.1987

Place of Birth: Dębica, Poland

Nationality: Polish

10/2018 - present	Technical Service Qualification Specialist at Cytec Engineered Materials GmbH, Solvay Group
	Education
07/2014 – 06/2018	Fraunhofer Institute for Structural Durability and System Reliability LBF /Technical University of Darmstadt, Germany Commonwealth Scientific and Industrial Research Organisation, Melbourne, Australia University of Queensland, Brisbane, Australia PhD Thesis: “Improvement of ductility and crystallization properties of poly (lactic acid) (PLA)”
04/2011 - 11/2013	Technical University of Darmstadt Master of Science, Chemistry
04/2013 – 10/2013	Fraunhofer Institute for Structural Durability and System Reliability LBF Master Thesis: “Novel flame retardants based on imides”
06/2011 – 09/2011	Heriot-Watt-University, Edinburgh, Scotland Internship
10/2006 – 04/2011	Technical University of Darmstadt Bachelor of Science, Chemistry
08/2010 – 10/2010	Department of Macromolecular Chemistry and Paper Chemistry at Technical University of Darmstadt Master Thesis: “Investigation of bio-conjugation of functional polymers to cyclic peptides”
09/2003 – 06/2006	High School named after King Władysław Jagiełło, Dębica, Poland Abitur

Maria Gokhale-Stec